UNIVERSITÉ DE MONTRÉAL

DELAY OF ROTATING STALL IN COMPRESSORS USING PLASMA ACTUATION

FARZAD ASHRAFI
DÉPARTEMENT DE GÉNIE MÉCANIQUE
ÉCOLE POLYTECHNIQUE DE MONTRÉAL

MÉMOIRE PRÉSENTÉ EN VUE DE L'OBTENTION
DU DIPLÔME DE MAÎTRISE ÈS SCIENCES APPLIQUÉES
(GÉNIE MÉCANIQUE)
AVRIL 2014

UNIVERSITÉ DE MONTRÉAL

ÉCOLE POLYTECHNIQUE DE MONTRÉAL

Ce mémoire intitulé :

DELAY OF ROTATING STALL IN COMPRESSORS USING PLASMA ACTUATION

présenté par : ASHRAFI Farzad
en vue de l'obtention du diplôme de : Maîtrise ès sciences appliquées
et a été dûment accepté par le jury d'examen constitué de :

M. MUREITHI Njuki W., Ph.D., président
M. VO Huu-Duc, Ph.D., membre et directeur de recherche
M. TRÉPANIER Jean-Yves, Ph.D., membre

ACKNOWLEDGMENTS

I would first like to express my deepest gratitude to Prof. Huu Duc Vo my thesis supervisor, for accepting me as his masters student, trusting me and for his continuous support and guidance besides his availability over the past two years. I want also to thank him for providing such an interesting project that I would not even think about.

I wish to express my gratitude to Mr. Xiaofei Xu for his help in CFD implementation of the plasma actuation model in my CFX simulations and also his help for setting up the plasma generation system, for this issue I also owe many thanks to Shubhankar Ghosh former master's student, who is now graduated for helping me in learning installations of plasma actuators in experimental tests.

I am also thankful to Martial Dumas, another graduated master's student and my previous colleague in office who helped me a lot in my mesh generation as well as numerical simulations with CFX and for his constructive and critical comments.

I also appreciate Mathias Michaud 2nd year undergraduate student working as an intern, for fixing the required settings in LabView software and for his great helps and technical assistance in laboratory for installations of test rig and measurement instrumentations as well as in performing data post processing.

I would also thank the PI4 (a group of 15 undergraduate final year students in integrated project four) who provided me the geometry and useful information about the compressor test rig and its operational conditions specially (Jade Bilodeau for centrifugal compressor geometry and simulations, Jean-Philippe Gauthier for the entire two-stage simulations and mesh, Jonathan Delarosbil, Mehregan Dor and Mateusz Kuczera for shaft alignments and installations of rig and finally Pierre-Olivier Tardif for programming the LabView interface).

I have also special appreciation for my colleagues Javad Hosseini, Francis Demers, Petro Junior Milan and Xin Gu for a friendly and pleasant atmosphere in the office and also for their technical assistance, discussions and advices.

Last but not least, I would like to thank my parents for their moral supports and patience during these two years as well as my sister and my brother-in-law for their presence, helps and supports.

RÉSUMÉ

Le décrochage tournant est une instabilité aérodynamique des compresseurs qui est bien connue et qui limite l'enveloppe d'opération des turbines à gaz de moteurs d'avion. Une méthode innovatrice avait été proposée pour supprimer le type d'initiation le plus commun au décrochage tournant en utilisant un actionneur plasma DBD annulaire. Un actionneur plasma DBD est un dispositif simple sans pièces mobiles qui convertit l'électricité directement en accélération de l'écoulement via l'ionisation partielle de l'air. Cependant, le concept proposé n'avait été évalué que de façon préliminaire via de simples simulations numériques d'un rotor axial isolé avec un code CFD rudimentaire. Ce projet fait une évaluation expérimentale ainsi que numérique de ce concept pour un étage de compresseur axial et un étage de compresseur centrifuge, tous deux faisant partie d'un banc d'essai de compresseur bi-étagé axial-centrifuge à basse vitesse.

Les deux configurations étudiées sont la configuration bi-étagé avec un actionneur plasma annulaire de 100 mN/m placé sur le carter juste en amont du bord d'attaque du rotor axial, et une configuration avec un seul étage de compresseur centrifuge dans lequel le même actionneur est placé juste en amont du bord d'attaque de l'impulseur. Les configurations testées furent simulées avec un code RANS CFD commercial sophistiqué (ANSYS CFX) dans lequel furent intégrés le plus récent modèle d'ingénierie de l'actionneur DBD ainsi qu'une condition de sortie dynamique, sur des domaines de calcul multi-étagé à un passage d'aube.

Les mesures expérimentales montrent que l'actionneur plasma DBD annulaire sur le carter réduit le débit massique du dernier point d'opération stable (point de décrochage tournant) de 19.28% pour l'étage de compresseur axial et de 28.39% pour l'étage de compresseur centrifuge pour lequel l'impulseur était la source du décrochage tournant. Les simulations numériques indiquent que pour les deux types de compresseurs l'actionneur retarde le décrochage tournant en poussant l'interface entre l'écoulement d'entrée et l'écoulement de jeu d'aube en aval vers l'intérieur du passage d'aube. Dans chaque cas, le pourcentage prédit par CFD de la réduction du débit massique du point de décrochage tournant concorde assez bien avec la valeur mesurée. Cependant, les simulations CFD surestiment le débit massique du point de décrochage tournant ainsi que l'augmentation de pression de l'étage centrifuge et sous-

estiment l’augmentation de pression de l’étage axial. Les principaux facteurs expliquant cette différence sont probablement les petites différences entre la forme simulée versus la forme actuelle de l’aube de rotor axial et l’incapacité de l’outil de simulation à bien capturer les pertes de pression totale dans la région près du moyeu du diffuseur sans aubes.

ABSTRACT

Rotating stall is a well-known aerodynamic instability in compressors that limits the operating envelope of aircraft gas turbine engines. An innovative method for suppressing the most common form of rotating stall inception using an annular DBD plasma actuator had been proposed. A DBD plasma actuator is a simple solid-state device that converts electricity directly into flow acceleration through partial air ionization. However, the proposed concept had only been preliminarily evaluated with simple numerical simulations on an isolated axial rotor using a relatively basic CFD code. The current project provides both an experimental and a numerical assessment of this concept for an axial compressor stage as well as centrifugal compressor stage that are both part of a low-speed two-stage axial-centrifugal compressor test rig.

The two configuration studied are the two-stage configuration with a 100 mN/m annular casing plasma actuator placed just upstream of the axial rotor leading edge, and the single-stage centrifugal compressor with the same actuator placed upstream of the impeller leading edge. The tested configuration were simulated with a sophisticated commercial RANS CFD code (ANSYS CFX) in which was implemented the latest engineering DBD plasma model and dynamic throttle boundary condition, using single-passage multiple blade row computational domains.

The experiments show that the casing plasma actuator reduces the mass flow of the last stable point (stall point) by 19.28% for the axial compressor stage and 28.39% for the centrifugal compressor stage for which the impeller is the source of rotating stall. The CFD simulations indicate that in both types of compressors the actuator delays the stall inception by pushing the incoming/tip clearance flow interface downstream into the blade passage. In each case, the predicted percentage reduction in stalling mass flow matches the experimental value reasonably well. However, the CFD simulations over-predicts the mass flow of the stall point as well as the pressure rise of the centrifugal stage and under-predict the pressure rise of the axial stage. The main factors for the difference are likely slight discrepancies between the simulated and actual axial rotor blade geometry deformation and the inability of the simulation tool to accurately capture the total pressure loss in the hub region of the vaneless diffuser.

TABLE OF CONTENTS

LIST OF TABLES

LIST OF FIGURES

NOMENCLATURE

AC	Alternative Current
AIRS	Abrupt Impeller Rotating Stall
B	Coefficient of Greitzer
C	Sound Speed
C_d	Discharge Coefficient
CEL	CFX Expression Language
CFD	Computational Fluid Dynamics
e	Experiment
ep	Experiment with Plasma
FFT	Fast Fourier Transform
IGV	Inlet Guide Vane
isen	Isentropic
K_t	Valve Closing Coefficient
l_c	Dimensionless Compressor Length
LE	Leading Edge
MIRS	Mild Impeller Rotating Stall
MIT	Massachusetts Institute of Technology
N	Rotational Speed of Compressor
NACA	National Advisory Committee for Aeronautics
NASA	National Aeronautics and Space Administration

P	Pressure
p	with Plasma
PIRS	Progressive Impeller Rotating Stall
PI4	A group of 15 undergraduate final year students for the 2012-2013 final-year integrated project in propulsion at École Polytechnique de Montréal
PR	Pressure Ratio
P_s	Static Pressure
P_T	Total Pressure
RANS	Reynolds Averaged Navier Stokes
RPM	Rounds per Minute
S	Static
S_c	Effective Section of the Compressor
SDBD	Single Dielectric Barrier Discharge
SST	Shear Stress Transport
T	Temperature
t	Time
TE	Trailing Edge
U_{tip}	Rotational Speed at Blade Tip
v	Fluid Speed
VDRS	Vaneless Diffuser Rotating Stall
V_p	Volume of Plenum

α	Absolute Flow Angle
ϵ	Dimensionless Time
λ_d	Debye Length
ρ	Density
Ψ_{TS}	Total to Static Pressure Rise Coefficient
Ψ	Dimensionless Pressure
φ	Dimensionless Mass Flow Rate

LIST OF APPENDICES

CHAPTER 1 INTRODUCTION

1.1 Background

The compressor forms along with the combustion chamber and turbine the three main components of a gas turbine but is usually the largest and heaviest component. It serves to compress the air before it enters the combustion chamber. The inherently positive pressure gradient in the flow direction renders its aerodynamic design highly challenging in terms of efficiency and aerodynamic stability. Its design has a direct impact on the performance and operating envelope of the engine.

To achieve the required pressure rise while limiting pressure gradients to avoid boundary layer separation on the blades, the compression is usually carried out over multiple stages. Each compressor stage consists of a rotating blade row (rotor) which increases both static pressure and absolute velocity of the fluid and a stationary blade row (stator) which diffuses the flow to transformed the increased kinetic energy into further static pressure rise. A compressor can be categorized according to the variation of the mean radius of the flow path. When this radius remains more or less constant, the compressor is of the *axial* type. On the other hand, when the mean flow radius increases significantly and the flow exits the rotor radially, the compressor is of the *centrifugal* or *radial* type and its rotor and stator are referred to as *impeller* and *diffuser*, respectively. A centrifugal compressor stage can achieve pressure rise that are several times that of an axial stage but at a lower adiabatic efficiency and incur a larger frontal area, which is less desirable for aircraft applications. Compressors that are between these two types are referred to as *mixed flow* compressors. A multi-stage compressor can be a combination of any of these types. However, large gas turbine engines usually use all axial stages while smaller engines typically use a combination of axial stages followed by a centrifugal stage.

The compressor performance is presented in a compressor map, as shown in figure 1.1, which is composed of a series of characteristic curves called *speedlines*, each of which is plot of pressure rise (pressure ratio or pressure rise coefficient) versus corrected mass flow for one particular rotation speed. Each speedline is delimited on the right by a choke condition and on

the left by the stall condition. Choking occurs when the flow is increased to the point where the pressure drops rapidly with increasing mass flow due to negative incidence on the rotor and stator blades and flow reaching choke conditions in their blade passages. The result is increased losses and a rapid drop in performance (pressure ratio and efficiency). On the other hand, a sufficient reduction of the flow causes the blades to stall from the increased incidence, resulting in aerodynamic instabilities in the form of *rotating stall* and *surge* that will be discussed in section 1.2.

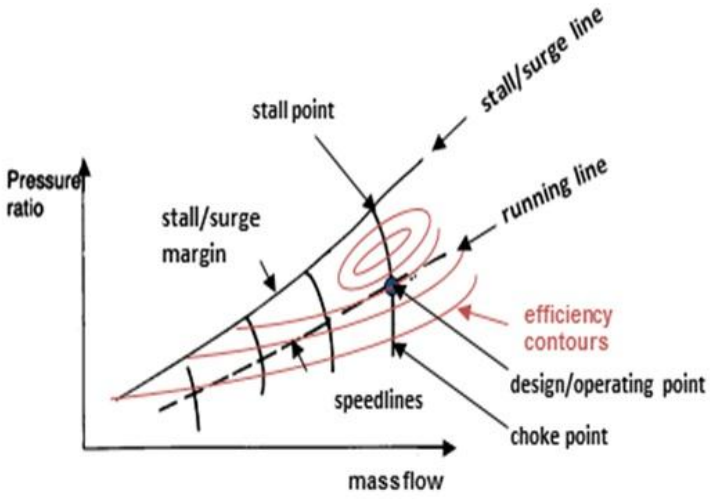

Figure 1.1: Compressor map

The curve that links the stall points of different speedlines is referred to as the *stall line* or *surge line*. Below this line, the speedlines are intersected by the *running line*, which is the line along which the compressor will operate when the engine is slowly accelerated or decelerated. The running line is set in the design through choking of the turbine. Its intersection with the speedline corresponding to the design rotational speed is the design or operating point of the compressor which should lie at or close to its peak efficiency. The running line can move up while the stall/surge line can move down under certain conditions such as transient operation and with engine wear. Consequently, a safety margin called stall margin or surge margin is left between the two lines which sacrifices compressor pressure ratio and possibly efficiency it displaces the design/operating point away from the peak efficiency point as illustrated in figure 1.1. Thus, there is great interest in technologies that can suppress compressor aerodynamic

instabilities and thus delay the stall point to lower mass flow so as to move the running line upward. The current research is aimed at assessing one such technology.

1.2 Compressor Aerodynamic Instabilities

As discussed in the previous section, compressor aerodynamic instabilities in the form of rotating stall and surge is the major factor in limiting the operating envelope of the compressor and of by extension of the gas turbine engine.

Rotating stall is the formation of a cell of velocity deficiency that rotates at a speed 20%-80% of the rotor speed [1], as illustrated in figure 1.2, and is usually accompanied by drop in pressure ratio and thus of engine performance. Two distinct types of rotating stall inception have been identified: long length-scale (*modal*) stall inception and short length-scale (*spike*) stall inception, which are illustrated in figure 1.3. Modal stall inception is characterized by the relatively slow growth over 10-40 rotor revolutions of a low-amplitude 2-D perturbation with circumferential wavelength on the order of the annulus into fully developed rotating stall cells. It has been shown both analytically and experimentally to occur at the zero-slope of the stagnation-to-static pressure rise characteristic (speedline) [2] of the entire compression system for which a positive slope is equivalent to negative damping of naturally occurring perturbations [3]. On the other hand; spike stall inception, which is more common in modern compressors, is characterized by the sudden appearance of a high-amplitude 3-D perturbation at the rotor tip with 2-3 rotor pitch[4] in circumferential wavelength. This perturbation grows rapidly within only two to five rotor revolutions into a fully developed rotating stall cell. This type of stall inception occurs at a negative slope of the stagnation-to-static speedline [5, 6], i.e. prior to the conditions for modal stall inception. Its rapid occurrence makes it harder to detect and control than modal stall inception. While spike stall inception is much less understood, the origin of the perturbation in the rotor tip region has linked it to tip clearance flow, i.e. the flow through the small gap between the rotor tip and compressor shroud. Compressors whose rotating stall is caused by tip clearance flow are usually referred to as *tip critical compressors*.

The drop in pressure rise associated with rotating stall means that the compressor can no longer maintain the necessary pressure in the combustion chamber. Thus, rotating stall usually triggers a much more severe aerodynamic instability in the form of surge. Surge is a one-

dimensional axisymmetric flow oscillation which, depending on its severity, can involve flow reversal across the engine, and cause not only a severe drop in engine power but also mechanical damage to the engine.

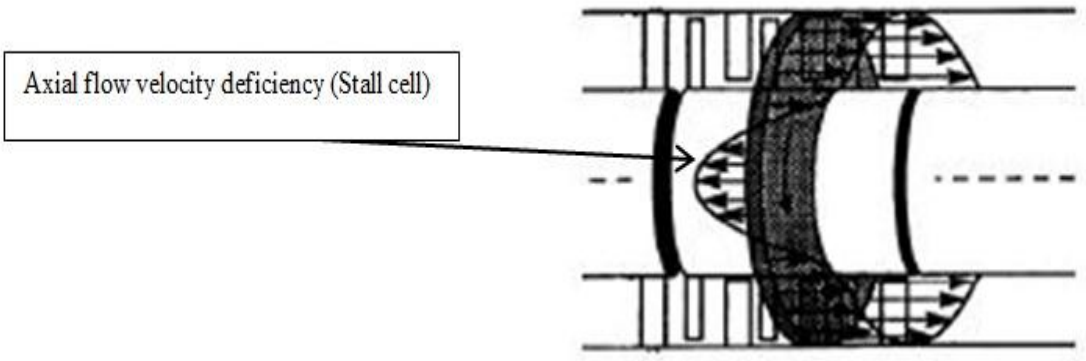

Figure 1.2: Rotating stall cell

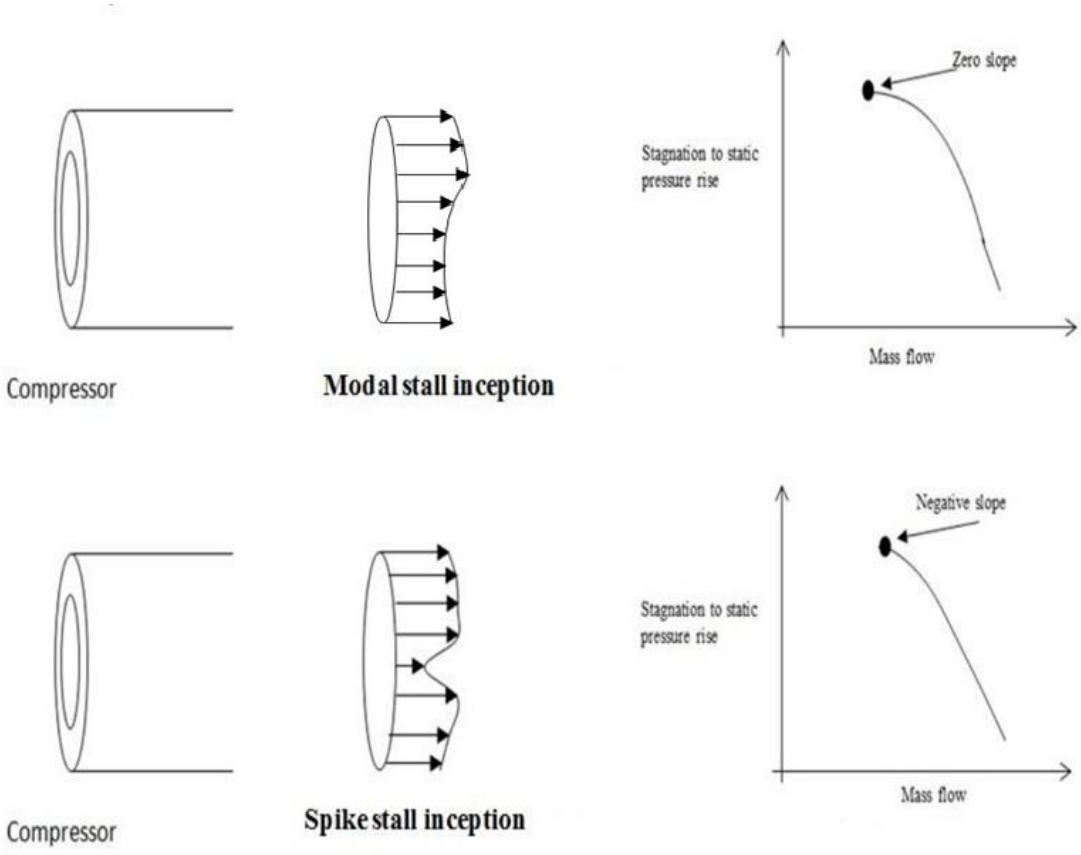

Figure 1.3: Two types of rotating stall inception

1.3 Rotating Stall Suppression

Given that surge is usually triggered by rotating stall, the suppression of aerodynamic instabilities starts with the suppression of rotating stall. Many passive and active rotating stall inception strategies have been tested.

Passive strategies do not require power input and mainly involve casing treatment, i.e. grooves and slots on the shroud above the rotor. However, while casing treatment has been shown to extend the stall/surge margin, it usually involves penalty in terms of efficiency and pressure rise at the design point [7]. Moreover, by their very nature, casing treatments are only effective for tip critical compressors which usually exhibit spike stall inception. Since this type of stall inception is not well understood, the design of casing treatment has been mostly empirical with no clear design rules to optimize stall margin while minimizing performance penalty.

On the other hand, active rotating stall suppression strategies require power input. However, this input can be kept low if the actuators are placed at strategic locations and designed to suppress the low-amplitude stall inception perturbations. More significantly, when implemented with a control feedback system, the actuator only needs to be turned on near stall which minimizes their negative impact on performance near the design point and further reduces power consumption. Most active control techniques have been successfully applied to delay modal stall inception for which the mechanism has been relatively well understood and analytically modeled since the 1980s. Moreover, the relative small growth rate and large wavelength of the pre-stall modal perturbations lends themselves better to detection and feedback control. These techniques include the use of circumferentially distributed movable inlet guide vanes [8], jet injectors [9] and tip jet injectors [10] to input out-of phase perturbations that suppress the growth of modal stall perturbations. Discrete micro-tip injectors aimed at the rotor tip clearance region have also been demonstrated, albeit without feedback control, to extend (Nie et al.[11], Deppe et al. [12]) on low-speed axial compressor test rigs. Despite their relative success, none of the tested active control strategies have yet been implemented in a commercial aircraft gas turbine engine. This absence can be attributed to the weight and costs associated with

integrating these mechanical and pneumatic actuators and their robustness (e.g. clogging of the jet injectors in a real aircraft working environment).

1.4 Problem definition

Vo [13, 14] used the advent of plasma actuation technology to propose an active rotating stall suppression concept primarily for spike stall inception that can potentially overcome these obstacles. A single dielectric barrier discharge (SDBD) plasma actuator is a thin solid-state actuator that converts electricity directly into flow acceleration via partial air ionization. As illustrated in figure 1.4, it essentially consists of two axially shifted electrodes, one exposed to the air while the other is hidden beneath a dielectric material. An AC voltage of several kilovolts and several kilohertz in frequency but at very low current (low power) placed across the electrodes results a strong electric field between the electrode that partially ionizes the air in a small region over the hidden electrode. The force on the ions (plasma) lying in this electric field cause them to accelerate and collide with neutral air particle resulting in a flow acceleration in a thin layer adjacent on the surface. More detailed information on the mechanism of DBD actuators can be found in references [15-17]. The electrical nature and simplicity of these actuators which are devoid of moving parts make them lighter, potentially more robust with higher bandwidth and easier to integrate than traditional mechanical and pneumatic actuators. In addition, since the exposed electrode is very thin and can even be made flush with the surface, DBD actuator has minimal if not zero detrimental impact on the flow when not in use. DBD actuators had been evaluated for a series of flow control applications mostly involving boundary layer separation suppression to delay wing stall [18-22] and reduce landing gear noise [23]. However, due to the limited strength of existing DBD actuators, experimental evaluations have been limited to relatively low speeds. The actuator strength is expressed as the induced axial force per unit actuator length.

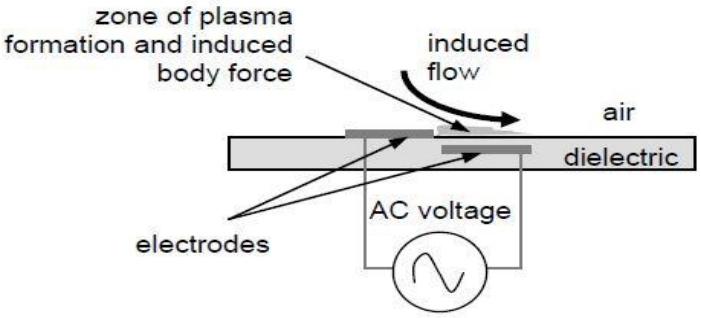

Figure 1.4: Configuration of electrodes in a plasma actuator

Vo [13, 14, 24] was the first to propose applying plasma actuators to suppress rotating stall. As shown in figure 1.5, his concept involves placing an annular DBD actuator on the shroud just upstream of the leading edge of a compressor rotor to accelerate the incoming flow to counter the effect of the tip clearance flow. The intended effect is somewhat similar to that of the discrete micro-injectors by Nie et al. [11, 25] and Deppe et al. [12] but more circumferentially uniform and devoid of mass addition and piping and other integration and robustness issues association with jet injection. While the results by Vo were very promising, his work was purely computational using a rather primitive CFD research code with a very basic (mixing length) turbulence model in which he implemented an engineering plasma actuator model. Furthermore, the simulations were limited to a single axial compressor rotor.

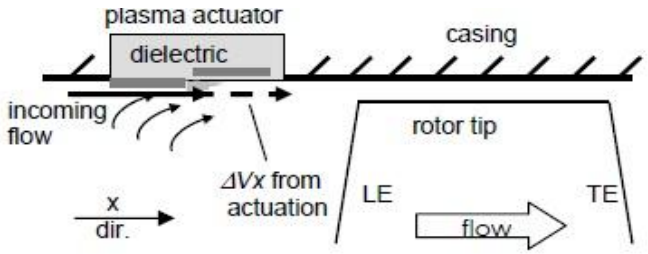

Figure 1.5: Stall inception suppression concept with plasma actuator proposed by Vo [13, 14, 24]

It remains to be seen whether the concept would work experimentally, even at low speed, on an axial compressor stage. Moreover, the applicability of the concept to centrifugal compressors should be assessed given that these compressors whose use has traditionally been restricted to small aircraft engines are likely to play an important role in future large aircraft turbofan engines whose increasing large bypass ratio lead to smaller engine core. Furthermore, it would be desirable to establish a more sophisticated computational tool validated with

experimental data that could be used to evaluate the concept for realistic aircraft engine compressor operating conditions for which the required actuator strength were estimated by Vo et al. [24] to be well above what can be achieved with existing DBD actuators.

1.5 Objectives

Based on the shortcomings of the work by Vo [13, 14, 24] as described in the previous section, the objectives of the present research are:

1. Demonstrate experimentally the concept of stall inception suppression with plasma actuation on a low-speed axial compressor stage and a low-speed centrifugal compressor stage.
2. Set up and validate a simulation tool for the concept based on a sophisticated (more accurate) commercial CFD code.

1.6 Thesis outline

Following the introduction to the research in this chapter, chapter 2 provides a brief literature review of rotating stall inception physics and relevant suppression methodologies. A review of DBD actuator models for CFD simulation is also provided. Chapter 3 presents the experimental setup and outlines the experimental and computational methodologies to obtain test data and corresponding numerical predictions on the effectiveness of the proposed plasma actuation concept for stall delay. Thereafter, the results from simulations and experiments are presented, compared and discussed in chapter 4. Finally, chapter 5 summarizes the conclusions of the current research and suggests improvements in future works.

CHAPTER 2 LITERATURE REVIEW

This chapter provides a review of the pertinent literature to this research. It will start with past work on stall inception mechanisms, followed by a more detailed summary of active rotating stall suppression strategies closely related to the concept studied in the current research. Finally, past research plasma actuation modelling and implementation in CFD simulations will be summarized.

2.1 Stall Inception Mechanisms

The first attempt to elucidate the mechanism behind rotating stall was done in the 1950s by Emmons[26]. As illustrated in figure 2.1, he proposed that a blade stall from a local increase in incidence would generate blockage in the local blade passage. The resulting divergence of flow to the two adjacent blade passages would increase the incidence to one neighbouring blade and decrease it for the other. The next blade would thus stall and decrease the incidence on the local blade, thus moving the stall cell circumferentially.

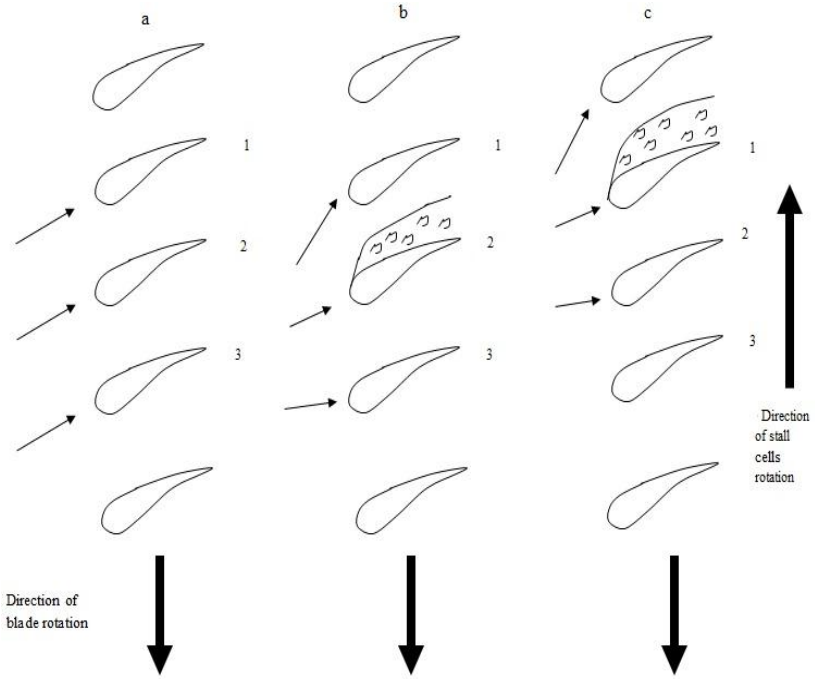

Figure 2.1: Rotating stall mechanism proposed by Emmons [26]

While intuitive, the mechanism proposed by Emmons was never proven and no significant work was done on explaining rotating stall until the 1980s when by Moore [3] and later by Moore and Greitzer [27] modeled a multi-stage compressor as an actuator disk with flow inertia. Their model showed that when the total-to-static pressure rise versus mass flow curve (speedline) reaches a positive slope, the damping of naturally occurring perturbations would be negative and these perturbations would grow to fully developed rotating stall cells. This type of stall inception was verified experimentally and would later be referred to as long length-scale or modal stall inception, which initiated much of the research into active rotating stall suppression technology, with the work listed in section 1.3.

However, the research in rotating stall took another turn when Day[6] experimentally discovered short length-scale or spike stall inception in the early 1990s. While this type of stall inception turned out to be much more common than modal stall inception, its highly localized nature with sudden appearance and rapid evolution made it hard to measure and predict. Through experiments on an axial compressor in which the inlet flow angle could be varied, Camp and Day [5] observed that spike stall inception seemed to occur at a constant inlet flow incidence angle for a particular geometry. They thus proposed that spike stall inception results from a 2-D type blade stall when the flow near the blade tip reaches a critical incidence. However, they could not provide any general quantitative criterion as to the value of the critical incidence nor the exact span location to evaluate it.

A few years later, using single and multiple blade passage simulations of an isolated axial compressor rotor, Vo [28, 29] proposed a new mechanism for spike stall inception that seemed to be consistent with previous experimental observations, as well as the first quantitative criteria to predict this type of stall inception. The proposed mechanism and criteria are based on tip clearance flow, which is the flow through the physical clearance between the rotor tip and the shroud that is driven by the pressure difference between the pressure and suction side of the rotor. Due to viscous and mixing loss within and at the exit of the gap, this flow has low relative stagnation pressure has high entropy contributing to loss in rotor pressure rise and efficiency. From the illustration in figure 2.2, as the tip clearance flow exits the tip gap, it encounters the low-entropy incoming flow at almost normal angles and forms an interface, which can be detected as a high entropy gradient region. The interface location is determined by a momentum

balance between the incoming and tip clearance flow. As one moves up the speedline, the mass flow and thus incoming axial flow velocity component decreases. The resulting increase in incidence strengthens the pressure difference across the blade and hence the tip clearance flow while the incoming flow is weakened. Consequently, the incoming/tip clearance flow interface moves upstream toward the leading edge plane.

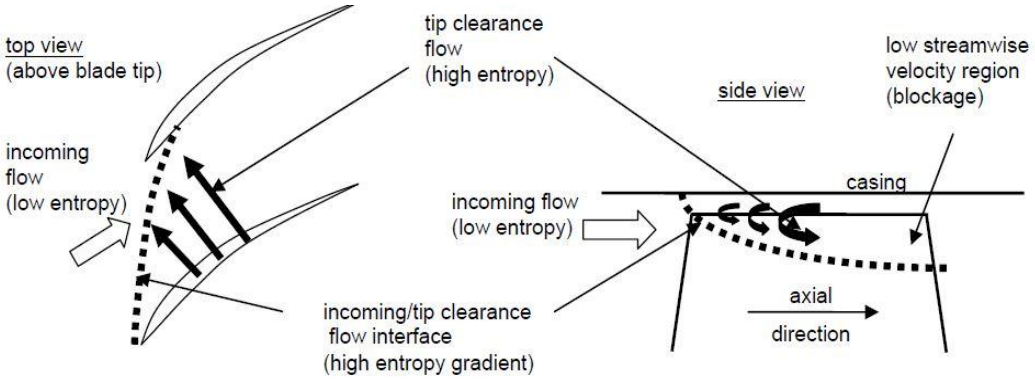

Figure 2.2: Interface between incoming flow and tip clearance flow [29]

In this context, and based on observations from his CFD simulations, Vo proposed two criteria for the formation of a short length-scale disturbance that leads to short length-scale rotating stall inception. These criteria are illustrated in figure 2.3. The first criterion (top illustration) is the incoming/tip clearance flow interface reaching the leading edge at the blade tip, which marks the onset of tip clearance flow spillage below and ahead of the blade tip leading edge into the adjacent blade passage. The second criterion is the onset of tip clearance fluid backflow at the trailing edge below the blade tip (detected as zero flow at the blade tip trailing edge), which would then impinge on the adjacent blade pressure surface (bottom illustration of figure 2.3). The proposed mechanism associated with these two criteria is shown in figure 2.4. Essentially, the impinging tip clearance fluid at the trailing edge (criterion 2) has a tendency to move upstream due to the positive pressure gradient along the blade passage but is forced by the incoming flow to either convect downstream or enter the adjacent blade tip clearance (double tip leakage). However, when the incoming tip clearance interface moves upstream of the leading edge at the blade tip (criterion 1), the spillage at the leading edge represents a path of lower resistance that downstream convection or double leakage that allows unhindered upstream movement of the impinged tip clearance flow that results in the formation of a spike. As such, Vo showed from his simulations that both criteria are required and reasoned that if one of the

two criteria could be suppressed, then spike stall inception could be delayed until both are satisfied at a lower mass flow.

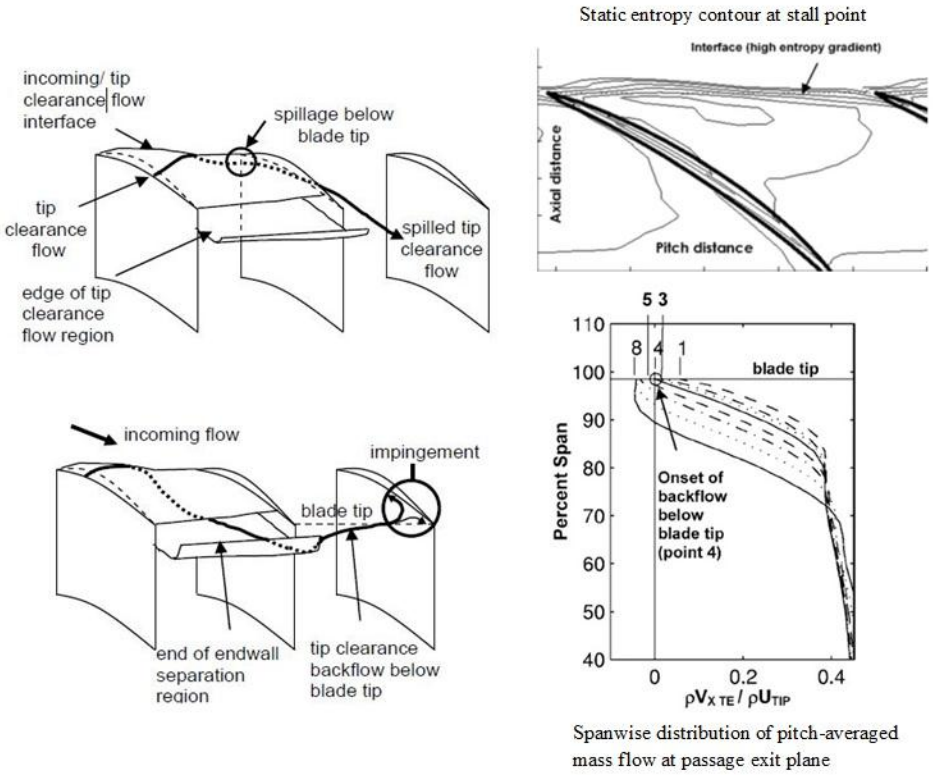

Figure 2.3: Criteria for spike stall inception[29]

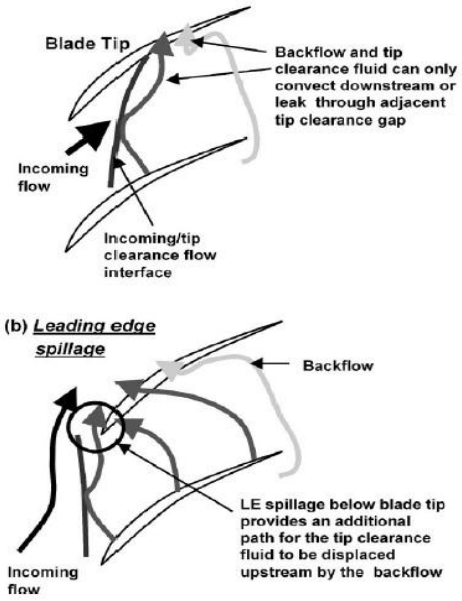

Figure 2.4: Proposed mechanism for spike stall inception [29]

Through this work, Vo [28] also suggested that should the two criteria occur in a particular rotor before the total-to-static speedline of the *entire* compressor reaches a zero-slope peak, then the compressor would exhibit spike stall inception. Otherwise, the compressor would exhibit modal stall inception. Furthermore, despite the proposed central role of tip clearance flow in spike stall inception, Vo infer that tip clearance flow can also play a role in modal stall inception if the losses it generates causes the total-to-static speedline of the compressor to turn over and reach zero-slope before criteria for spike stall inception are met.

Although the trailing edge backflow criterion (criterion 2) has yet to be widely accepted, many subsequent work by other researchers on different geometries seem to corroborate the leading edge spillage criterion (criterion 1) both through CFD simulations [30] and experiments [12, 31], which point to criterion 1 being generic.

While a lot of research has been carried out on rotating stall in axial compressors, much less research has been carried out for centrifugal compressor. Japikse [32] summarized the knowledge on centrifugal compressor stall. Rotating stall in centrifugal compressors can be triggered by the impeller or the diffuser. Three types of rotating stall are associated with the impeller, namely mild impeller rotating stall (MIRS), abrupt impeller rotating stall (AIRS) and progressive impeller rotating stall (PIRS) while only one type is known for diffusers, namely vaneless diffuser rotating stall (VDRS). For the first type of stall in impeller (MIRS), there is no clear theoretical explanation. However it is considered as a precursor of (VDRS). (AIRS) is characterized by large amplitude oscillations in velocity and pressure upstream and downstream of the impeller, and can occur at negative or positive slope of the pressure rise characteristic. Very little is known about (PIRS), beyond the fact that the amplitude of the perturbations grow progressively. The important parameters which have been associated with rotating stall in impeller are tip incidence, impeller outlet blade angle and leading edge to throat velocity ratio. However, there are no reliable prediction criteria for the onset of impeller rotating stall. Similarly, there are no generic prediction tools for diffuser stall, but the parameters affecting VDRS are the diffuser length, width, inlet-to-throat area ratio and the vaneless extent and the number of vanes for vaned diffusers and their designs can affect the flow pattern and stall onset in diffusers.

2.2 Relevant Active Rotating Stall Suppression Methodologies

Section 1.3 provided a general summary of rotating stall suppression technologies. This section provides a more detail review of the active rotating stall suppression technologies closely related to and including the concept studied in this research.

Many active control concepts have been tested for modal stall inception, which is easier to detect and whose slower evolution puts lower requirements on actuator bandwidth. On the other hand, the more recently discovered and less understood nature of spike stall inception, along with the rapid evolution of spike perturbation means that much fewer work has been done on spike stall inception outside of casing treatments whose empirical development have preceded even the discovery of modal stall inception.

Day [33] was arguably the first to work on supressing spike stall inception after he discovered it. Given the location of the spike perturbation, he experimentally applied small air jets in the rotor tip gap region upstream of the first rotor of a four stage low-speed axial compressor. The air injection system was in the form of an array of 12 equally spaced individually controllable valves, hinged along one side as shown in figure 2.5, i.e. about one injector per five rotor blade pitch. The valves are flush with the outer casing of the annulus when closed. Emerging localized spike-type stall cells were found to be removed by air injection in their immediate vicinity, doing this repeatedly improved stall margin by 6 percent.

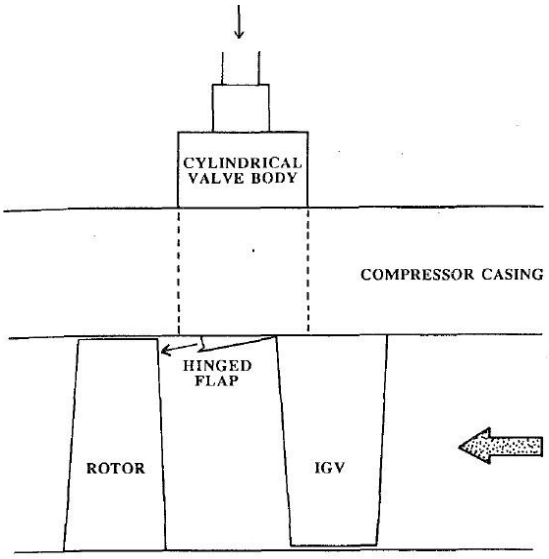

Figure 2.5: Schematic picture of air injection valve used by Day[33]

Deppe et al.[12] also experimentally applied discrete micro-injection in the tip clearance region of three low-speed single-stage axial flow compressors. The air injectors consisted of small 2 mm diameter tubes located 3 mm upstream of the rotor tip at leading edge in two different configurations (with 8 nozzles and with 16 nozzles). It was found that 16 nozzles (1 per blade pitch) are more effective in terms of stall margin extension. Their best result was a 20% reduction in stalling mass flow for an injection of 0.286% of the incoming mass flow. In a parametric study the radial position of the nozzles were changed, increasing the radial distance measured from casing wall caused a significant reduction in performance improvement, thus indicating that spike-type stall is linked to tip clearance flow. In a similar study injection angle was varied, for positive jet angles (against rotor rotation) stall flow rate remained almost constant, but for negative angles (in direction of rotor rotation) stall mass flow rate was even higher than the stall flow rate without injection.

Nie et al.[11, 25] improved on the tip injection concept by using flush-mounted discrete micro-air injectors which can be rotated in yaw as shown in figure 2.6. The injectors can be mounted at different axial positions. In their first study of 2002 [11] they reduced stall mass flow by 5.83% on a low-speed three-stage axial compressor using four injectors equally spaced circumferentially with 7mm axial gap upstream of the first rotor injecting 0.056% of design mass flow rate. In a subsequent study using the same injectors on this compressor and a higher speed compressor, Nie et al [25] found that the optimum axial location and yaw angles for the

injections depends on injection flow rate and compressor speed and with injection just downstream of the rotor leading edge and axial direction preferable for low speed and low injection rate and injection at rotor leading edge turned toward the direction of rotating better for high speed compressors.

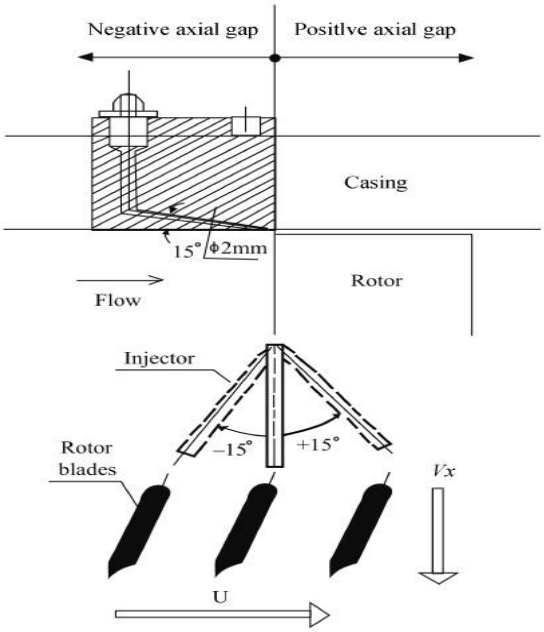

Figure 2.6: Injector axial position and definition of yaw angle[11, 25]

It is noted that all of the above techniques aimed at supressing spike stall inception by using air injection to add axial momentum to the incoming flow in the tip region. As such, one can infer from their success that they probably work by pushing the incoming/tip clearance flow interface downstream back into the blade passage and thus delaying of the first stall criterion for spike stall inception proposed by Vo [28]. However, the injection concepts have many inconveniences that prevent their application in a real aircraft engine operating environment. First, the required high-pressure air must be taken from downstream stages in the compressor which imposes an efficiency penalty on the engine. Second, the recirculated air from aft stages is also hot which may increase tip clearance gap from shroud thermal expansion[34], further degrading performance and reducing stall margin. Third, while both previous factors can be minimized with very small injection, the micro injection system would be highly vulnerable to clogging from the dirty operating environment that can only be prevented though expensive

maintenance. Last but not least, the integration of such pneumatic systems with pipes and valves adds complexity and weight to the engine.

It is in this context that Vo [13, 14] proposed the concept of placing an annular plasma actuator on the casing just upstream of the rotor leading edge to accelerate a thin layer of incoming flow adjacent to the shroud in order to push the incoming/tip clearance flow interface downstream and in doing so suppress spike stall inception, as shown in figure 2.7. To evaluate this concept, Vo implemented a plasma actuator model in the form of a basic steady linear [13] and non-linear[14] spatial body force distribution and a more sophisticated distribution into a basic cell-centered RANS CFD research code (UNSTREST by J. Denton of the University of Cambridge). He simulated the low-speed compressor rotor used in his spike stall inception study [28, 29] without and with plasma actuator placed different actuator axial locations at low (Mach 0.2) and medium (Mach 0.5) circumferential tip speed. He showed that the plasma actuator delays stall by moving the incoming/tip clearance flow interface downstream and is most effective when placed just upstream of the rotor leading edge, in this case at 7% chord upstream. At low tip speed (Mach 0.2), an actuator strength on the order of 100-200 mN/m would be required to achieve a drop of about 8% in the stall mass flow, which is higher than the strength achievable with the first generation of plasma actuators (20-30 mN/m). Moreover, the effectiveness decreases with speed and the actuator strength requirement scales roughly with speed. Vo et al. [24] repeated the simulations for a different (transonic) compressor rotor which showed similar conclusions.

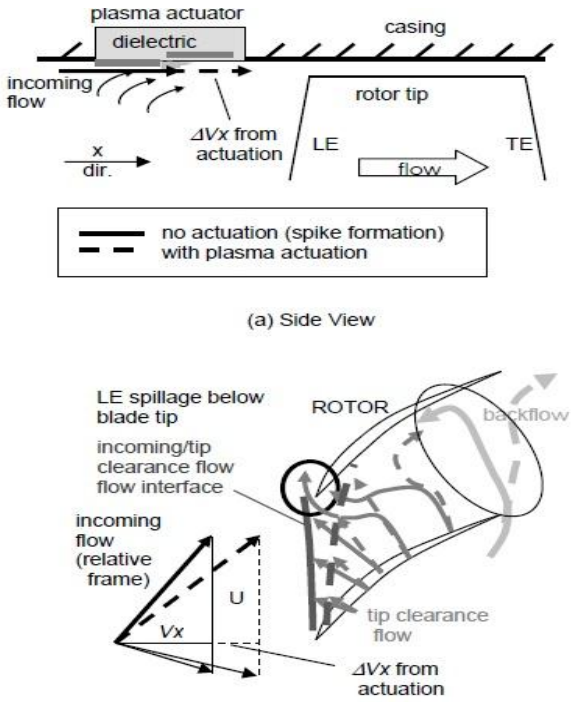

Figure 2.7: Concept of plasma flow actuation for suppression of rotating stall inception [13, 14, 24]

Jothiprasad et al. [35] later simulated the same concept studied numerically using a simple linear body force distribution as the plasma actuator model implemented in a 3D RANS solver developed for turbomachinery. However, their objective was to assess the effect of the directionality of actuation. An annular DBD plasma actuator with an actuator strength of 260 mN/m was positioned at 7% chord upstream of a low-speed compressor rotor (left of figure 2.8). Subsequently, axial sections of DBD actuators are placed at intervals around the circumference axially to turn the incoming flow circumferentially in or against blade rotation (right of figure 2.7), these two cases would respectively decrease and increase rotor tip incidence. Their results indicated that only the actuation in the direction of rotation is ineffective, which implies that tip incidence reduction is not crucial for stall margin enhancement. This lends credence to the mechanism of stall suppression proposed by Vo in figure 2.7. Motivated by the effects observed at low-speed, a further study at transonic speeds was done on the NASA Rotor 37, axial transonic compressor rotor. It was found that an actuation strength of 5.24 N/m would be needed to extend 7.6% the stalling mass flow.

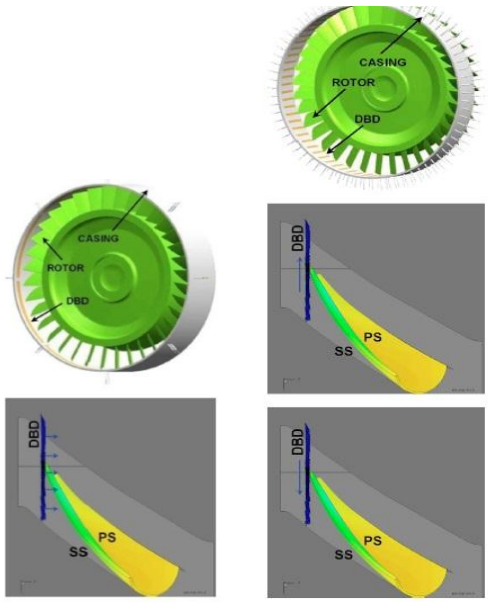

Figure 2.8: DBD actuator for downstream force. Forcing region and direction in blue [35]

It must be noted both Vo [13, 14, 24] and Jothiprasad [35] used an exit static pressure boundary condition for the computational domain. As such, they could not obtain the new stall point with plasma actuator should it lie past the zero-slope peak of stagnation-to-static pressure rise characteristic of the simulated rotor.

In the case of centrifugal compressors, Nie et al. [25] also experimentally implemented the micro tip injection concept to a low-speed centrifugal compressor with 19 impeller blades and 15 diffuser vanes as shown in figure 2.9. Eight injectors were applied at each of the positions 2 and 3 while five equally spaced injectors were used at position 4. Two injected mass flow rates were applied, namely 0.942% and 0.579% of the stall mass flow rate. The authors found that the position where injection is most effective may be different according to the amount of injected air. At the higher injected mass flow rate position 2 was found the best location by providing a decrease of 10% in stall mass flow rate with rotating stall detected in the inducer (upstream part of impeller) one can infer that the application of injection at this position works by affecting tip clearance flow. For low injected mass flow rates, injection at position 4 was found to be the most effective as it is inferred to reduce flow incidence to the diffuser. Finally injection at position 1 with 0° yaw did not show a significant extension in stall margin. This could be caused by not injecting air in the tip clearance gap since figure 2.9 shows that the head of the injection tube is below impeller leading edge tip.

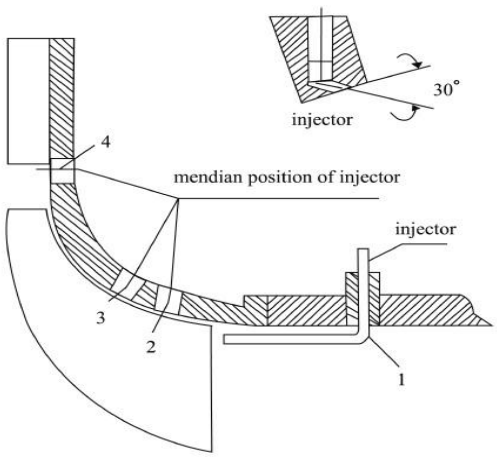

Figure 2.9: Micro injector applied to centrifugal compressor by Nie et al. [25]

In another study, Skoch et al. [36] experimented steady jet injection at the shroud into the vaneless region just upstream of the vanned diffuser of a 4:1 pressure ratio high-speed centrifugal compressor stage. Several parameters such as injection angle, injection flow rate, injector spacing and injection versus bleed were investigated, compressor discharge and external source were used as the air supply. In addition, the effect of the flow obstruction by a tube inserted in diffuser vaneless space through the shroud was also studied. Figure 2.10 depicts the setup. Three different stabilizing methods were investigated. The results showed that forward-tangent injection using recirculated air resulted in a little pressure loss in the diffuser and a small improvement in surge margin while reverse-tangent injection produces higher losses in stage pressure ratio for a similar stall margin improvement. However, control tubes provided the greatest surge margin improvement while with moderate pressure loss in the diffuser. The improvements produced from all methods are results of the span-wise reduction of average swirl angle which in turn causes: a reduction in diffusion between the impeller exit and the diffuser throat; a reduction of incidence on the diffuser vane leading edge; and the elimination of backward rotating perturbation. One can thus infer that a rotating stall control concept in the vaned diffuser of a centrifugal compressor should aim to reduce average swirl angle while keeping pressure loss in minimum level.

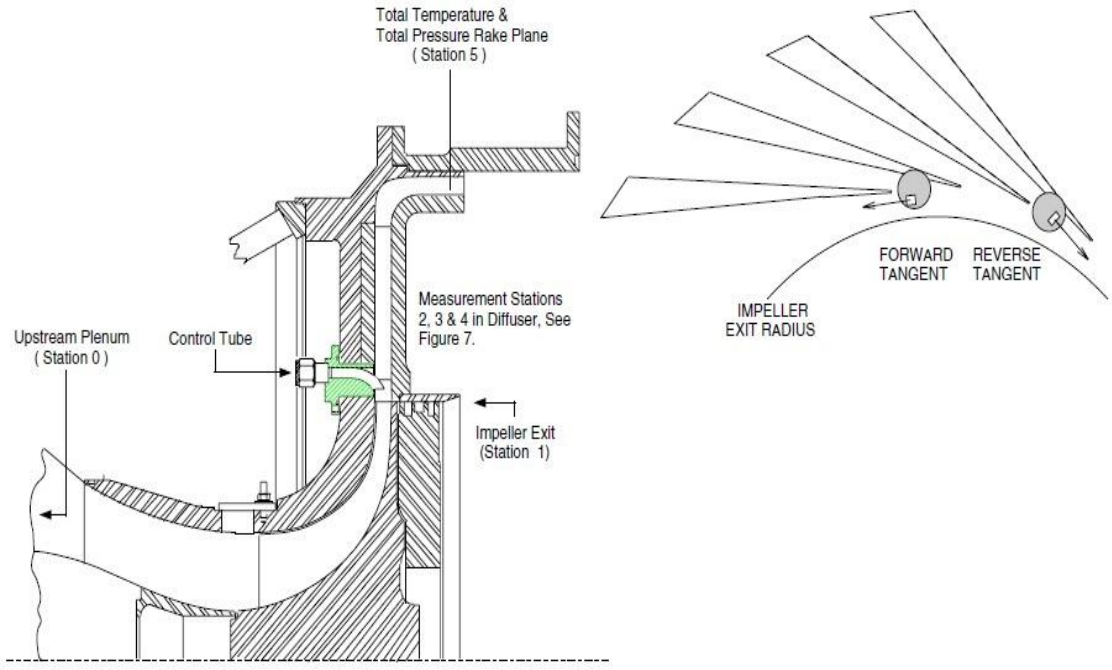

Figure 2.10: Cross section of test compressor and control tube (left), shroud side injector orientations (right) [36]

2.3 Plasma actuator modelling

Computational fluid dynamics (CFD) has played a key role in the development of new plasma actuation concepts by providing the tools to evaluate their feasibility in terms of actuation requirements at realistic operating conditions as well as to assess whether the currently available actuator strength is sufficient to justify an experiment. Such an assessment is required in the current research before setting up the experimental demonstration of the casing plasma actuation concept for rotating stall suppression. The use of CFD simulation requires an adequate model of the DBD plasma actuator.

The models of DBD plasma actuators can generally be separated into two different categories. The first category includes complex models which couple the governing equations of motion for ions and electrons to the flow equations. These models have been developed by Roy et al. [37] , Jayaraman et al. [38] and Gaitonde et al. [39]. However, these models are highly computationally intensive even to simulate a simple two-dimensional actuator in quiescent flow on a flat plate. Thus, they cannot be used for simulations of flow control applications on realistic shapes in the near future.

The other category consists of engineering models which simulate the effects of the DBD actuator on the flow by an equivalent spatial body force distribution that can be implemented as a source term in the CFD code. Shyy et al. [40] developed the simplest of these models by using a time-averaged linear two-dimensional body force distribution in terms of the actuator size and input voltage amplitude and frequency, which was used by Vo [13] (initially) and Jothiprasad et al. [35] to simulate their concepts. However, this model highly over estimates the actuator strength for a given voltage and frequency input. Suzen et al. [41] later developed a more sophisticated model that produces a (non-linear) more realistic body force distribution (when compared to the results from the complex models) based on actuator geometry and the nature of the fluid and dielectric material. This body force distribution is then modulated in time with the alternating voltage input. This model was used by Vo in his later studies [13, 14, 24] of the plasma actuation concept for rotating stall suppression. Orlov et al. [42] used a network of electrical elements to model the dynamics of the glow discharge (plasma) region over the hidden electrode to capture the unsteady charge distribution over this electrode due to plasma formation, advancement and retreat over the input cycle. Lemire and Vo [23] combined the best element of previous models [41, 42] to obtain a more accurate spatial and time variation of the induced body force. Figure 2.11 shows a spatial body force distribution obtained by Lemire et al. [23] from their model, which they assessed to be very similar to that from one of the complex models. An evaluation of the different engineering models by Palmeiro and Lavoie [43] showed that this is the best engineering model of DBD actuators so far.

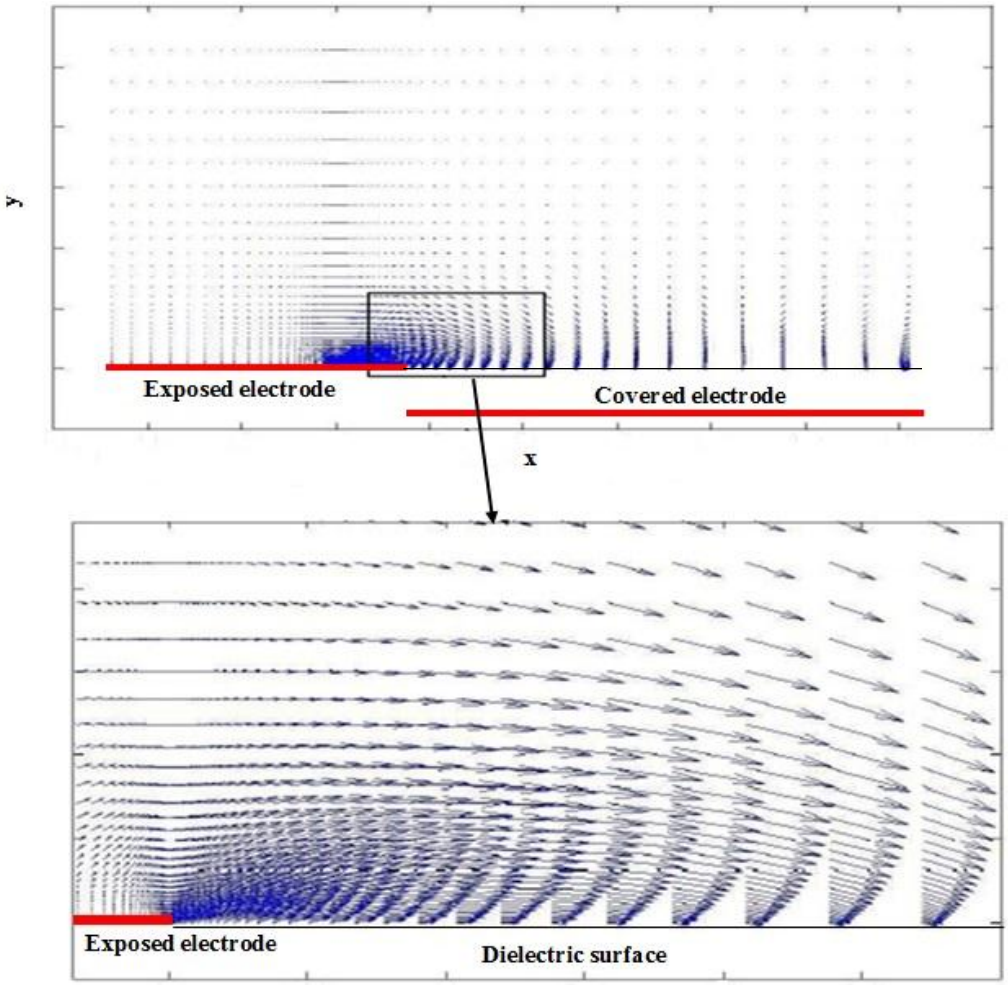

Figure 2.11: Spatial body force distribution from model of Lemire et al. [23] (x and y are in mm, x=0 is the edge of the exposed electrode, and y=0 is the dielectric surface).

While a time-varying spatial body force should in principle be implemented in CFD simulations to reproduce the effect of the AC input to the actuator, virtually all flow control simulations so far in the literature with DBD actuators use a constant (time-averaged) spatial body force distribution. This distribution can be scaled so that the integral value in the x-direction matches the desired actuator strength. This steady approach is justified a relatively slow flow velocities where the flow convection time over the actuator is much slower than the time period of the DBD actuator input, meaning that from the point of view of the flow, the actuator appears to be operating in steady state.

CHAPTER 3 METHODOLOGY

The general methodology taken in this research is to set up and use a numerical tool based on a commercial CFD code and an engineering plasma actuator model to assess the feasibility of testing the casing plasma actuation concept on an existing low-speed compressor test rig. The experiments are subsequently carried out to verify the numerical prediction and validate the tool. Given that the simulations are constrained by the compressor test rig and plasma actuator, this chapter starts with a description of the experimental setup, followed by the numerical setup and simulation and testing procedures.

3.1 Experimental setup

The compressor test rig used for the current research is a low-speed two-stage compressor composed of an axial stage and a centrifugal stage with a vaneless diffuser. This rig was designed and built by a group of 15 undergraduate final year students for the 2012-2013 final-year integrated project in propulsion at École Polytechnique de Montréal. The blade rows and casing fabricated in plastic by stereolithography, making it easier to integrate DBD plasma actuators for which the casing can be used as the main dielectric material. A photograph of the rig is shown in figure 3.1. The compressor is driven by a 0-8900 rpm 7.7 HP Baldor-Reliance AC electric motor and drive.

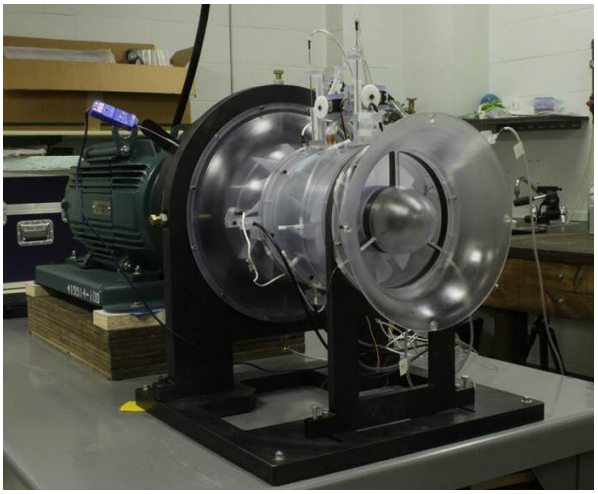

Figure 3.1: Low-speed axial-centrifugal compressor test rig with instrumentation

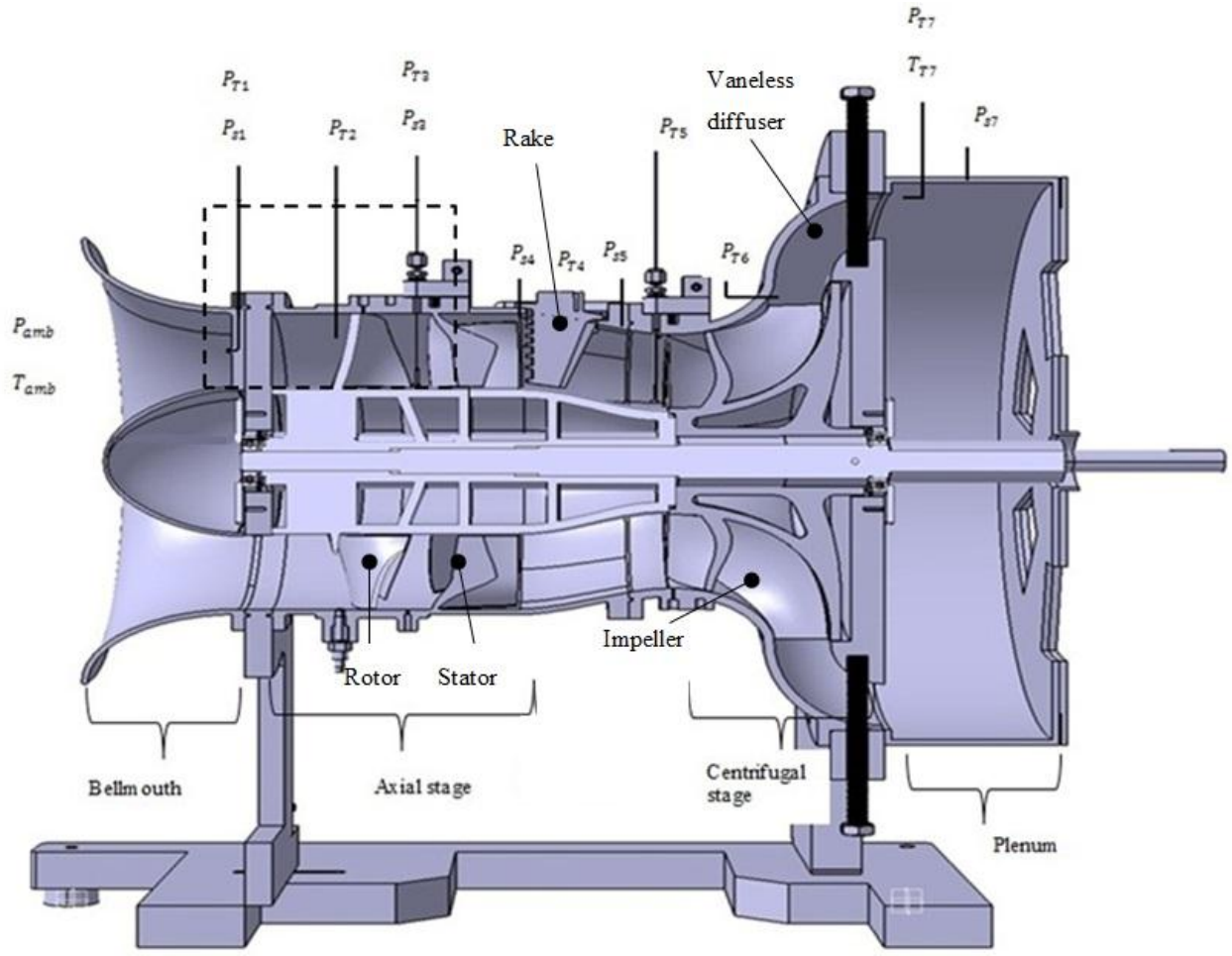

Figure 3.2: Side view cross-section of compressor test rig with instrumentation

Figure 3.2 presents a cross-sectional side view of this two-stage axial-centrifugal compressor, along with the instrumentations, which will be discussed later. The flow enters axially through a Bellmouth with three struts into an axial compressor with constant hub and tip radii. The hub rotates with the rotor such as the stator has a hub clearance. The axial flow exiting the axial stage then enters an impeller and vaneless diffuser that dumps the swirling flow into a plenum. The plenum extremity is made up of two plates, each having six openings of same shape and area. One plate can slide past the other to vary the opening area and thus control the mass flow rate through the compressor. While the compressor was originally designed to operate at a corrected speed (N_c) of 7200 rpm, the operating corrected speed was reduced to 4400 rpm for the current research to allow for the plasma actuator of limited strength to have a more noticeable effect. The main design characteristics of each stage of the compressor at either speed are shown in tables 3.1 and 3.2. It is noted that design parameters at N_c=4400 rpm correspond to peak

efficiency conditions at this speed. The rig is designed such that the axial stage can be removed and replaced with a bladeless hub and shroud in order to run the centrifugal compressor alone.

Table 3.1: Design parameters of the axial compressor stage

Parameter	**N_c=7200 rpm**	**N_c=4400 rpm**
Design corrected mass flow (kg/s)	0.5112	0.3016
Design stagnation pressure rise coefficient	0.3839	0.3950
Design efficiency	0.9456	0.8625
Rotor circum. tip speed (m/s)	66.8	40.8
Tip radius (mm)	88.90	
Hub radius (mm)	44.45	
Number of blades (rotor/stator)	12/14	
Rotor tip clearance/stator hub clearance (mm)	0.381/0.381	

Table 3.2: Design parameters of the centrifugal compressor stage

Parameter	**N_c=7200 rpm**	**N_c=4400 rpm**
Design corrected mass flow (kg/s)	0.5112	0.3016
Design stagnation pressure rise coefficient	2.404	2.341
Design efficiency	0.8976	0.8959
Impeller inlet circum. tip speed (m/s)	57.3	35.0
Impeller tip radius inlet/exit (mm)	76.2/107.95	
Impeller inlet hub radius/exit blade height (mm)	31.75/26.20	
Number of blades (impeller)	12	
Impeller tip clearance (mm)	0.381	
Vaneless diffuser inlet radius (mm)	107.95	
Vaneless diffuser exit radius (hub/tip) (mm)	133.35/159.18	

Instrumentation

As shown in figure 3.1 and summarized in table 3.3 the instrumentation on the compressor rig mainly consists of static pressure taps, total pressure probes and thermocouples. The static pressure taps are placed on the casing at different axial position, including at the exit of every blade row. At each axial position, the taps are spaced out circumferentially and connected together to obtain an average static pressure. At the exit of the stator, the taps are spaced so that different pitch positions with respect to the stator blades are covered by the circumferential taps to get a meaningful average.

The total pressure probes include Kiel probes placed at the exit of the rotor, impeller and vaneless diffuser (P_{t3}, P_{t6}, P_{t7}) with radial traverses powered by servos. A homemade pitot tube with radial traverse is also placed just upstream of the impeller. Just downstream of the stator lies a total pressure rake with seven holes radially spaced out to cover seven equal area portions of the annulus. The rake can in be positioned circumferentially with respect to the stator blade pitch to obtain a two-dimensional distribution of the total pressure distribution at the stator exit plane.

Four type-T thermocouples, read through a NI 9211 unit, were used. Two thermocouples, calibrated in a constant temperature bath to ± 0.1°C accuracy, were placed upstream on the Bellmouth intake to measure ambient (inlet) total temperature and in the plenum to obtain the exit temperature for efficiency estimation of the two stage compressor or the centrifugal compressor when the latter is operated alone. The efficiency of the axial stage could not be measured because the temperature rise across the stage is too small making the measurement uncertainty too significant. The other two uncalibrated (± 1°C in accuracy) thermocouples were used to monitor the temperature of the two bearings.

The pressures (relative to the atmospheric pressure) were measured with a 16-channel Netscanner 9116 from with a range of 0-1 psi and a precision of ± 3.4 Pa. The ambient conditions were read through an Arduino board from digital sensors placed below the compressor rig, namely a Bosch BMP085 for atmospheric pressure whose range and precision are respectively 30-110 kPa and ± 0.3 kPa, and a AM2302 probe for relative humidity (0-100% ± 3%). The rotational speed was visually read from the motor drive display and is accurate to ± 1 rpm.

The static and total pressure and temperature measurements along with the rotational speed and atmospheric conditions allow calculations of the pressure rise coefficient. Moreover, the static pressure at the Bellmouth exit in combination with the atmospheric pressure (which is the corresponding inlet total pressure) were used to calculate the mass flow using correlations for the discharge coefficients C_d obtained from the rig designers. The details of the calculations of the main parameters can be found in Appendix A and were implemented in a LabView program created by the rig designers for real time display of the measured speedline.

Other instruments include three optical tip clearance sensors and three high-speed (Kulite) pressure sensors, placed at the rotor leading edge, impeller leading edge and impeller trailing edge. The tip clearance probes were supposed to measure the change in tip clearance size due to rotor and impeller blade deformation under rotation. However, they did not work reliably and the deformation obtained from finite element simulations in ANSYS during the blade design was substracted from the static tip clearance (measured with feeler gauges) to give the tip clearance values under rotation given in tables 3.1 and 3.2. Similarly, the Kulite sensors installed to detect perturbations associated with rotating stall inception and fully developed rotating stall proved ineffective due to the signal to-noise ratio at the low-speed operation. Instead, a thin string was hanged from the shroud just upstream of either the rotor or the impeller, as shown in figure 3.3a, when the centrifugal stage is operated alone. As illustrated in figure 3.3b, the string points downstream when the operating point is stable. Near stall, the string would oscillate a little bit while still pointing downstream, lightly due to tip clearance flow oscillation often observed as one approaches the stall point [44]. When rotating stall occurs, this string would abruptly oscillate back and forth.

Table 3.3: Measurement instrumentations installed on the compressor

P_{amb}	T_{amb}	P_{T1}	P_{s1}	P_{T2}	P_{T3}	P_{s3}	P_{s4}
Ambient pressure	Ambient temperature	Total pressure at Bellmouth	Static pressure at Bellmouth	Total pressure at Rotor inlet	Total pressure at Rotor outlet	Static pressure at Rotor outlet	Static pressure at Stator outlet
P_{T4} **(Rake)**	P_{s5}	P_{T5}	P_{T6}	P_{T7}	T_{T7}	P_{s7}	
Total pressure rake at stator outlet	Static pressure at Impeller inlet	Total pressure at Impeller inlet	Total pressure at Impeller outlet	Total pressure at Plenum	Total temperature at Plenum	Static pressure at Plenum	

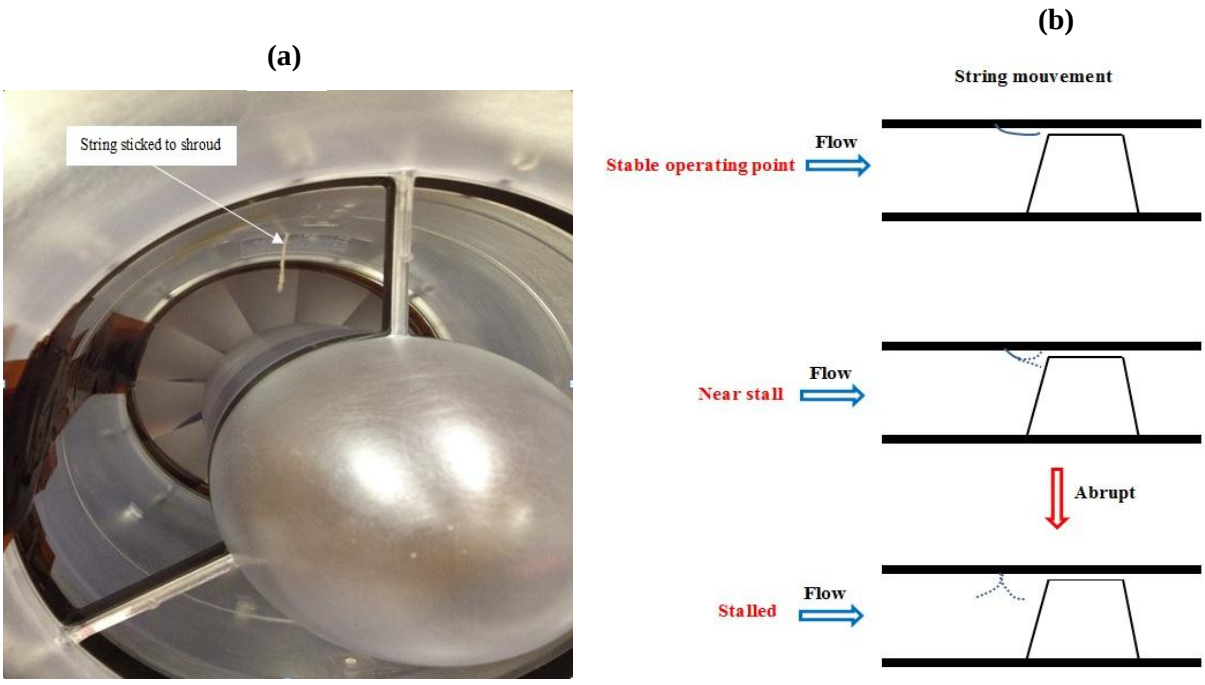

Figure 3.3 : String for rotating stall detection

Plasma actuator

The annular casing plasma actuator used in the experiments were built by using the material of the casing (5-mm thick DSM Somos WaterShed XC 11122 photopolymer) as the main dielectric material and 0.0035 in. thick self-adhering copper foil tape for the electrodes. Layers of 0.001 and 0.005 in. thick Kapton tape cover either side of the main dielectric material increase the electrical insulation and to protect the photopolymer from wear/degradation under repeated plasma formation. Figure 3.4 illustrates the geometrical layout and positioning of the DBD actuator for the axial rotor. The 25.4 mm wide hidden electrode is placed on the outside of the casing and is completely covered with Kapton tape to avoid the formation of parasitic (non-useful) plasma on the outer casing. The 6.35 mm wide exposed electrode is placed on the inner casing without overlap with the edge of the hidden electrode. Its downstream edge lies 5 mm (11.25% of rotor tip chord) upstream of the blade tip leading edge. The upstream half of the exposed electrode is covered with Kapton tape to avoid parasitic plasma at its upstream edge. A similar setup (figure 3.5) is used for the impeller of the centrifugal compressor stage. It must be noted that in either case, the annular DBD actuator does not cover the full 360°, but skips three small circumferential sections of about 10° each to avoid two mounts instrumentation mounts and to provide space for connecting the electrode to the high-voltage generator.

The physical layout of the DBD actuator used in this experiment was determined based on Thomas et al. [18] and past tests done by the research group at Polytechnique, updated with trial and error on the Watershed 11122 photopolymer. The aim was to obtain about 100 mN/m actuator strength for continuous operation over 30 seconds at a time without damaging the actuator. The methodology used to measure the actuator strength and to determine the required input AC voltage and frequency are described in Appendix B

Two experimental configurations were tested in the current research. The first is with the two-stage axial-centrifugal compressor with the plasma actuator applied only to the axial compressor rotor. The second configuration is with the centrifugal compressor stage operating alone with the plasma actuator applied to the impeller.

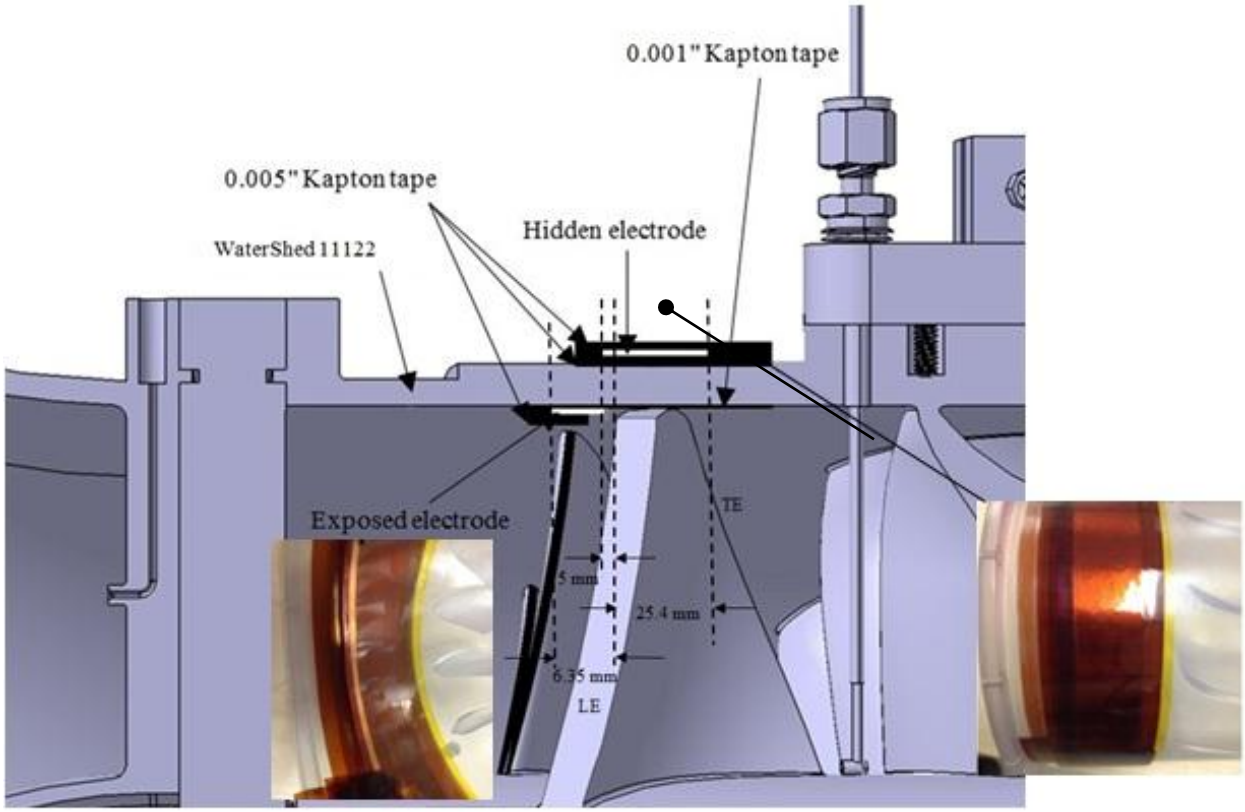

Figure 3.4: Profile of actuator installed on the casing for the axial rotor

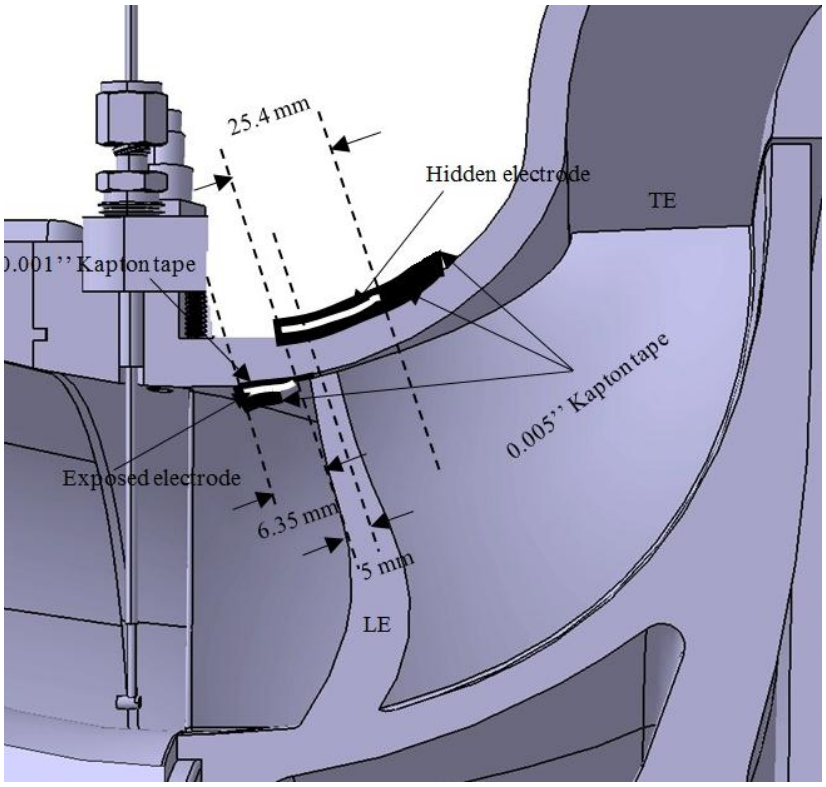

Figure 3.5: Profile of actuator installed on the casing for the impeller

3.2 Numerical setup

The simulations of the compressor test rig described in section 3.1 are carried out using ANSYS-CFX Version 13, a sophisticated commercial finite-volume Reynolds Average Navier-Stokes (RANS) CFD code widely used for turbomachinery. User defined functions can be added to ANSYS CFX via CFX Expression Language (CEL) written by the user in FORTRAN. In this case, the CEL is used to implement a DBD plasma actuator model and a more sophisticated throttle exit boundary conditions that can capture points beyond the zero-slope peak of the total-to-static speedline. The DBD plasma actuator model used takes the form of a spatial body force distribution obtained and implemented in CFX as a source term.

Several hypotheses are used to simplify the simulations while attempting to capture the main physics of the flow. The first is to neglect the effect on capturing the stall point of blade-to-blade interactions from adjacent blade rows and of *rotating instabilities*. Rotating instabilities are circumferential perturbations of multiple blade pitch in wavelength, referred that can occur in the stable operating region near stall. This hypothesis allows for the use to simulate only a single

blade passage per blade row with a mixing plane interface between two adjacent blade rows which only a radial distributions of circumferentially averaged properties are transferred. This practice is standard for simulating multi-stage compressors where blade rows have different blade numbers which would otherwise require prohibitively expensive (in time and resources) full-annulus simulations. The second hypothesis, the plasma actuator operation is quasi-steady from the point of view of the flow. In this case, the flow convection time is about one order of magnitude higher than the period of the plasma actuator input, which means that this assumption may still be all right and thus allow for the use of a constant (time-averaged) body force distribution to represent the effect of the plasma actuator.

Computational Domain and Boundary Conditions

Although the first test configuration aims to assess the casing plasma actuation concept on the axial compressor stage, the compressor rig must be run with the centrifugal compressor as well. The simulation domain thus includes both stages as shown in figure 3.6 (although some simulations that included only the axial rotor were also carried out for comparison, as shown in appendix D). The domain is subdivided into seven subdomains containing, in order, the intake, plasma actuator, rotor, stator and inter stage duct, impeller, diffuser and end duct. The first subdomain is an axial length approximately equal to that of the Bellmouth without directly modeling the latter. The last subdomain models the plenum without meshing the real plenum. The inset in figure 3.6 illustrates the extent of this subdomain inside the physical plenum. (A validation of this approach versus meshing and simulating the real plenum is presented in appendix E). Each subdomain is one-blade pitch in circumferential width, with the inlet and plasma domains taking the width of the rotor domain and the diffuser and end duct domains that of the impeller.

With reference to figure 3.6, the *Rotor Inlet*, *Stator*, *Diffuser* and *End_Duct* subdomains are stationary while the *Rotor* and *Impeller* domain are solved in the rotating frame. The *Plasma* subdomain starts at the axial location where the stationary bullet of the intake ends and the hub stars to rotate as part of the axial rotor. It ends just upstream of the rotor leading edge so as to place the spatial force distribution representing the plasma actuator as closed to the rotor leading edge as possible to represent the physical configuration. The closeness of this interface to the rotor leading edge requires the use of a Frozen Rotor interface (instead of a Stage, i.e. mixing

plane interface) which allows for transfer of pitchwise flow variation across the interface between the Rotor and Plasma subdomains. The remaining interfaces are of the Stage type which is much less computationally demanding than the Frozen Rotor interface.

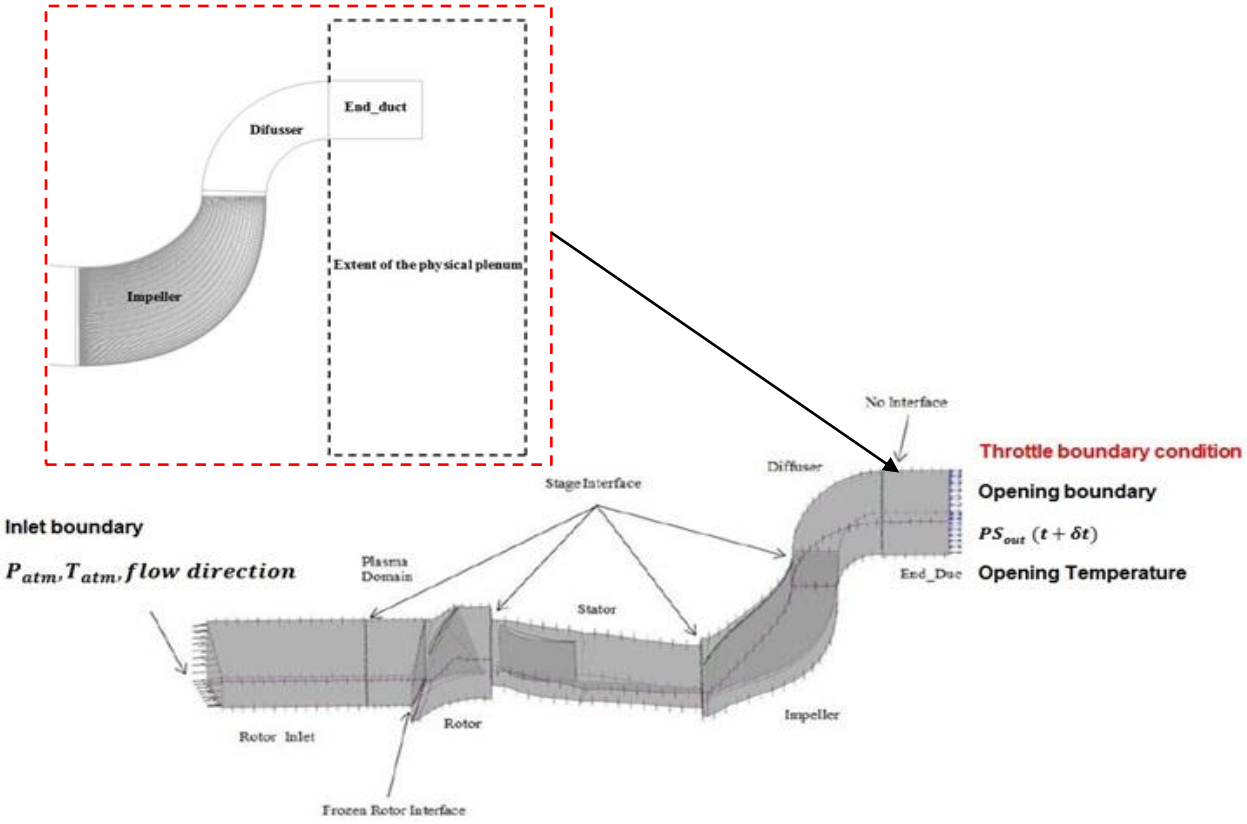

Figure 3.6: Schematic of the two-stage compressor computational domain for plasma actuation on axial rotor

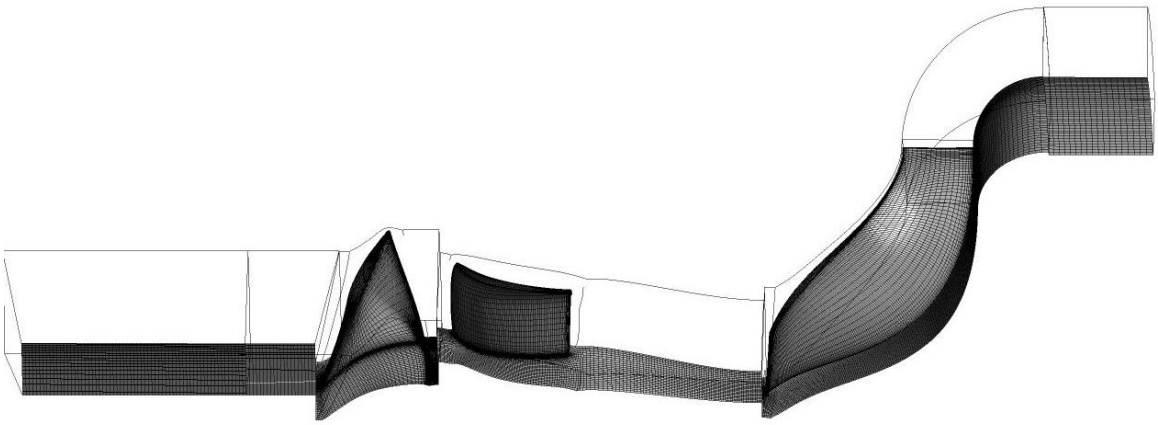

Figure 3.7: Mesh of two-stage compressor computational domain

The subdomains containing the blade rows and the diffuser were meshed using ANSYS TURBOGRID, a meshing software specialized for turbomachinery. The mesh for the remaining sub domains were created with GAMBIT but the number of elements in the radial, axial and circumferential directions were chosen to be coherent with the TURBOGRID subdomains to preserve mesh density compatibility at the interfaces. Following a mesh study whose details are given in Appendix H, the final chosen mesh is shown in figure 3.7 and contains 1091440 nodes. The node distribution (meriodional×pitch×radial) for the rotor, stator and impeller subdomains are 78×70×40 , 110×40×36 and 110×50×30, respectively, with the corresponding number of radial nodes in the tip/hub clearance being 8, 7 and 7. The y+ value at the solid surfaces vary between approximately 12 and 20.

All solid surfaces are modeled as a no-slip wall with the automatic wall function option used to switch between a no-slip wall and wall function according to the local y+ value. The only exceptions are the hub and shroud surfaces of the *End_Duct* subdomain which are defined as free-slip (inviscid) walls to account for the fact that this domain lies in the plenum with no physical solid surfaces at the position of these endwalls (see inset of figure 3.6). In the rotating sub-domains, stationary endwall surface such as the casing are defined as counter rotating. The *Stator* subdomain hub is defined as rotating to be consistent with the physical configuration. Last but not least, the SST turbulence model is chosen. The common k-ε model is more robust and may be more suitable for highly separated flow such as in stall and surge simulations. However, the SST model is more accurate in predicting the onset and amount of boundary layer separation in an adverse pressure gradient and in modeling flow over curved surfaces [45]. Since simulations in the current cover the stable range of the speedline up to the stall point, the accuracy of the SST model is more useful than the robustness of the k-ε model.

For the configuration where the centrifugal compressor stage is tested alone, the computational domain and boundary conditions are very similar to those of the two-stage configuration in figure 3.6. As shown in figure 3.8, the only difference is that the *Plasma-Rotor-Stator* subdomains combination in figure 3.6 has been replaced by an empty *Intermediate* sub domain followed by a *Plasma* subdomain, the latter sharing a Frozen Rotor interface with the *Impeller* domain.

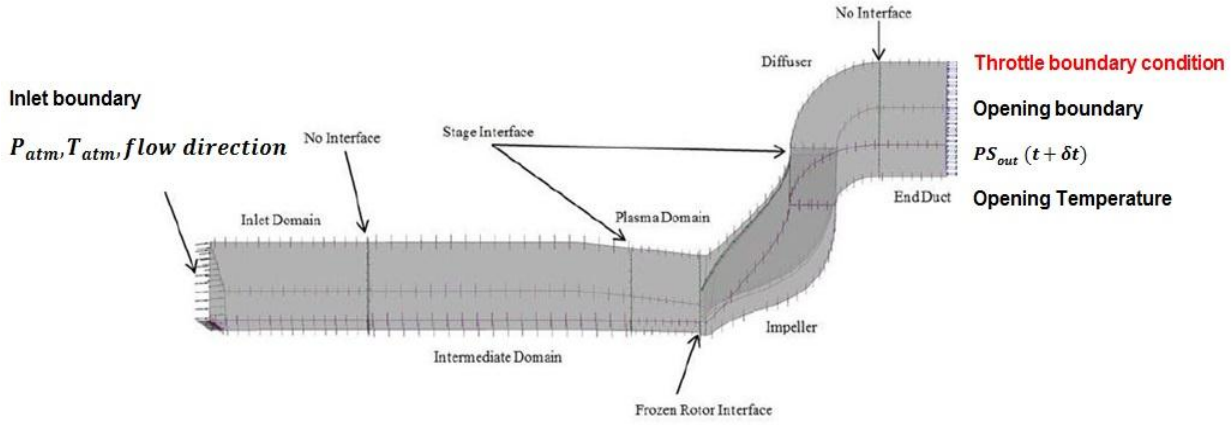

Figure 3.8: Schematic of computational domain for centrifugal compressor alone for plasma actuation on impeller

Plasma Actuator Model

The plasma actuator model consists a time-invariant spatial body force distribution obtained from the model by Lemire and Vo [23] as shown in figure 2.14 implemented in CFX as a momentum source term through a CEL function. The original 2-D spatial body force distribution for a fine Cartesian used by Lemire and Vo to run their model is mapped onto the 3-D mesh of the *Plasma* subdomain at the location where the physical plasma actuator is placed and then multipled by a scale factor to give an integrated axial value equal to the desired actuator strength. The curvature effect of the cylindrical domain was taken into account in the mapping by considering the effective depth of each cell. The mapping procedure is the same as that described by Vo [13] and is described in more detail in appendix F. While the plasma actuator in experiments is installed 5 mm upstream of the rotor/impeller leading edge, it had to be placed at 6 mm upstream of the rotor/impeller leading edge in the CFD simulations to avoid mesh generation problems associated with placing the interface between the plasma and rotor/impeller sub-domains too close to the rotor/impeller leading edge.

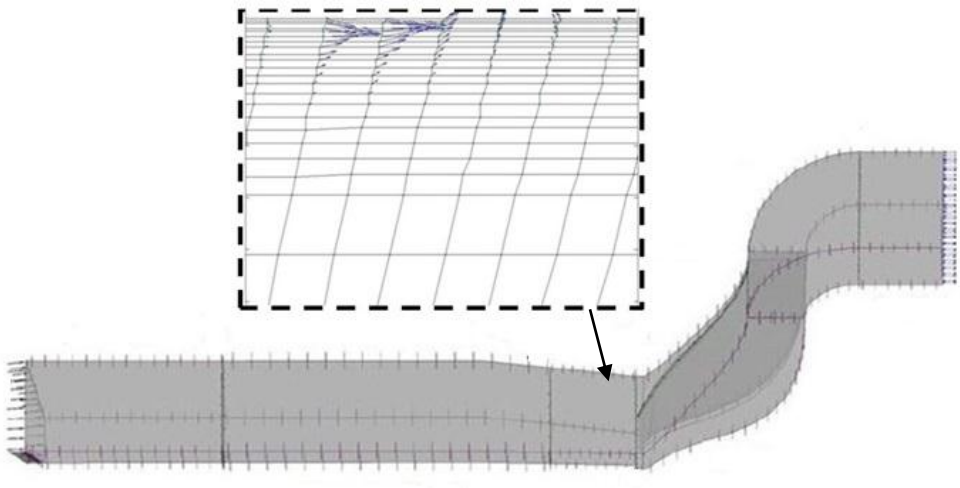

Figure 3.9: Plasma body force mapping for the plasma domain

3.3 Simulation Procedure

For each of the two test configurations, the numerical investigation aims to predict the stall point without and with plasma actuation, which requires in each case simulating stable operating up the speedline until the stall point is reached. The simulation procedure consist of first obtaining a stable operating point via a steady simulation using a standard exit static pressure boundary condition and calculating the value of the throttle constant (K_t) corresponding to this point via equation (C.10) in Appendix C. Using the converged solution from this point as initial condition, the simulation switched to the time-accurate mode with the throttle boundary condition and the value of K_t is increased to obtain the next stable operating point up the speedline. This process is repeated each time using the previous solution as the initial condition and increasing K_t until the last stable point (stall point) is reached. In principle, if the stalling behavior is abrupt, this numerical setup should show the pressure rise coefficient and mass flow drop if K_t is increased beyond the value corresponding to the last stable point. However, the criterion applied in the current study is that the interface between the incoming and tip clearance flow at the rotor or impeller blade tip reaches the leading edge plane.

3.4 Experimental procedure

The experimental procedures parallels the numerical procedure laid out in section 3.3 with a slight modification to avoid damaging the DBD plasma actuator. While the part of the

actuator inside the compressor gas path is relatively thin, its protrusion is enough to change the tip clearance and thus performance. To ensure a fair comparison between results without and with plasma cases, the no-actuation case is run with the actuator in place but turned off.

The procedure consists of starting the compressor and waiting for it to stabilize at 4400 rpm with the throttle opened for a stable operating point. The throttle is then closed in steps. At each new throttle position, a pause of three to five second is provided for the flow to stabilize before the pressure, temperature and rpm data is recorded (mass flow rate, pressures and temperatures are monitored in real time so as to determine whether the flow has settled.) When the plasma actuator is off, ten one-second averaged readings are taken for pressures and temperature at each throttle position. The points are numerically averaged to get the final value and the scatter is used to determine the error margin. With the plasma actuator turned on, a one-second average is taken for each point to avoid the risk of actuator damage from extended operation. This reading is assumed to be the averaged point. The error margin is assumed to be the same as a similar point (in terms of mass flow) without plasma. For the speedline measurements, the rake is taken out to minimize flow interference and the static pressure at the shroud along with the inlet total (ambient) pressure to obtain the total to static pressure rise.

For the two-stage configuration, rotating stall was accompanied by a sudden drop in pressure rise and mass flow so that the previous point in the slow throttle closing is taken as the last stable point (stall point). This technique was also verified and confirmed later with the string technique. For the second test configuration with the centrifugal compressor stage operating alone, only the string technique was used to determine the stall point because the pressure and mass flow change at rotating stall is not obvious. In the test with plasma actuation, the DBD actuator is only turned on near the no-plasma stall point and left on until the new stall point is reached. The speedline with and without plasma were carried out two to three times in succession to insure repeatability of the results.

Finally, for measurement of the total pressure profile just downstream of the rotor and the impeller, the Kiel probes is traversed from the shroud toward the hub. At each position, a two to three second pause is given for the flow to settle and pressure data is recorded at ten one-second reading. The average is taken and the scatter provides the error margin.

CHAPTER 4 RESULTS AND DISCUSSION

This chapter presents the results for the two tested configurations at 4400 rpm, namely the two-stage configuration with plasma actuation at the axial rotor leading edge and the single-stage centrifugal compressor configuration with plasma actuation at the impeller leading edge. For each configuration, the computational predictions from CFD simulations are first presented and then compared with experimental results with a discussion on the comparison. Unless otherwise specified, the numerical simulations used as inlet conditions the ambient conditions recorded during the experiments and the pressure and temperature in the calculations of points on the speedline are taken from the CFD flow solution at the same axial and radial locations as the corresponding probes in the test compressor. In the plots, the suffixes *p* and *e* in the point numbering refers, respectively, to plasma actuation and experimental data. While this chapter presents one set of experimental data per tested configuration, each case was tested two to three times to ensure repeatability. The data for the repeated tests are presented in Appendix I.

4.1 Two-Stage Configuration with Plasma Actuation on Axial Rotor

Figure 4.1a presents the results for the two-stage CFD simulations in terms of the stagnation-to-static pressure ratio versus corrected mass flow for the entire two-stage compressor (figure 4.1a) without and with plasma actuation at the axial rotor with an actuator strength of 100 mN/m, with key points identified. (It is noted that the static pressure at the diffuser exit is an area-averaged over a plane in the virtual *End_duct* subdomain of figure 3.6 at the location of the static pressure taps in the plenum which is not reproduced in the simulation.) Figure 4.1b presents the corresponding stagnation-to-static pressure rise coefficient taken across the axial rotor versus corrected mass flow, along with the entropy contours at the rotor blade tip plane at the key points to determine the position of the incoming/tip clearance flow interface as a stall assessment criterion. The ‘ghost points’ with dashed outline represents the points that have supposedly stalled according to this criterion. The errors bars on some of the points higher up the speedline represents the range of the oscillation in pressure rise seen in the solution with the corresponding point being the average value of the pressure rise. The procedure to obtain the error bars and average for these points is explained in Appendix I.

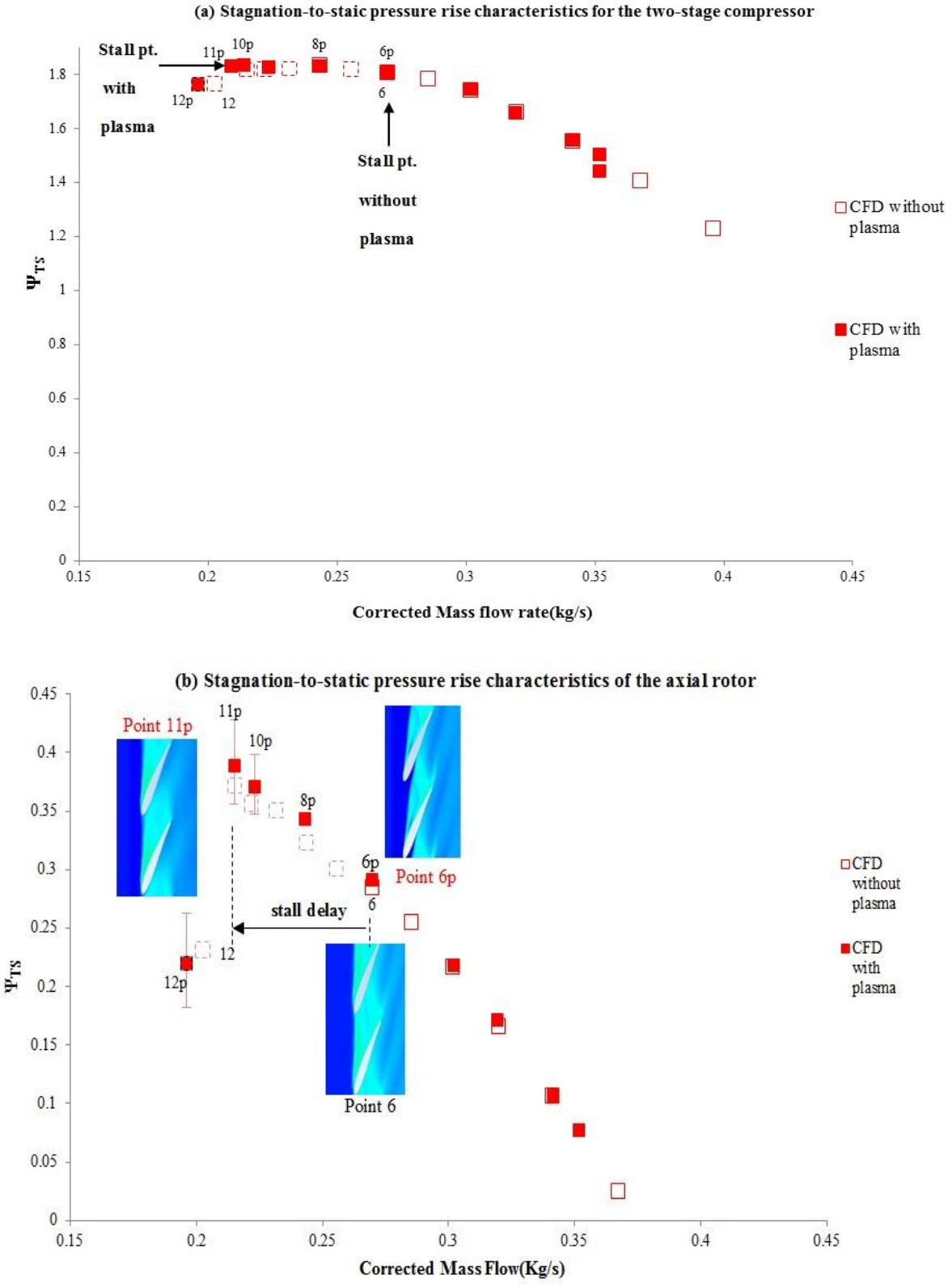

Figure 4.1: CFD assessment of effect of plasma actuation at axial rotor leading edge

From the results presented in figure 4.1, point 6 is the stall point for the no-actuation case according to the spike stall inception criterion since the corresponding entropy contour in figure 4.1b shows that the incoming/tip clearance interface reaches the rotor tip interface leading edge plane. According to the literature, the negative slope of the speedline of the two-stage compressor at point 6 in figure 4.1a further supports the inference of spike stall inception originating in the axial rotor since the zero-slope peak of the speedline (modal stall inception criterion) has not yet been reached. Using this spike stall inception criterion, one can see that the additional axial momentum added by the plasma actuator at the rotor leading edge pushes the incoming/tip clearance flow interface downstream inside the blade passage from the entropy contours for point 6p in figure 4.1b. The stall point with plasma actuation is thus delayed until point 11p giving a reduction in stall mass flow of 20.27 %. The plasma actuation also slightly increases the pressure rise. These observations agree with those of Vo [13, 14, 24] for this actuation concept.

The only puzzling observation is that in the no-actuation case, the ghost points indicate that both the axial rotor and two-stage total-to-static pressure rise continue to increase beyond point 6 even though we would expect it to drop once the stall criterion is reached. One initial hypothesis is that presence of a centrifugal stage which is more robust to rotating stall may have stabilized the two-stage compressor and contributed to this unexpected behavior. However, a simulation of the rotor alone in Appendix D shows the same observation and thus discounts the presence of the centrifugal stage as a being factor. Experimental data should provide some confirmation of this behavior.

Figure 4.2 plots the experimental results along with the computational predictions of figure 4.1 in the background. For the test data, the errors bars were determined using the procedure outlined in section 3.4. The ghost points (10e and 12ep) with dashed outline represents the points *in rotating stall*, the dashed error-bars for these points represent the extent of flow oscillations due to rotating stall. In going from 9e to 10e and from 11ep to 12ep through a small closing of the throttle, not only the pressure rise and mass flow suddenly drop but the oscillations as outlined by the error bars also suddenly increase. Thus, the measured stall points (last stable points) are point 9e for the no-actuation case and 11ep for the actuated case, giving a measured reduction stall mass flow of 19.28%, which is relatively close the predicted value from CFD, and

also compares well with micro-injection techniques reviewed in Chapter 2. This delay in stall was also repeated in subsequent experiments as shown in Appendix I.

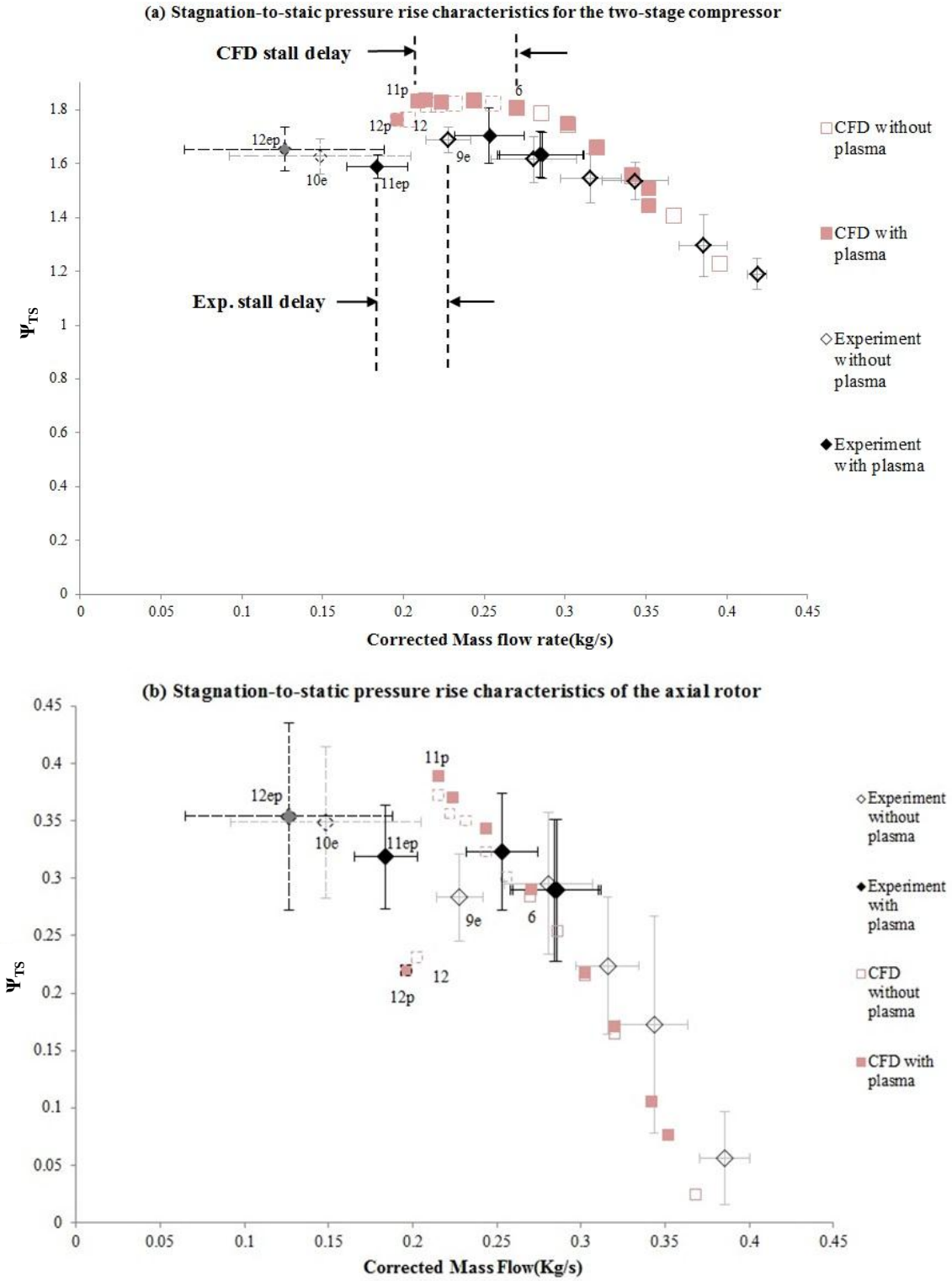

Figure 4.2: Experimental vs. CFD assessment of plasma actuation at axial rotor leading edge

Another observation from figure 4.2 is that there is a modest but noticeable difference between the measurements and simulations in both the stall points (points 9e vs. 6 and 11ep vs. 11p) and the speedline (in stable range to the right of the stall point). In particular, one notices that the simulations under-predict the pressure rise for the axial rotor but over predicts it for the full two-stage. One possible explanation is that the exact blade shape at 4400 rpm may not have been reproduced in the simulations. Under rotation, the blades from the rotor and impeller tend to un-twist and this deformation was taken into account such that the rotor and impeller production blade geometry ('cold shape') were slightly different from the desired rotating geometry at the original design speed of 7200 rpm. However, the rotor and impeller were simulated with the originally designed blade geometry at 7200 rpm rather than correcting the rotating shape to 4400 rpm. At 4400 rpm, the rotor would have lower stagger angle (more pressure rise) and impeller would have more backsweep (less pressure rise) than the simulated geometries at 7200 rpm. Since the centrifugal stage produce much more pressure rise than the axial stage, the trend seen in the impeller would be the same as seen in the two-stage compressor. This would explain the tendency observed in the speedline data comparison. Furthermore, this hypothesis is further reinforced by a comparison of the spanwise distribution of pitch-averaged total pressure just downstream of the axial rotor at an operating corrected mass flow of 0.30 kg/s in figure 4.3. This comparison shows a higher rise in total pressure ratio in the upper half-span for the tested versus simulated geometry and the difference rises with span. This is consistent with the actual rotor blade having increasing lower stagger angle than the simulated rotor as one moves toward the tip, as the deformation naturally increases with rotor span. The extent of this factor for the structurally sturdier impeller will be verified in section 4.2. Other factors that may play a role in the discrepancy between the numerical and experimental speedlines and stall points include: the estimated value and axisymmetric assumption of the simulated tip clearance (the real tip clearance was not perfectly axisymmetric and an average value minus an estimate of blade radial deformation were used to get the simulated tip clearance); the accuracy of the simulated endwall boundary layer at the rotor inlet (the actual Bellmouth intake was not simulated); the fully annular assumption for the simulated plasma actuator; and the borderline validity of the steady spatial body force distribution at the flow speeds involved. Note that instrument accuracy only represents about 10 % of the pressure rise error-bars for the stall (last stable) points. The rest of the error-bars come from the flow field fluctuations resulting from flow features such as

those due to relative motion between adjacent blade rows and tip clearance flow oscillations near stall.

Another observation is that, notwithstanding the error bars, figure 4.2b shows that the stagnation-to-static pressure rise across the axial rotor continues to increase after stall (points 9e to 10e). This is consistent with the puzzling observation seen in figure 4.1b in the simulations at the left of the predicted stall point (point 6).

A last interesting note is the visual observation during the experiments that at stable operating points near stall the string starts to oscillate but still curving downstream. This is consistent with the flow pressure oscillation seen at points near stall in the simulations (e.g. points 10p and 11p in figure 4.1).

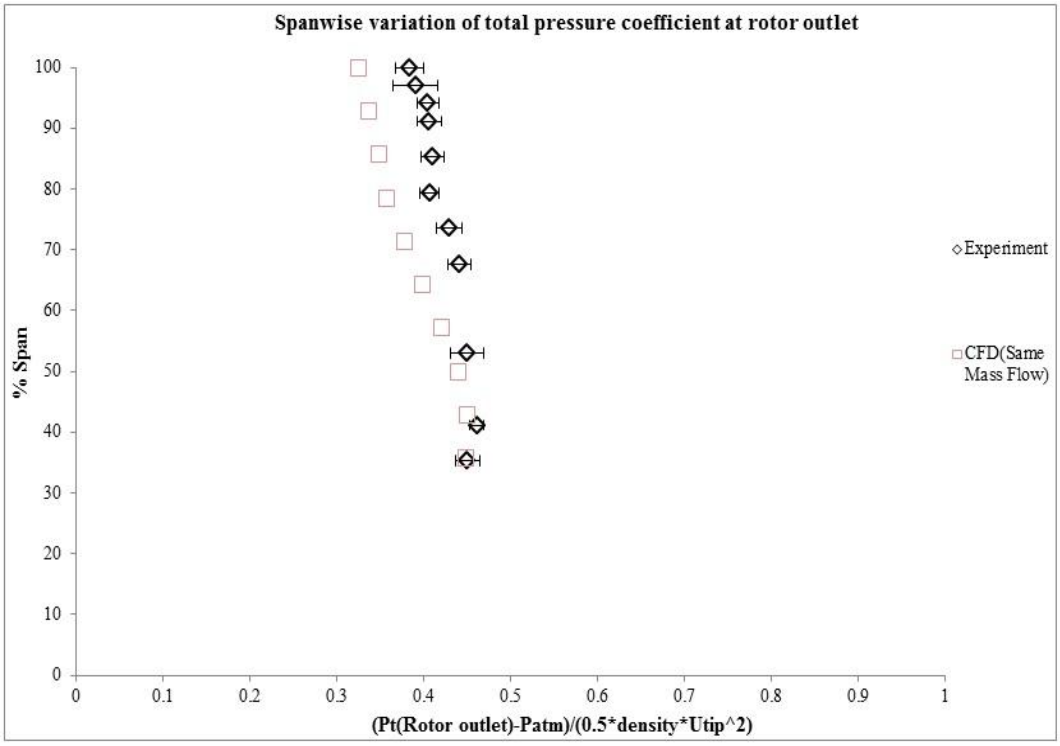

Figure 4.3: Spanwise variation of pitch-averaged total pressure coefficient at rotor outlet

4.2 Single-Stage Centrifugal Compressor Configuration with Plasma Actuation on Impeller

As discussed in chapter 2, rotating stall in centrifugal compressor can occur in either impeller or diffuser and is more varied and much less understood than in axial compressors. The CFD simulations of the centrifugal compressor stage without plasma actuation are first carefully studied to get a better idea of the source of rotating stall. This assessment is important as the physical constraints in the compressor rig only allows for the application of plasma actuator at the impeller leading edge to address stall inception in the impeller.

Figure 4.4 shows the simulated speedline with the entropy contours at the impeller tip plane for selected points. One can observe that the incoming/tip clearance flow interface reaches the leading edge at point 24. When the numerical throttle is closed slightly further, the pressure and mass flow drops to point 26 while the interface moves upstream of the leading edge as is usually expected for an axial rotor. From these observations, it is inferred that point 24 is the stall point (last stable point) with the ghost point 26 with dashed outline being in rotating stall, and that for this centrifugal compressor the impeller is the source of the rotating stall with a stall criteria similar to spike stall inception.

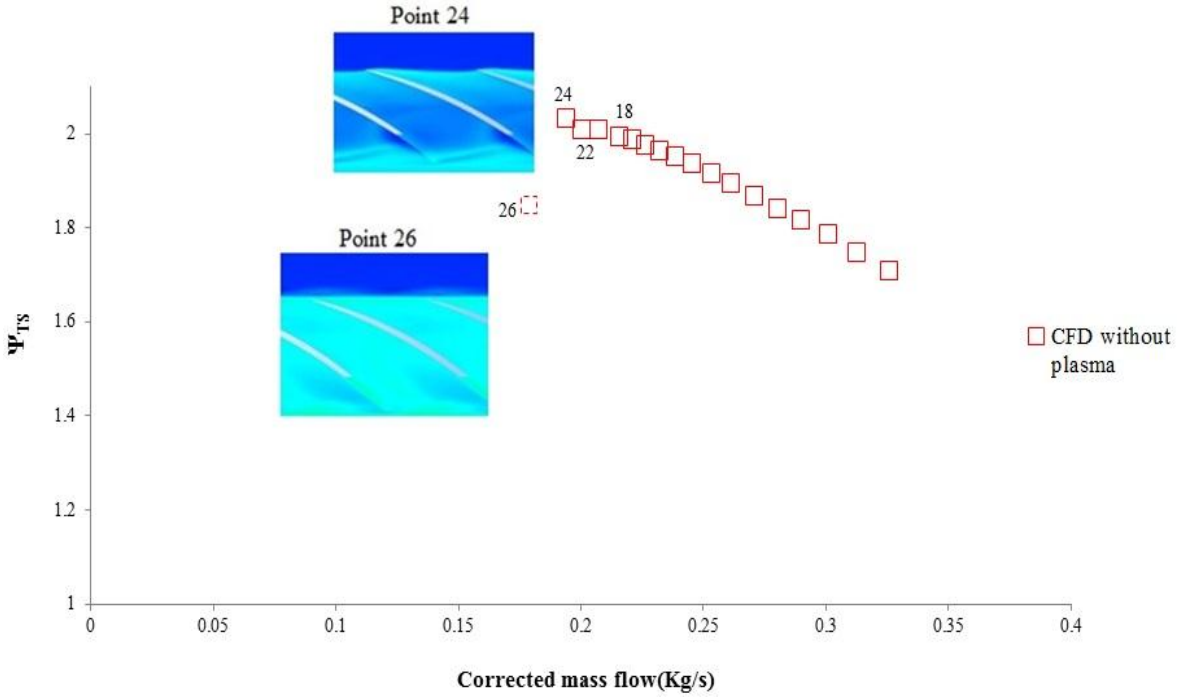

Figure 4.4: CFD prediction of centrifugal compressor total-to-stagnation characteristics (speedline) at 4400 RPM without plasma actuation

The inference that the impeller is the source of rotating stall for this centrifugal compressor is further reinforced by the evolution of the flow field. Figure 4.5 shows the streamlines in a meridional plane through the impeller and vaneless diffuser for points 18, 22 and 24 identified in figure 4.4. While there is a large flow recirculation zone in the diffuser at point 18 that could be associated with a diffuser stall, the size of the recirculation significantly decreases as one moves up the speedline toward point 24. The proposed explanation for this behavior is illustrated in figure 4.6, which shows that as the meridional velocity diminishes with reduced mass flow, the swirl angle of the flow exiting impeller (absolute flow angle α) increases. The result is a longer path traveled by flow particle along the vaneless diffuser and hence a lower pressure gradient and separation (or recirculation) near diffuser shroud. The reduction in the recirculation zone implies that the diffuser is not the source of stall for this centrifugal compressor and thus that plasma actuation on the impeller may work in delaying stall. (In fact, as shown in Appendix G, an early computational study was carried out with different plasma actuation location on this centrifugal compressor stage at 3700 rpm to show that the impeller leading edge actuation was the best configuration)

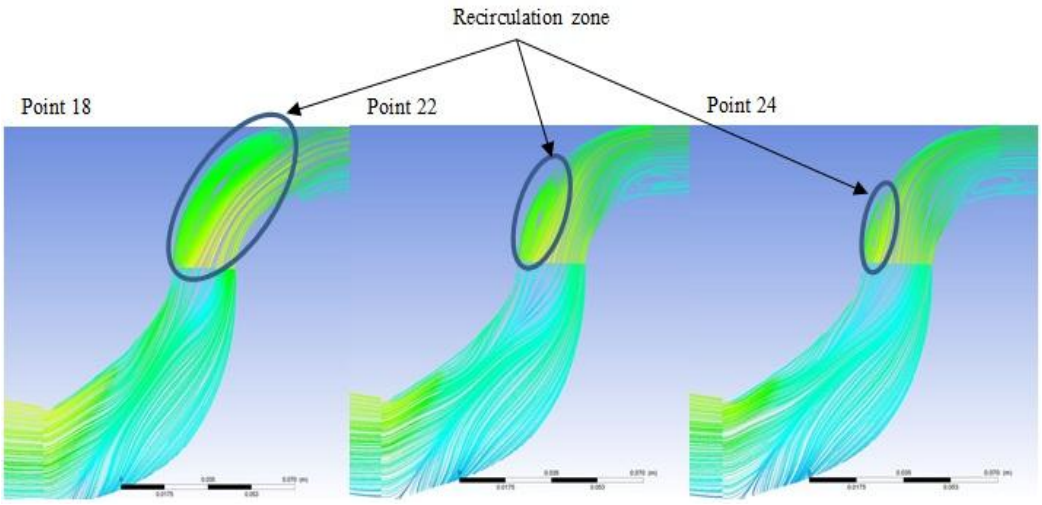

Figure 4.5: Variation in recirculation zone size near diffuser shroud for points in figure 4.4

Figure 4.7 presents the speedline with plasma actuation at 100 mN/m from CFD simulations on top of the no-actuation speedline of figure 4.4. The entropy contours at the impeller blade tip for points 24p versus point 24 shows that the casing plasma actuation at the impeller leading edge pushes the incoming/tip clearance flow interface inside the blade passage as was the case with the axial rotor. Using the position of this interface as the stall criterion, the

new stall point would be point 32p, giving a reduction in stall mass flow of 16.67% for the proposed plasma actuation concept.

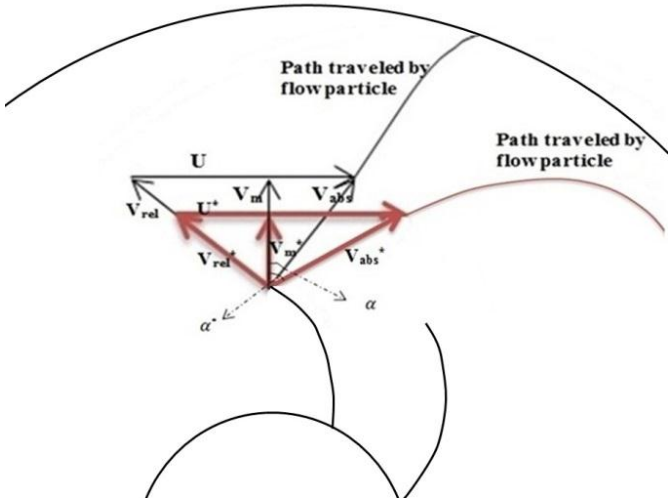

Figure 4.6: Explanation for evolution of recirculation zone near vaneless diffuser shroud

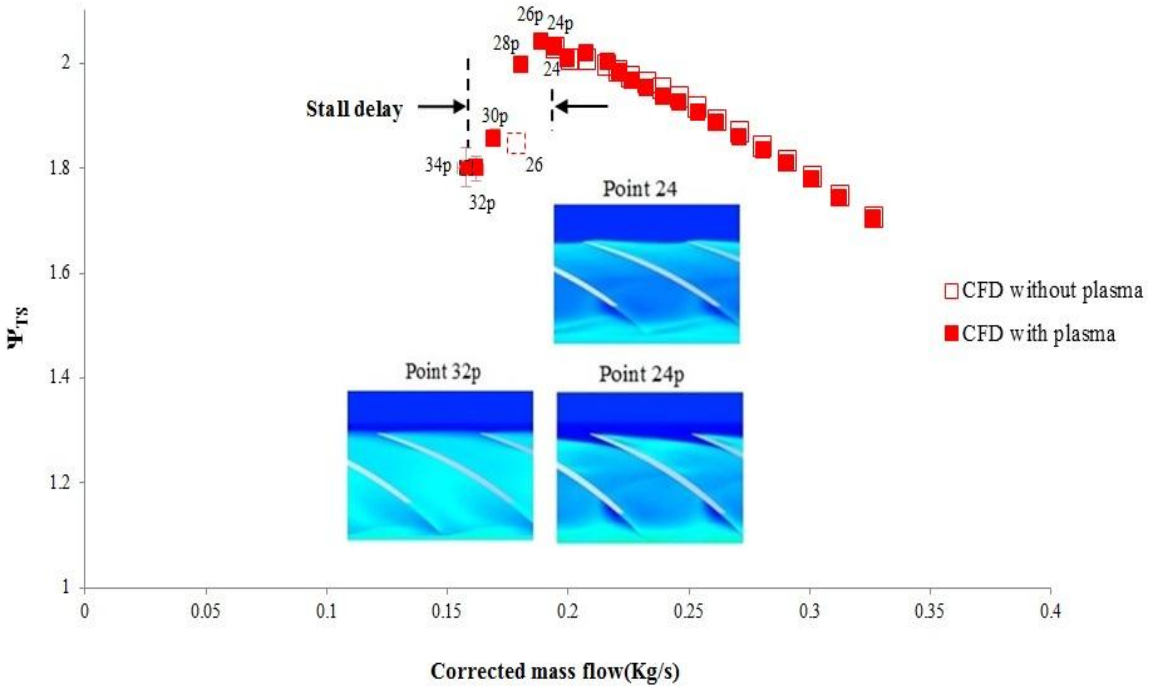

Figure 4.7: CFD prediction of centrifugal compressor total-to-stagnation characteristics with versus without plasma actuation

Figure 4.8 presents the experimental data for the centrifugal compressor with the corresponding CFD results from figure 4.7 in the background. Based on the string technique, the measured last stable point (stall point) without and with plasma are points 12e and 9ep, respectively, which translate to a stall mass flow reduction of 28.39%, which is close to the CFD prediction in terms of absolute reduction and in line with what had been achieved in the literature [reference] with micro-tip injection on impellers. With the repeatability of this extension in a repeat of these tests (Appendix I), this experiment shows that the proposed casing plasma actuation concept can also work for a centrifugal compressor in which then impeller is the source of rotating stall. An additional important observation is that the measured stall mass flow of the centrifugal stage without actuation (point 12e in figure 4.8) is much lower than that of the two-stage configuration (point 9e in figure 4.2). This confirms that the axial stage is the source of rotating stall inception in the axial-centrifugal configuration and thus validates the previous two-stage setup for testing plasma actuation on the axial rotor.

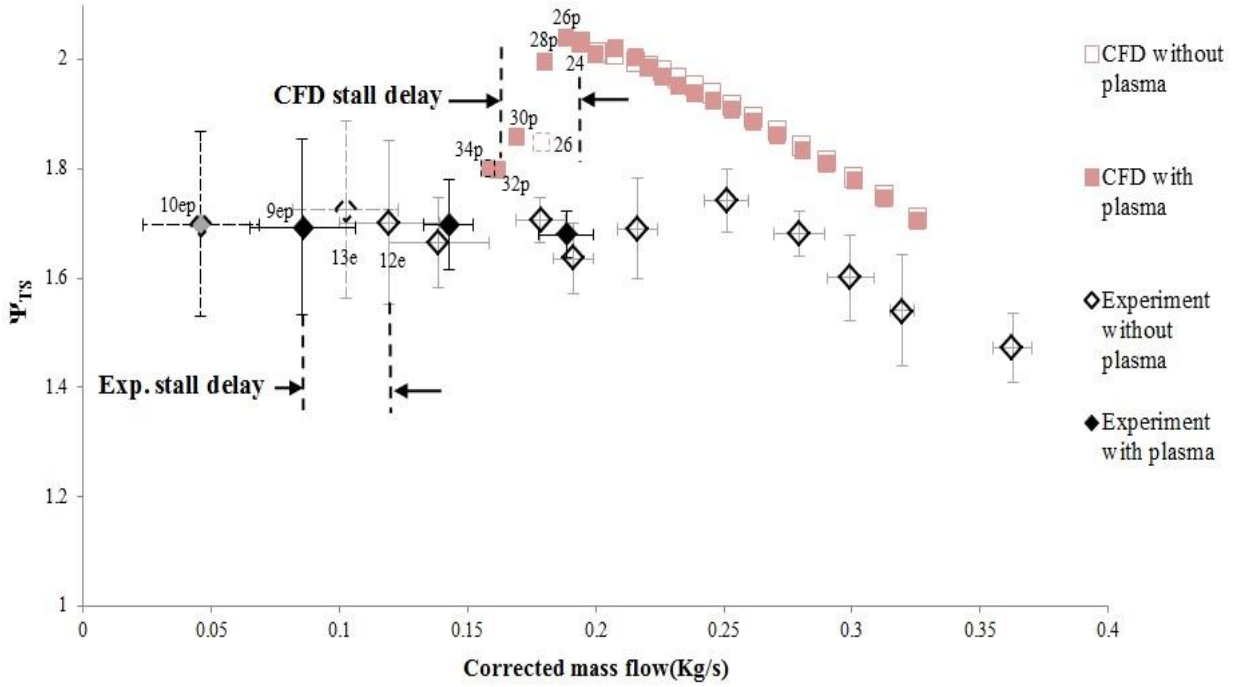

Figure 4.8: Measured versus CFD prediction of centrifugal compressor total-to-stagnation characteristics without and with plasma actuation

The comparison of the experimental and CFD results in figure 4.8 also shows some discrepancy in the prediction of the speedline by CFD. One difference is that slope of the speedline near stall is very flat in the experiments compared the predicted negative slope for no actuation and positive slope with plasma actuation. The differences concerning the shift in the predicted stall point and lower pressure rise in the experiment versus the CFD simulations are consistent with the observations in the two-stage configuration. A comparison of the measured and predicted (CFD) spanwise stagnation pressure at the impeller exit and diffuser exit at the design corrected mass flow of 0.30 kg/s without plasma in figures 4.9 and 4.10 may provide some clues to explain this discrepancy. Figure 4.9 indicates that the CFD simulations predict the pressure rise across the impeller quite well with proportionately much less discrepancy than for the axial rotor (figure 4.3). However, figure 4.10 point to a growing discrepancy in the stagnation pressure distribution at the diffuser exit as one moves toward the span. The results in figures 4.9 and 4.9 indicate the blade deformation discrepancy argument for the axial rotor is not a factor for the impeller and that the discrepancy seen in the experimental versus CFD speedlines is due to the CFD code’s difficulty in accurately capturing the total pressure loss in the hub region of the vaneless diffuser.

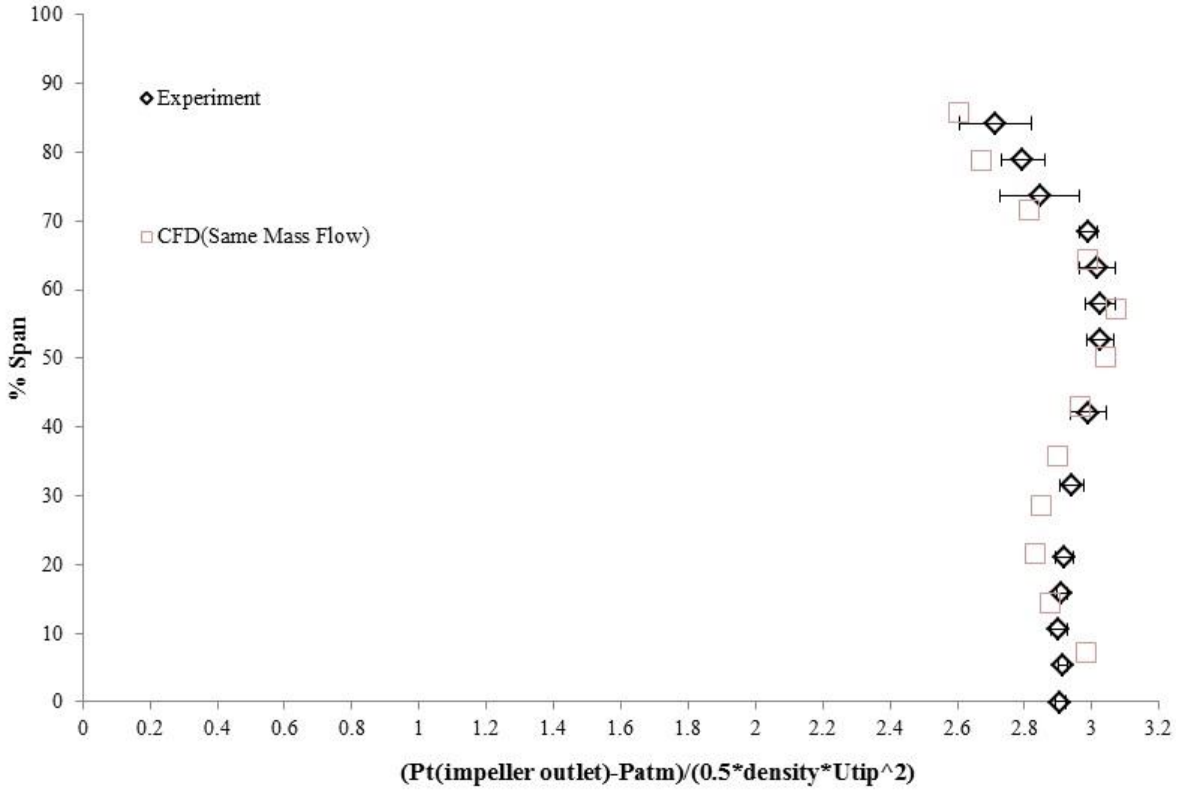

Figure 4.9: Spanwise variation of pitch-averaged total pressure coefficient at impeller exit

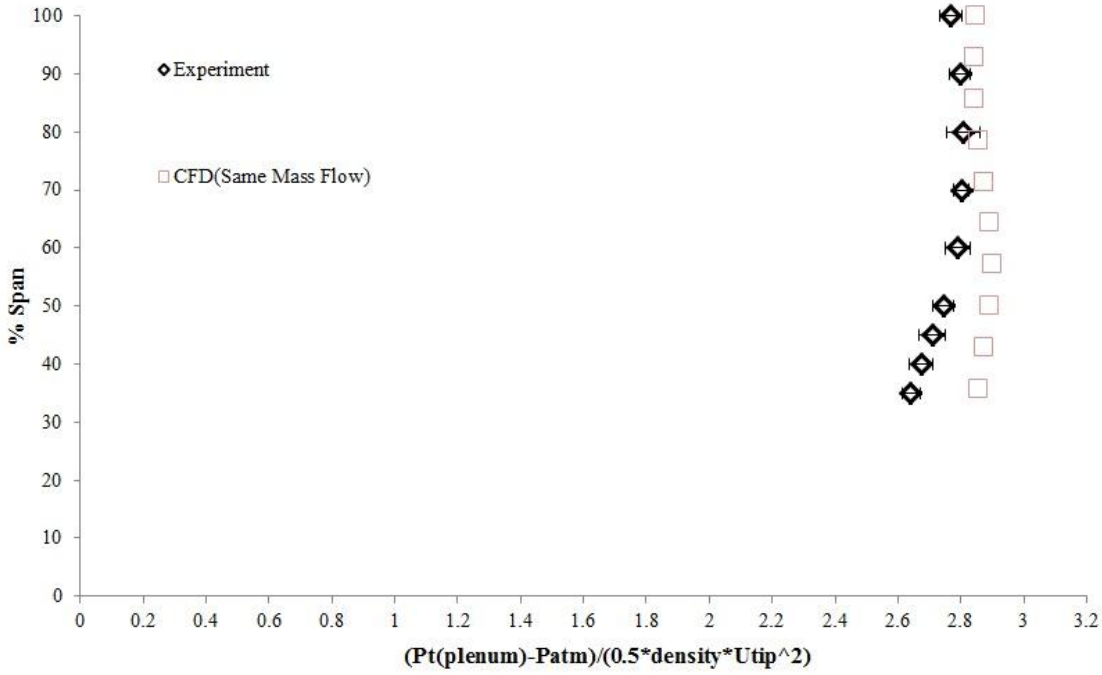

Figure 4.10: Spanwise variation of pitch-averaged total pressure coefficient at diffuser exi

CHAPTER 5 CONCLUSIONS

5.1 Summary and conclusions

A concept of annular casing plasma actuation to suppress rotating stall inception has previously been proposed but only evaluated numerically for an isolated compressor rotor using a basic CFD code. This project aimed to assess this concept both numerically and experimentally on an axial compressor stage as well as a centrifugal compressor, which are part of a two-stage axial compressor test rig operating at 4400 rpm. The latest engineering DBD plasma model and dynamic throttle boundary condition are implemented in a sophisticated commercial RANS CFD code (ANSYS CFX) to form the computational tool. The computational domains were set up to model closely the tested configurations consisted of multiple blade rows of single blade passage simulations with mixing plane interfaces between the blade rows.

Two configurations were simulated and tested. The first is the entire two-stage axial-centrifugal compressor with a 100mN/m annular casing plasma actuator placed just upstream of the axial rotor leading edge. The second configuration incorporates only the centrifugal compressor with the same casing plasma actuator placed just upstream of the impeller leading edge.

Both experiments and simulations show that the casing plasma actuator can work for both the axial compressor and the centrifugal compressor in which the impeller is the source of rotating stall. The CFD simulations seem to confirm that the mechanism of suppression of stall by the casing plasma actuator is that the axial momentum added by the actuator pushes the incoming/tip clearance flow interface downstream into the blade passage. This mechanism not only applies for the axial rotor but to the impeller as well. The predicted percentage reduction in stalling mass flow matches the experimental value reasonably well in both configurations. However, the CFD simulations over-predicts the mass flow of the stall point as well as the pressure rise of the centrifugal stage and under-predict the pressure rise of the axial stage. Comparison of the spanwise distribution of total pressure just downstream of the axial rotor,

impeller and vaneless diffuser at the design mass flow indicates that the main factors for the difference are the failure to fully correct for axial rotor blade deformation at the (part) speed of 4400 rpm and the inability to accurately capture the total pressure loss in the hub region of the vaneless diffuser.

In addition, the axial compressor rotor seems to exhibit a peculiar and yet to be explained behaviour of continued increased in exit tip static pressure past the point of stall, apparent in both CFD and experimental data.

5.2 Recommendations for Future Work

Experimental validation of the simulation results indicate that the computational tool based on ANSYS-CFX could possibly serve as a means to investigate the plasma actuation concepts for rotating stall suppression at more realistic speeds that are beyond the capability of existing plasma actuators. However, a number of tasks are recommended to improve this tool and make it more accurate.

1) Verify and correct any discrepancy between the simulated blade geometry and true geometry at 4400 rpm
2) A more detailed experimental survey of the flow field in the compressor rig (without plasma actuator) at more points on the speedline to validate in detail the CFD simulations an identify the weakness of the computational tool. A more detail flow survey could include using total pressure traverse at all available meridional positions, including upstream just of the rotor and impeller, and obtaining two-dimensional total pressure distribution at the stator exit plane and apply flow visualization techniques in the vaneless diffuser.
3) Second, a time-varying spatial body force distribution should be implemented for the DBD actuator model as the quasi-steady assumption for the plasma effect is reaching its limit even for this low-speed compressor.

Finally, an investigation both with detailed measurement and CFD simulations into the source of the rise in static pressure at the exit of the axial rotor after stall.

REFERENCES

[1] I. J. Day, "Axial Compressor Stall," University of Cambridge, 1976.

[2] J. D. Paduano, E. Greitzer, and A. Epstein, "Compression system stability and active control," *Annual Review of Fluid Mechanics*, vol. 33, pp. 491-517, 2001.

[3] F. Moore, "A theory of rotating stall of multistage axial compressors: part I—small disturbances," *Journal of Engineering for Gas Turbines and Power*, vol. 106, pp. 313-320, 1984.

[4] P. D. Silkowski, "Measurements of rotor stalling in a matched and a mismatched multistage compressor," *GTL report*, vol. 221, 1995.

[5] T. Camp and I. Day, "1997 Best Paper Award—Turbomachinery Committee: A Study of Spike and Modal Stall Phenomena in a Low-Speed Axial Compressor," *Journal of Turbomachinery*, vol. 120, pp. 393-401, 1998.

[6] I. Day, "Stall inception in axial flow compressors," *Journal of Turbomachinery*, vol. 115, pp. 1-9, 1993.

[7] H. FUJITA, "A study on configurations of casing treatment for axial flow compressors," *Bulletin of the JSME*, vol. 27, pp. 1675-1681, 1984.

[8] J. M. Haynes, G. J. Hendricks, and A. H. Epstein, "Active stabilization of rotating stall in a three-stage axial compressor," *Journal of Turbomachinery*, vol. 116, pp. 226-239, 1994.

[9] H. D. Vo and J. D. Paduano, "Experimental development of a jet injection model for rotating stall control," in *ASME, International Gas Turbine & Aeroengine Congress & Exhibition, 43 rd, Stockholm, Sweden*, 1998.

[10] H. J. Weigl, J. Paduano, L. Frechette, A. Epstein, E. Greitzer, M. Bright, *et al.*, "Active stabilization of rotating stall and surge in a transonic single stage axial compressor," Massachusetts Institute of Technology, Dept. of Aeronautics and Astronautics, 1997.

[11] C. Nie, G. Xu, X. Cheng, and J. Chen, "Micro air injection and its unsteady response in a low-speed axial compressor," in *ASME Turbo Expo 2002: Power for Land, Sea, and Air*, 2002, pp. 343-352.

[12] A. Deppe, H. Saathoff, and U. Stark, "Spike-type stall inception in Axial Flow Compressors," in *6th Conference on Turbomachinery, Fluid Dynamics and Thermodynamics, Lille, France*, 2005.

[13] H. D. Vo, "Suppression of short length-scale rotating stall inception with glow discharge actuation," in *ASME Turbo Expo 2007: Power for Land, Sea, and Air*, 2007, pp. 267-278.

[14] H. D. Vo, "Rotating stall suppression in axial compressors with casing plasma actuation," *Journal of Propulsion and Power*, vol. 26, pp. 808-818, 2010.

[15] C. Enloe, T. E. McLaughlin, R. D. Van Dyken, K. Kachner, E. J. Jumper, and T. C. Corke, "Mechanisms and responses of a single dielectric barrier plasma actuator: plasma morphology," *AIAA journal*, vol. 42, pp. 589-594, 2004.

[16] J. W. Gregory, C. L. Enloe, G. I. Font, and T. E. McLaughlin, "Force production mechanisms of a dielectric-barrier discharge plasma actuator," *AIAA paper*, vol. 185, p. 2007, 2007.

[17] U. Kogelschatz, "Dielectric-barrier discharges: their history, discharge physics, and industrial applications," *Plasma chemistry and plasma processing*, vol. 23, pp. 1-46, 2003.

[18] T. C. Corke and M. L. Post, "Overview of plasma flow control: concepts, optimization, and applications," *AIAA paper*, vol. 563, p. 2005, 2005.

[19] T. C. Corke, M. L. Post, and D. M. Orlov, "Single dielectric barrier discharge plasma enhanced aerodynamics: physics, modeling and applications," *Experiments in Fluids*, vol. 46, pp. 1-26, 2009.

[20] J. Huang, T. C. Corke, and F. O. Thomas, "Plasma actuators for separation control of low-pressure turbine blades," *AIAA journal*, vol. 44, pp. 51-57, 2006.

[21] M. L. Post and T. C. Corke, "Separation control using plasma actuators-stationary and oscillating airfoils," *AIAA paper*, vol. 841, p. 2004, 2004.

[22] E. Potočar, B. Širok, M. Hočevar, and M. Eberlinc, "Control of Separation Flow over a Wind Turbine Blade with Plasma Actuators," *Strojniski Vestnik/Journal of Mechanical Engineering*, vol. 58, 2012.

[23] S. Lemire and H. D. Vo, "Reduction of fan and compressor wake defect using plasma actuation for tonal noise reduction," *Journal of Turbomachinery*, vol. 133, p. 011017, 2011.

[24] H. D. Vo, J. D. Cameron, and S. C. Morris, "Control of short length-scale rotating stall inception on a high-speed axial compressor with plasma actuation," in *ASME Turbo Expo 2008: Power for Land, Sea, and Air*, 2008, pp. 533-542.

[25] C. Nie, Z. Tong, S. Geng, J. Zhu, and W. Huang, "Experimental investigations of micro air injection to control rotating stall," *Journal of Thermal Science,* vol. 16, pp. 1-6, 2007.

[26] H. Emmons, C. Pearson, and H. Grant, "Compressor surge and stall propagation," *Trans. AsME,* vol. 77, pp. 455-467, 1955.

[27] F. Moore and E. Greitzer, "A theory of post-stall transients in axial compression systems: Part I—Development of equations," *Journal of Engineering for Gas Turbines and Power,* vol. 108, pp. 68-76, 1986.

[28] H. D. Vo, "Role of tip clearance flow on axial compressor stability," Massachusetts Institute of Technology, 2001.

[29] H. D. Vo, C. S. Tan, and E. M. Greitzer, "Criteria for spike initiated rotating stall," *Journal of Turbomachinery,* vol. 130, p. 011023, 2008.

[30] J.-P. Chen, M. D. Hathaway, and G. P. Herrick, "Prestall behavior of a transonic axial compressor stage via time-accurate numerical simulation," *Journal of Turbomachinery,* vol. 130, p. 041014, 2008.

[31] M. A. Bennington, J. D. Cameron, S. C. Morris, and C. P. Gendrich, "Over rotor casing surface streak measurements in a high speed axial compressor," in *ASME Turbo Expo 2007: Power for Land, Sea, and Air*, 2007, pp. 445-455.

[32] D. Japikse, *Centrifugal compressor design and performance*: Concepts Eti, 1988.

[33] I. Day, "Active suppression of rotating stall and surge in axial compressors," *Journal of Turbomachinery,* vol. 115, pp. 40-47, 1993.

[34] A. J. Strazisar, M. M. Bright, S. Thorp, D. E. Culley, and K. L. Suder, "Compressor stall control through endwall recirculation," in *ASME Turbo Expo 2004: Power for Land, Sea, and Air*, 2004, pp. 655-667.

[35] G. Jothiprasad, A. Wadia, A. Breeze-Stringfellow, R. C. Murray, K. Essenhigh, G. A. Bennett, *et al.*, "Control of Tip-Clearance Flow in a Low Speed Axial Compressor Rotor With Plasma Actuation," *Journal of Turbomachinery,* vol. 134, p. 021019, 2012.

[36] G. J. Skoch, "Experimental investigation of centrifugal compressor stabilization techniques," in *ASME Turbo Expo 2003, collocated with the 2003 International Joint Power Generation Conference*, 2003, pp. 765-776.

[37] S. Roy, K. Singh, H. Kumar, D. V. Gaitonde, and M. Visbal, "Effective discharge dynamics for plasma actuators," *AIAA paper,* vol. 374, p. 2006, 2006.

[38] B. Jayaraman, Y.-C. Cho, and W. Shyy, "Modeling of dielectric barrier discharge plasma actuator," *Journal of Applied Physics,* vol. 103, p. 053304, 2008.

[39] D. V. Gaitonde, M. R. Visbal, and S. Roy, "A coupled approach for plasma-based flow control simulations of wing sections," *AIAA paper,* vol. 1205, p. 2006, 2006.

[40] W. Shyy, B. Jayaraman, and A. Andersson, "Modeling of glow discharge-induced fluid dynamics," *Journal of Applied Physics,* vol. 92, pp. 6434-6443, 2002.

[41] Y. Suzen and P. Huang, "Simulations of flow separation control using plasma actuators," *AIAA paper,* vol. 877, p. 2006, 2006.

[42] D. M. Orlov, T. Apker, C. He, H. Othman, and T. C. Corke, "Modeling and experiment of leading edge separation control using SDBD plasma actuators," *AIAA paper,* vol. 877, p. 2007, 2007.

[43] D. Palmeiro and P. Lavoie, "Comparative analysis on single dielectric barrier discharge plasma actuator models," in *7th International Symposium on Turbulence and Shear Flow Phenomena, Ottawa, Canada*, 2011.

[44] R. Mailach, I. Lehmann, and K. Vogeler, "Rotating instabilities in an axial compressor originating from the fluctuating blade tip vortex," *Journal of Turbomachinery,* vol. 123, pp. 453-460, 2001.

[45] C. Ansys, "Release 13.0, CFX-"Solver theory guide"," Technical report, Ansys2010.

[46] P. Versailles, V. Gingras-Gosselin, and H. D. Vo, "Impact of pressure and temperature on the performance of plasma actuators," *AIAA journal,* vol. 48, pp. 859-863, 2010.

[47] F. O. Thomas, T. C. Corke, M. Iqbal, A. Kozlov, and D. Schatzman, "Optimization of dielectric barrier discharge plasma actuators for active aerodynamic flow control," *AIAA journal*, vol. 47, pp. 2169-2178, 2009.

[48] X. Xu, H. D. Vo, N. Mureithi, and X. F. Zhang, "Turbulent Boundary Layer Separation Control by Using DBD Plasma Actuators: Part I—Experimental Investigation," in *ASME 2010 International Mechanical Engineering Congress and Exposition*, 2010, pp. 1-13.

[49] N. Balcon, N. Benard, Y. Lagmich, J.-P. Boeuf, G. Touchard, and E. Moreau, "Positive and negative sawtooth signals applied to a DBD plasma actuator–influence on the electric wind," *Journal of electrostatics,* vol. 67, pp. 140-145, 2009.

[50] D. Martial, "Development of a method of simulation of surge in a multistage compressor," Master of applied science Masters thesis, École Polytechnique de Montréal, 2013.

[51] E. M. Greitzer, "Surge and rotating stall in axial flow compressors—Part I: Theoretical compression system model," *Journal for Engineering for Power,* vol. 98, pp. 190-198, 1976.

[52] E. M. Greitzer, "Surge and rotating stall in axial flow compressors—Part II: experimental results and comparison with theory," *Journal for Engineering for Power,* vol. 98, pp. 199-211, 1976.

APPENDIX A- Experimental Setup and Measurements details

The side cross-section of the compressor is shown in figure 3.2; also the instrumentations installed over the compressor shown in the picture are listed in table 3.2. The necessary data to plot the speedline of compressor stages are measured via the instrumentations installed over the compressor, once these analogue data are recorded they are sent to the instruments that are not installed over the compressor to be transformed to digital data that can be read in the LabView interface. It is also possible to measure other data such as tip-clearance size, and to change the position of total pressure tubes via a servo-motor mechanism by the provided devices. Pictures of the compressor assembly and table of the instrumentation are shown in figures A.1 and A.2.

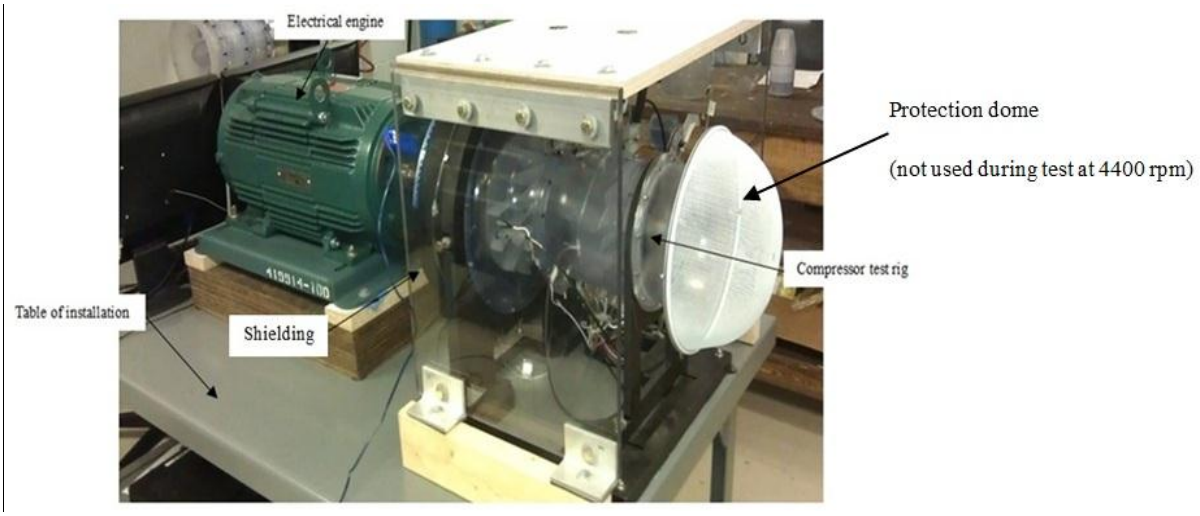

Figure A.1: Assembly of compressor test rig

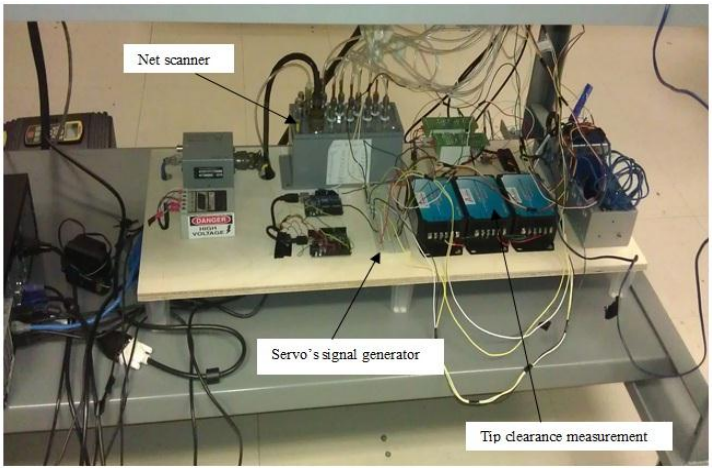

Figure A.2: System of instrumentation installed over a board

The mechanism of throttle setting is shown in figure A.3. For the facility of opening and closing the valve an electric jack is provided.

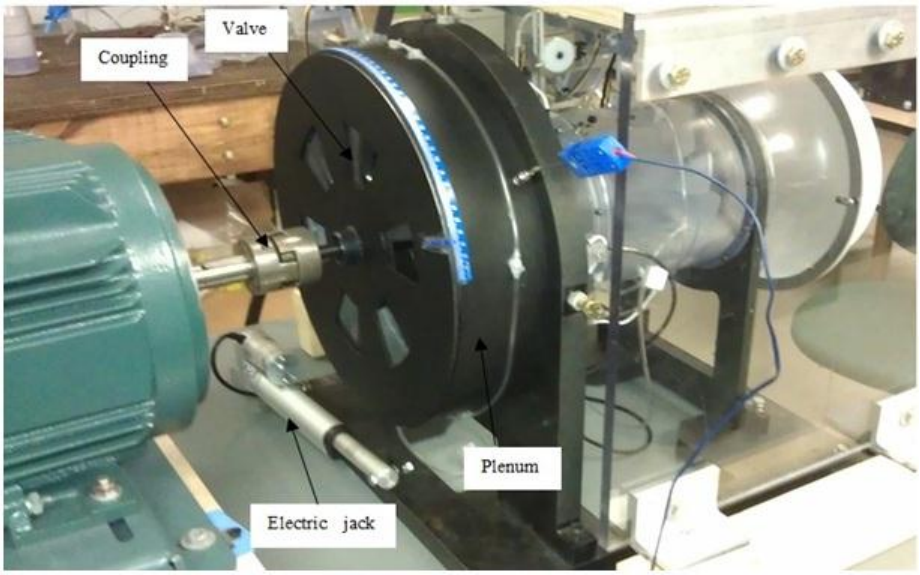

Figure A.3: Throttle setting mechanism

Measurements

The most important measurements for speedline are (P_{amb},T_{amb}, P_{s1}, P_{s3}, P_{s4}, P_{s7}, P_{T7}). The main parameters to be calculated for the speedlines are:

1) $\psi_{Ts} \equiv \frac{P_{sout}-P_{amb}}{\frac{1}{2}\rho U_{tip}^2}$ Vertical axis (A.1)

Where $\rho \cong constant = \rho_{T0}$ and $U_{tip} = 40.8\frac{m}{s} at\ 4400\ RPM$

and $P_{sout}=$ $\begin{cases} P_{s2} & for\ axial\ rotor \\ P_{s4} & for\ axial\ stage \\ P_{s7} & for\ two-stage \end{cases}$

2) $\psi_{Ts} \equiv$PR$\equiv \frac{P_{s7}}{P_{amb}}$ (For centrifugal compressor) (A.2)

3) Horizontal axis, Corrected Mass Flow Rate, $\dot{m}$.

- Density at the inlet where $P_{T0} = P_{atm}$ is

$$\rho_{T0} = \left(\frac{1}{287.06*(T_{T0}+273.15)}\right) * \left[P_{T0} - 230.617 * Humidity * \exp\left(\frac{17.5043*T_{T0}}{241.2+T_{T0}}\right)\right] \quad \text{(A.3)}$$

- Isentropic mass flow rate

$$dp = P_{atm} - P_{s1} \rightarrow V_{isen} = \sqrt{\frac{2*dp}{\rho_{T0}}} \rightarrow \dot{m}_{isen} = V_{isen} * \rho_{T0} * A \quad \text{(A.4)}$$

- Discharge coefficient (Considering boundary layer thickness)

$$\text{Cd} = -179.76 * \dot{m}_{isen}{}^{6} + 502.46 * \dot{m}_{isen}{}^{5} - 583.35 * \dot{m}_{isen}{}^{4} + 359.79 * \dot{m}_{isen}{}^{3} - 124.25 * \dot{m}_{isen}{}^{2} + 22.774 * \dot{m}_{isen} - 0.7501 \quad \text{(A.5)}$$

Equation (A.5) is obtained by the designers of the rig.

$$\dot{m} = \text{Cd} * \dot{m}_{isen} * 0.45359237 \quad \text{(A.6)}$$

(0.45359237 for conversion from lb/s to kg/s)

- And finally converting to corrected mass flow rate.

$$\dot{m}_{corrected} = \dot{m} * \frac{\sqrt{\frac{T_{T0}}{288.15}}}{\frac{P_{T0}}{101325}} \quad \text{(A.7)}$$

APPENDIX B- Plasma generation system and actuator strength measurement

B.1 Plasma generation system

This system as shown in figure B.1 consists of a signal generator, power amplifiers, ballast resistor module and transformers.

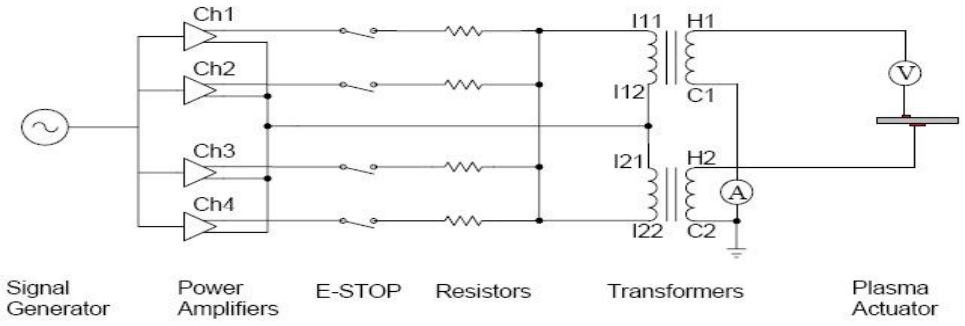

Figure B.1: Schematic of plasma generation system

For AC signal generating, standard signal generators or NI DAQ cards (e.g. PCI-6110) can be used. The signal generated is in forms like, sine, square, triangle and sawtooth. The signal is then sent to two Crown XTi-4000 Power Amplifiers powered by two independent AC line sources (110 W, 15 A), consisting of totally four channels with the same amplification ratio. In addition to power switches, an emergency stop is provided to cut off AC power supply directly from line sources. Four channels of amplifier are connected to four ballast resistor module (2ohm, 300W) which are mounted on a PC board, and are lifted 0.5 inches to avoid over-heating of the board. Four outputs of resistors are connected together which then connect to two CMI-5525 transformers made by Corona Magnetics to obtain high AC voltage. Each of these transformers which are mounted on a porous aluminum plate has a turns ratio (secondary to primary) of 360:1,working frequency of 0.9-5 KHz with maximum output of 25 KV_{rms} .In order to obtain a total ratio of 720:1, they are connected in parallel. As shown in figure B.1, C1 and C2 are connected to ground, and H1, H2 each is connected to one electrode. The assembly is shown in figure B.2, the bottom to top order of components is amplifiers, ballast resistor module and transformers, the system is cooled with a fan, also for safety and to avoid high voltage discharge,

any metallic component should be kept at a distance from high voltage leads of transformers, and also all metallic cases and plates are grounded. The high voltage between actuators is measured via a PVM-3 high voltage probe (40 KVDC, max frequency of 40 MHz, divider ratio of 10000:1), made by North Star High Voltage, this probe is put near one electrode, doubling the value measured, gives us the voltage difference between the plasma actuator electrodes.

Figure B.2: Assembly of plasma generation system

B.2 Actuation strength measurement

To obtain an actuator strength of about 100 mN/m and associate required input for the experiments, a little setup was built to measure actuator strength. Annular plasma actuator is installed over a free casing, and is oriented in a direction in which the induced flow is blowing upward, i.e. the streamwise direction is vertical, the free casing (the same material and same thickness as the compressor casing), is placed over a wooden rod, which is placed over a high-precision balance (Sartorius) with 10 Kg capacity and 0.01 g resolution. This arrangement allows the air to be sucked from below, with this technique the downward acting reactive thrust which is produced by the plasma induced flow is measured for a range of frequencies and voltages

applied in order to find a suitable frequency and voltage to obtain 100 mN/m. This arrangement is shown in figure B.3.

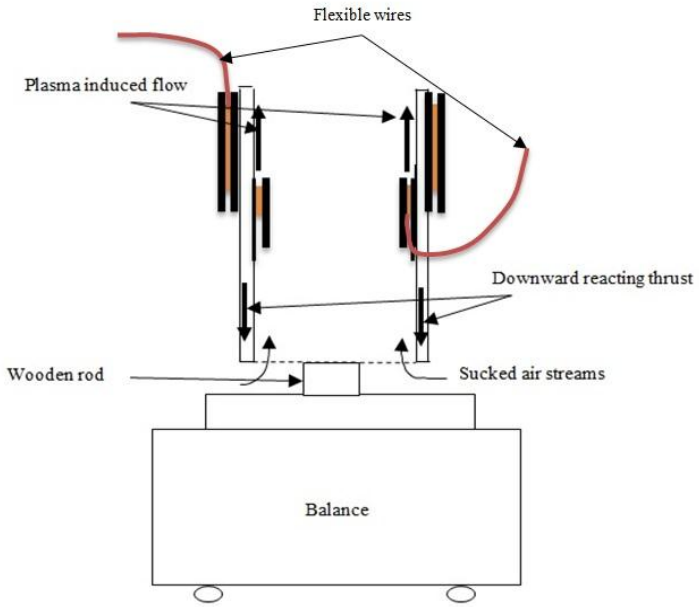

Figure B.3: Arrangement for actuator strength measurement

It should be noted that measured reactive thrust is actually the actuator strength minus the viscous shear force at the surface as shown by Versailles et al. [46].

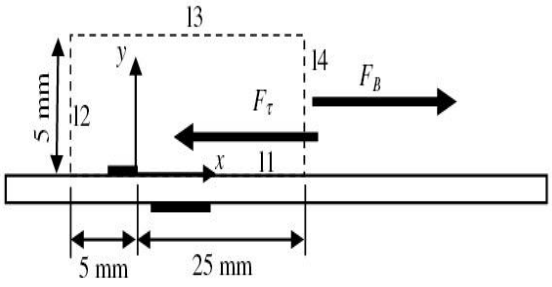

Figure B.4: Control volume for induced body force computation

F_τ which is wall shear force that can be calculated from velocity gradient at the wall, the momentum equation in x direction (Equation B.1) gives the imparted body force F_B, (so thrust measured is a reduced amount of real actuator strength). CFD simulations of plasma actuator on a flat plate at static air condition estimated that shear force is about 25 % of imparted body force, so it can be deduced that reactive thrust measured is about 75% of actuator strength, so every value measured as thrust must be multiplied by 1.333 to obtain real actuator strength.

$$F_B - \int_{l1} \mu \frac{du}{dy} dx = - \int_{l2} \rho u^2 \, dy + \int_{l3} \rho uv dx + \int_{l4} \rho u^2 dy \quad \text{(B.1)}$$

B.3 Plasma actuator characterization

The results of the tests are plotted in figure B.5. Thomas et al. [47] showed that the thrust is inversely related to the frequency of the signal generated. Furthermore Xu [48] and Balcon et al. [49] showed that negative sawtooth gave greater thrust for the same power consumption than the sinusoidal input. Thus a negative sawtooth input at lower frequency range was used.

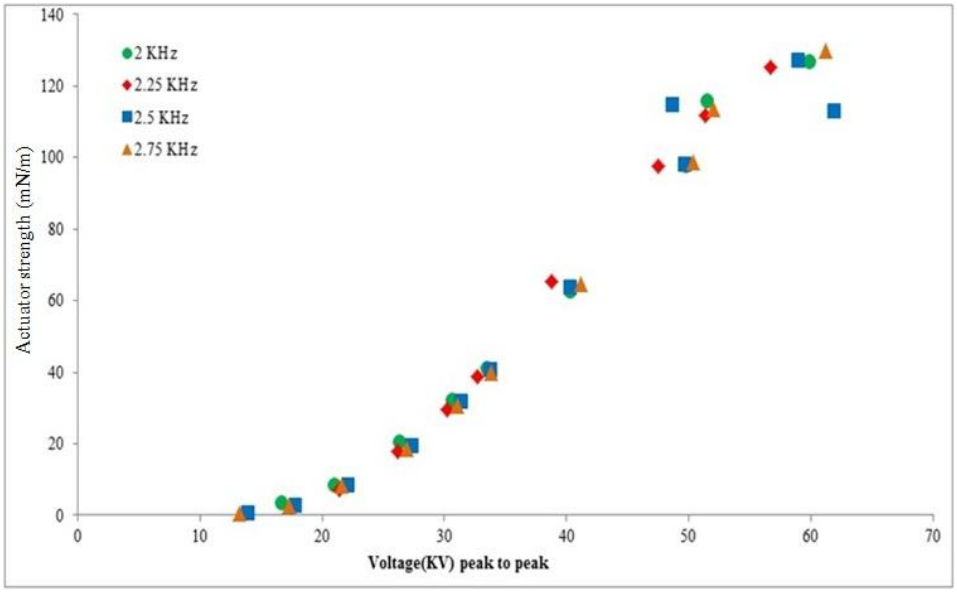

Figure B.5: Actuation strength as a function of voltage

Figure B.5 shows the actuator strength per unit length as a function of peak-to-peak voltage for several low AC frequencies ranging from 2 KHz to 2.75 KHz. Past 100mN/m, the plasma is almost in filamentary mode and is not recommended for use (inefficient, not good for actuator wear). Thus 2.5 KHz frequency can be used for the tests on the compressor test rig, and the value of 100mN/m is used for doing CFD simulations. The values on the vertical axis are the real actuator strength but not the measured reactive thrust, so this value is applied for simulations. In order to find a relation between the thrust and peak-to-peak voltage, figure B.5 is again plotted in logarithmic scale for both axes and the points are connected via a linear trendline. The slope of all these lines is between 3 to 3.5, close to 3.5, which is so close to the relation found by Thomas et al.[47] as a power law which gives

$$T \propto V^{3.5} \rightarrow \ln T \ = 3.5 * lnV \quad \text{(B.2)}$$

Trendlines are all good fits since their R^2 are almost equal to 1.

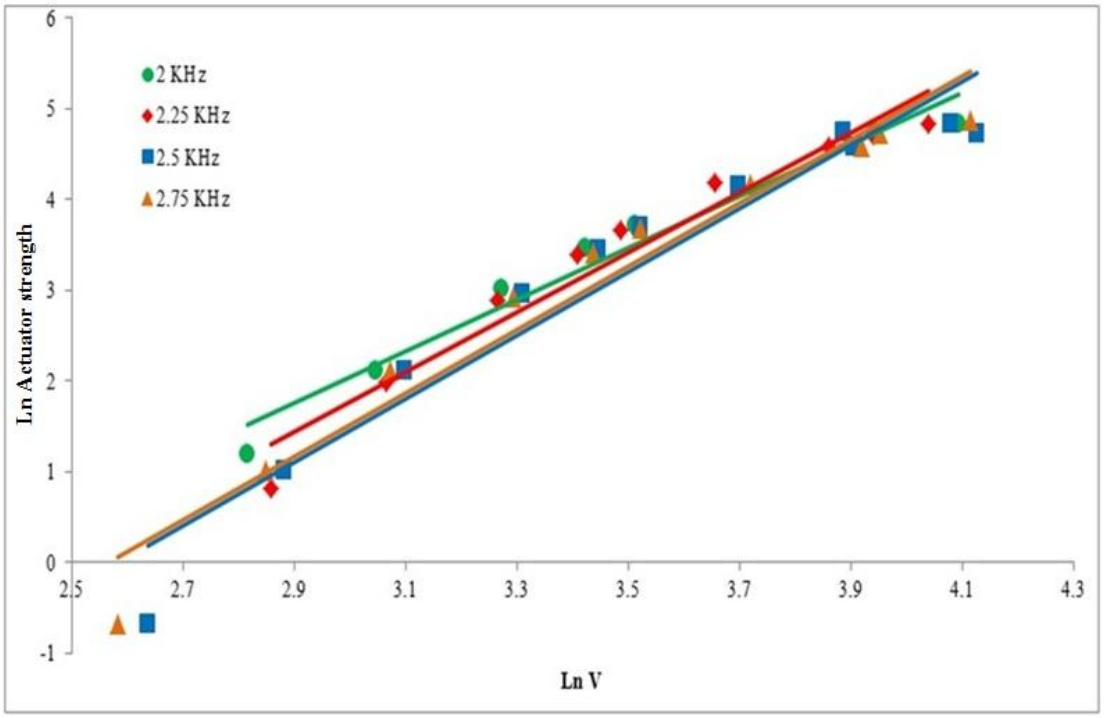

Figure B.6: Logarithmic plot of actuator strength as a function of voltage

APPENDIX C- Throttle exit boundary condition

Dumas [50] created a hybrid model of compression system which links numerical resolution of 3D Navier-Stokes equations with 1D analysis for surge simulation.

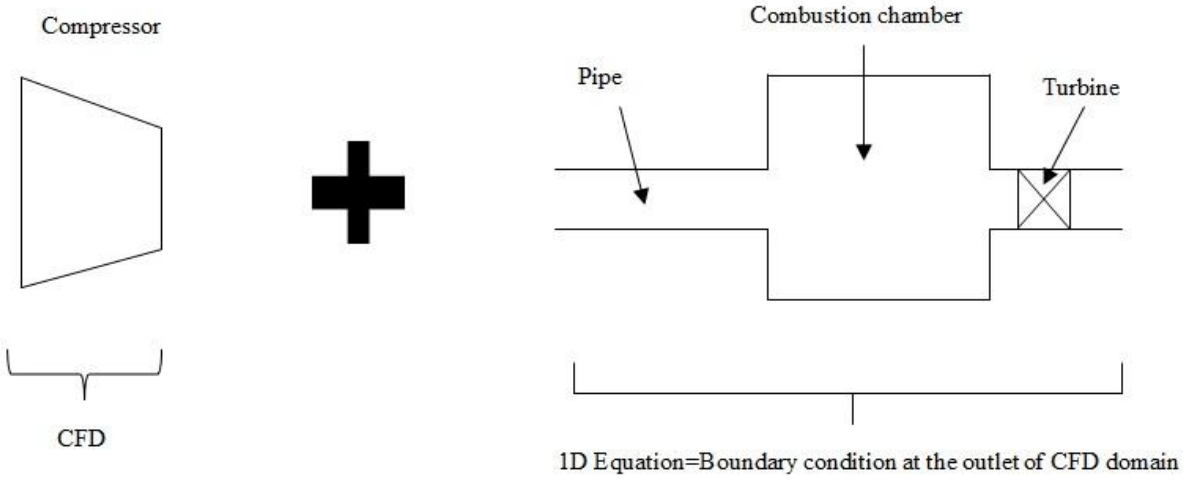

Figure C.1: General principle of the numerical method

As illustrated in figure C.1, the compressor is simulated in 3D via CFD as the principle element under study, while the combustion chamber (plenum) and turbine (valve) are modeled as a 1D equation to provide a dynamic static pressure boundary condition at the exit of the simulation domain (compressor).

Dumas performed 1D modeling of (combustion chamber, turbine) using the model of Greitzer [51, 52] in Greitzer's model compressor is also modeled by (actuator disc theory) which considers compressor as a disc with infinitesimal thickness (only flow properties at its upstream and downstream are considered), combustion chamber is replaced by a plenum of volume V_p. In the plenum pressure P, temperature T and density ρ are uniform and fluid velocity is almost zero i.e. $v = 0$. Turbine is modeled by a valve that can be opened or closed. So, Greitzer's model is completely 1D as shown in figure C.2.

Dynamic boundary conditions modeling

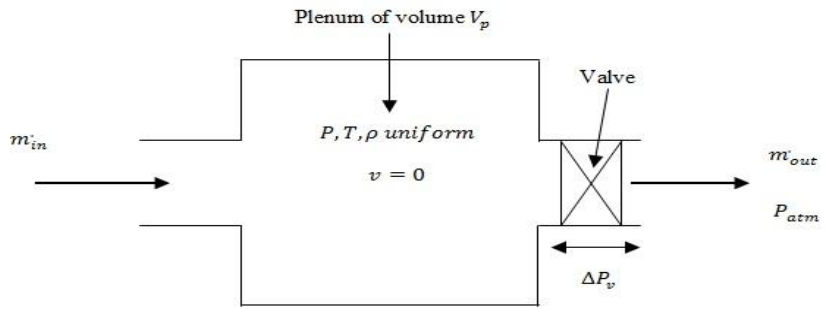

Figure C.2: Schematic of 1D model

As shown in figure C.2, the combustion chamber is modeled as a plenum volume with uniform isentropic compressibility while the turbine is represented by a valve with a quadratic relation between pressure drop and mass flow.

To obtain the governing equations of this 1D model, the following indices are used:

$: for\ plenum \quad v: for\ valve \quad c: for\ compressor \quad s: for\ static$

$in: for\ inlet\ of\ the\ model\ shown\ in\ figure\ 3.29\ \&\ \ out: for\ its\ outlet$

Procedure for obtaining the governing boundary condition for outlet of compressor.

- Conservation of mass for plenum

$$\dot{m}_{in} - \dot{m}_{out} = \frac{d(\rho_p V_p)}{dt} = V_p \frac{d(\rho_p)}{dt} \tag{C.1}$$

- Perfect gas law

$$P = \rho \tilde{R} T \tag{C.2}$$

Where $\tilde{R} = 287\ \frac{J}{Kg.K}$, perfect gas constant for air

The system in the plenum is considered to be isentropic, so we have

$$^{\gamma}T^{\gamma} = constant \tag{C.3}$$

Where $\gamma = adiabatic\ coefficient\ of\ air = 1.4$

$$\frac{d(\rho_p)}{dt} = \frac{1}{\tilde{R}}\frac{d(\frac{P_p}{T_p})}{dt} = \frac{}{\tilde{R}\gamma T_p}\frac{dP_p}{dt} = \frac{}{c^2}\frac{dP_p}{dt} \tag{C.4}$$

Where $c = sound\ speed\ in\ the\ air$

- Substituting equation (C.4) in (C.1) gives equation (C.5).

$$\frac{dP_p}{dt} = \frac{c^2}{V_p}(\dot{m}_{in} - \dot{m}_{out}) \tag{C.5}$$

This equation gives instantaneous variation of pressure in the plenum as a function of volume of plenumV_p, sound speed c as well as inlet and outlet mass flow rates $\dot{m_{in}}, \dot{m_{out}}$.

With the help of following non-dimensional variables, it is possible to obtain more useful equations; furthermore, non-dimensionalizing helps comparison between different geometries without considering other parameters. Dimensionless variables are:

1) $\emptyset = \frac{v_{normal}}{U}: dimensionless\ mass\ flow\ coefficient$
2) $\psi = \frac{P_p \quad P_{total,inlet}}{\rho_{inlet}U^2}: dimensionless\ total\ to\ static\ pressure\ coefficient$
3) $\varepsilon = \frac{t*U}{R}$: dimensionless time coefficient
4) $l_c = \frac{L_c}{R}: dimensionless\ length, Raverage\ radius\ of\ compressor$
5) $B = \frac{U}{2*C}\sqrt{\frac{V_p}{S_c L_c}}: coefficient\ B\ of\ Greitzer$
6) $U: rotor\ tip\ speed$
7) $\rho_{inlet}: density\ at\ inlet, constant$

- Equation (C.5) can be rewritten in terms of $\emptyset$ Instead of $\dot{m}$ as

$$\frac{dP_p}{dt} = \frac{U*\rho_p*S_c*c^2}{V_p}(\emptyset_{in} - \emptyset_{out}) \quad \text{(C.6)}$$

- Then

$$\psi = \frac{P_p - P_{total,inlet}}{\rho_{inlet}U^2} \quad \rightarrow \quad d\psi = \frac{1}{\rho_{inlet}U^2}dP_p \rightarrow dP_p = \rho_{inlet}U^2 d\psi \quad \text{(C.7)}$$

And

$$\varepsilon = \frac{t*U}{R} \rightarrow d\varepsilon = \frac{U}{R}dt \rightarrow dt = \frac{R}{U}d\varepsilon \quad \text{(C.8)}$$

- Substituting (C.7) and (C.8) in (C.6) and doing some simplifications, gives

$$\frac{\partial\psi}{\partial\varepsilon} = \frac{\rho_p}{\rho_{inlet}}\frac{1}{4B^2 l_c}(\emptyset_{in} - \emptyset_{out}) \quad \text{(C.9)}$$

- Turbine is modeled with a valve, and the pressure drop across that is modeled by a coefficient (K_t) in equation (C.10).

$$\Delta P_v = \frac{1}{2}K_t \rho v_{normal}^2 \quad \text{(C.10)}$$

If static pressure at plenum outlet is supposed to be equal to the total pressure at compressor inlet, so total to static pressure rise across the compressor ΔP_c corresponds to static pressure drop across the turbineΔP_v.

- Non-dimensionalizing equation (C.10) gives

$$\psi = \frac{1}{2}K_t {\emptyset_{out}}^2 \quad \text{(C.11)}$$

- Finally combination of equations (3.10) and (3.12) gives.

$$\frac{\partial\psi}{\partial\varepsilon} = \frac{\rho_p}{\rho_{inlet}}\frac{1}{4B^2 l_c}\left(\emptyset_{in} - \sqrt{\frac{2\psi}{K_t}}\right) \quad \text{(C.12)}$$

For incompressible flows $\frac{\rho_p}{\rho_{inlet}}$ is almost equal to 1,with the help of equation (C.12) when related to the boundary condition of CFD domain, stall and surge can be modeled in a compressor.

For applying dynamic boundary condition to CFD simulations, as explained in previous section, the principle element under study which is resolved in 3D CFD simulations is compressor, so from now on indexes in & out correspond to the inlet and outlet of compressor.

For simulating stall or surge, as long as compressor behavior is in the transient part of the speedline (past the steady-state part), a dynamic or (variable with time) static pressure rather than a constant static pressure is applied at the compressor outlet to precisely model the flow in the compressor. It is considered that the conditions at compressor outlet (pressure, temperature, density, mass flow) correspond to the plenum. This dynamic (static pressure) is calculated from discretization of equation (C.12)

$$Ps_{out}(t+\delta t) = Ps_{out}(t) + \frac{\rho_{out} U^2 \delta t}{4B^2 L_c}\left(\frac{\dot{m}_{outlet}(t)}{\rho_{out} * S_c} - \sqrt{\frac{2 * Ps_{out}(t)}{\rho_{inlet} * K_t}}\right) \quad \text{(C.13)}$$

It is now clear that static pressure at compressor outlet at time $t+\delta t$ is calculated from mass flow rate and static pressure at previous time iteration or t. This static pressure is considered as the outlet boundary condition for the compressor. As long as when the compressor is stalled the flow is still in positive direction and is not reversed like what happens during surge, the following boundary conditions can be considered for performing the simulations.

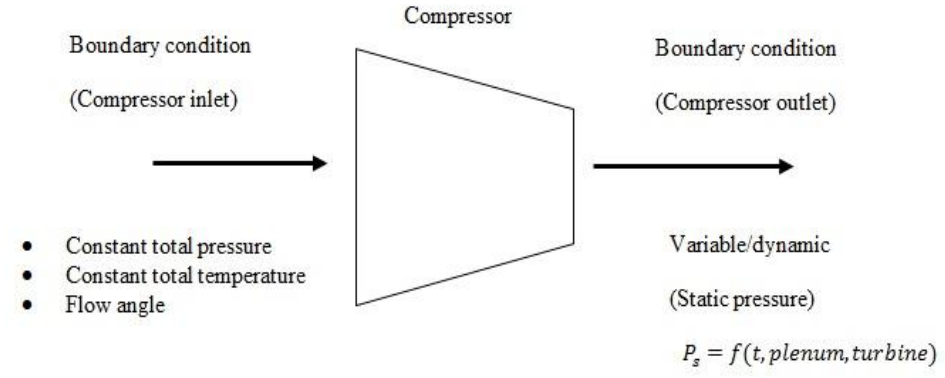

Figure C.3: Boundary conditions applied at inlet and outlet of compressor for transient regime

For the steady-state part of the speedline the static pressure at the compressor outlet is constant over time, but the same settings for boundary conditions as shown in figure C.3 can still be used for performing the simulations. In steady-state part applying constant static pressure or dynamic (static pressure) gives the same result, because even if dynamic pressure is used, it very soon converges to a constant value and this constant value is applied over the time of simulation. So for the simulations and obtaining the complete speedline till the stall point, the dynamic (static pressure, $Ps_{out}(t + \delta t)$) as sketched in figure C.3 and calculated in equation (C.13) is used.

APPENDIX D- Comparison of full two-stage compressor simulation with isolated axial rotor simulation

In addition to the simulations performed on the two-stage compressor, a set of simulations were also performed on just the axial rotor to assess the effect of centrifugal stage on the axial stage.

The computational domain is shown in figure D.1. A duct length of one-blade pitch in axial length is provided downstream of the rotor trailing edge for attenuation of circumferential flow non-uniformity in the blade passage to zero for compatibility with the circumferential uniform exit boundary condition.

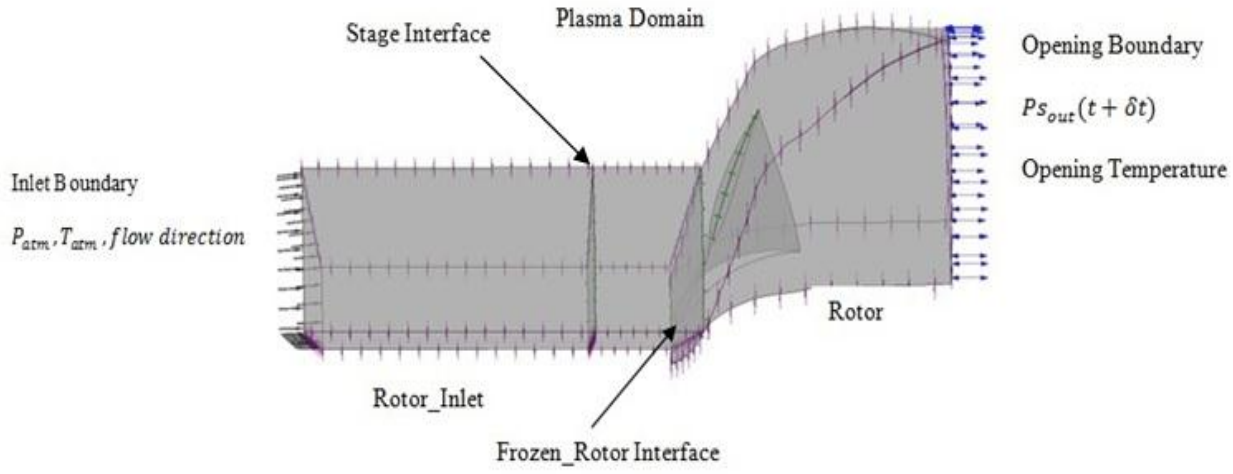

Figure D.1: Schematic of the numerical setup of axial rotor (alone)

The speedline of the simulation for the isolated rotor shown in figure D.1 with that of figure 3.6 are compared in figure D.2.

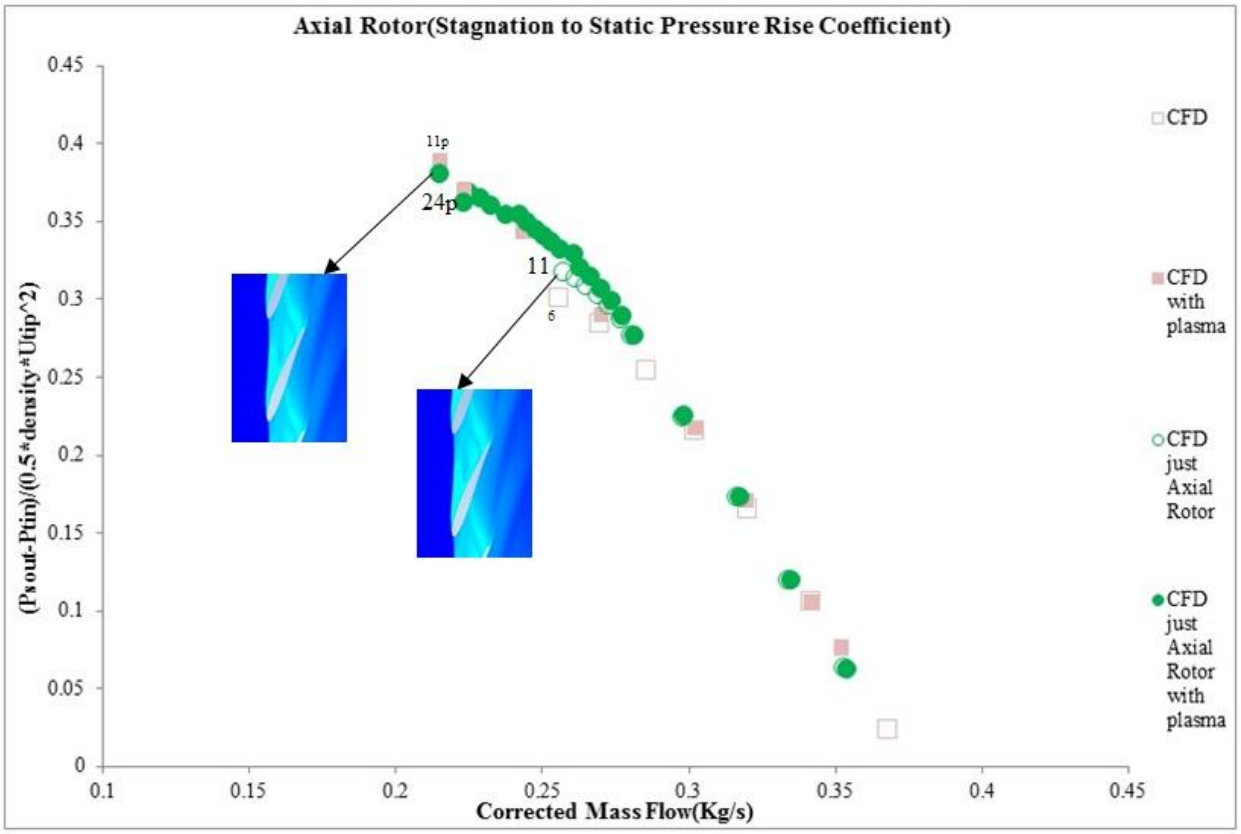

Figure D.2: Axial rotor speed-line for two different configurations

The results show that the predicted speedline is virtually the same, in addition the incoming/tip clearance flow interface criterion for stall occurs at the same mass flow rates in both configurations for cases without and with plasma. Therefore it can be said that circumferential stage has almost no effect on the axial stage. Thus evaluating the effect of plasma on the axial isolated rotor may be sufficient.

APPENDIX E- The effect of simulating the real plenum instead of virtual end-duct domain

As explained in section 3.2 the end-duct domain with virtual hub and shroud aligned with the diffuser's hub and shroud, was used to model the static pressure distribution over the diffuser outlet plane. This configuration allowed for a smaller domain compared to the real plenum and thus lower computational time and resources. The results of simulating a point near stall at 3470 RPM with this domain and the same point with real plenum modeling are compared in figures E.1 and E.2. For simulation with plenum the amount of opening of the valve is fixed and the pressure at the opening is fixed to be equal to ambient conditions.

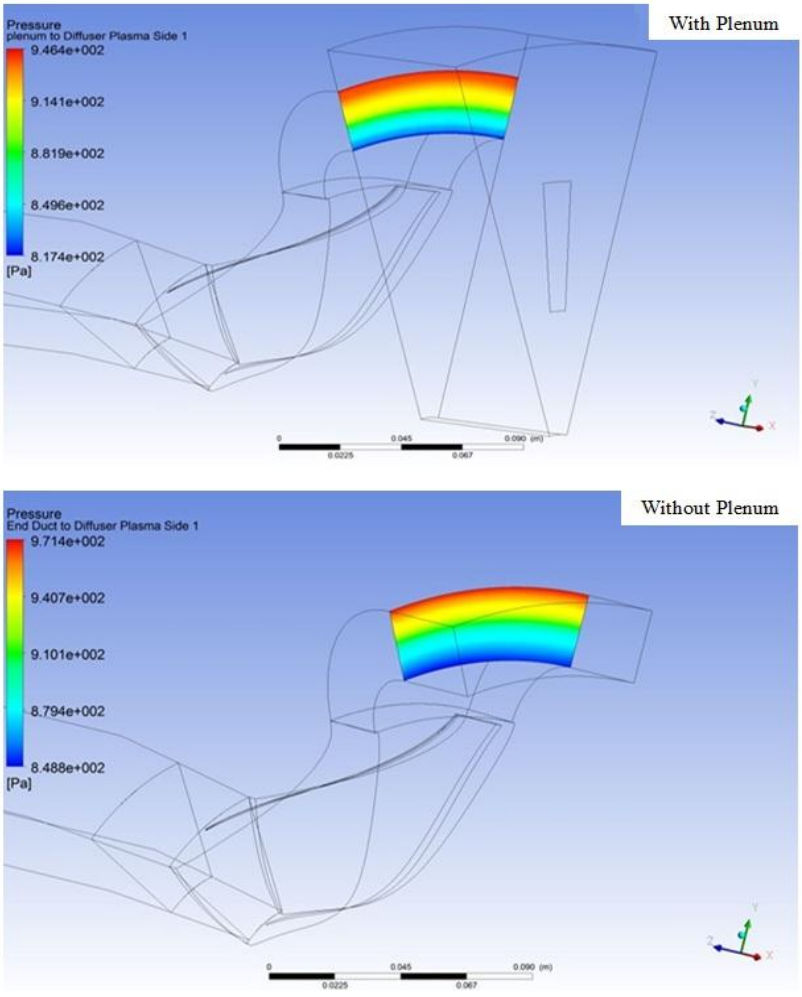

Figure E.1: Comparison of static pressure distribution over diffuser outlet plane

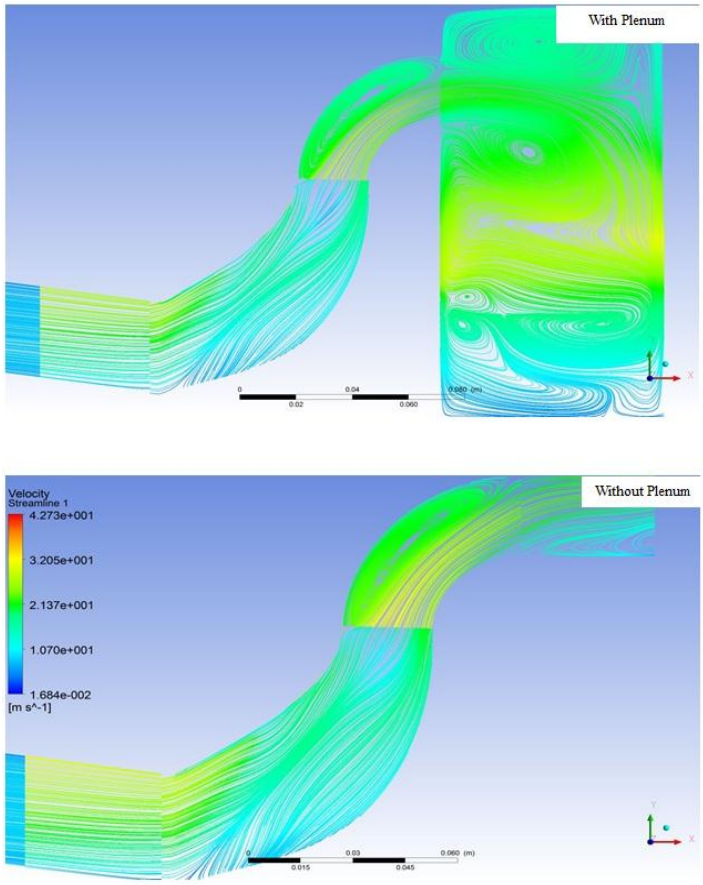

Figure E.2: Comparison between velocity streamlines in meridional view

As is illustrated in figure E.2 the size of recirculation zone near diffuser shroud does not change in simulation without and with plenum. The static entropy contours also show the same position for the low entropy incoming flow and high entropy tip clearance flow interface. Table E.1 summarizes the results of comparison and shows that using a small end-duct gives the results with good agreement as those from simulations of the real plenum. Note that the difference in area average of pressure at diffuser outlet is 1.9% of ΔP_{TS} across compressor, so the difference can be neglected.

Table E.1: Comparison between results (without and with plenum)

	Corrected mass flow(Kg/s)	**Area average of pressure at diffuser outlet(Pa)**
With plenum	0.16958	891.008
Without plenum	0.16566	908.518

APPENDIX F- Plasma Actuator Model Implementation

The implementation of the DBD plasma actuator model essentially consists of mapping the time-averaged spatial body force distribution of Lemire et al. [23] from their fine 2-D Cartesian mesh onto the coarse CFD mesh of the plasma sub-domain created in GAMBIT at the determined location of the plasma actuator using the procedure laid out by Vo [14]. The process starts with exporting the coordinates of a periodic side of the perfectly cylindrical CFD mesh of the *Plasma* sub-domain in the axial-radial plane and superposing over it the fine 2-D Cartesian actuator mesh at the desired position of the actuator as illustrated in figure F.1. The body force per unit depth for each CFD cell is the sum of the values from smaller fine actuator mesh cells lying within it, modulated by the proportion of their areas lying within the CFD cell, as shown in figure F.2. This value is then multiplied by the effective depth of the 3-D cell volume to get the body force associated with the CFD cell. The body force distribution is then multiplied by a factor so that the integrated value equals the desired actuator strength. Figure F.3 shows the final transferred body force distribution on the CFD mesh.

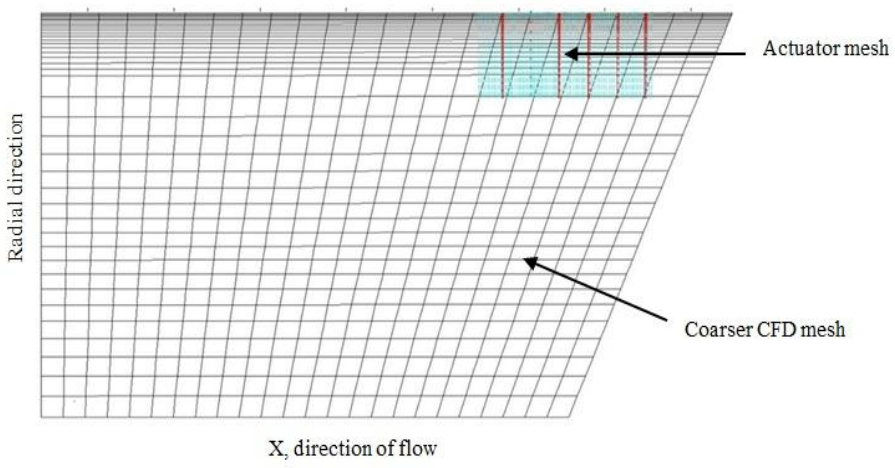

Figure F.1: Actuator mesh mapped onto CFD mesh

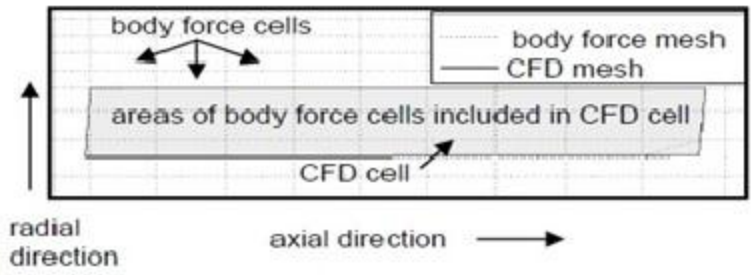

Figure F.2: Body force mapping process [14]

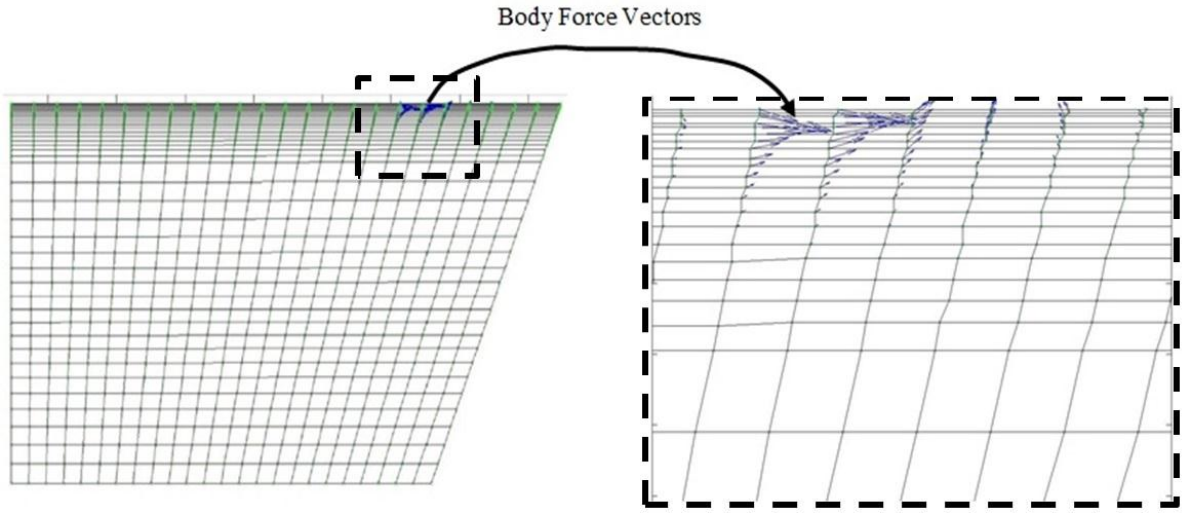

Figure F.3: Plasma body force distribution over CFD mesh

User FORTRAN option in ANSYS-CFX [45] (subroutines, user functions, shared libraries), help to implement this body force distribution in CFD simulations. Since the body force produced by the MATLAB code is 300 mN/m, a scale factor of 1/3 is applied to the vector force field.

APPENDIX G- Assessment of plasma actuation strategies

Plasma actuation is applied at different locations to find the best place for delaying rotating stall in centrifugal compressor.

G.1 Streamwise plasma at diffuser inlet

It is applied just at the inlet of diffuser domain, after the impeller TE. The interface of electrodes is at a distance of 3.5 mm from diffuser inlet and 6 mm from impeller trailing edge. This is the closest possible distance for the interface of electrodes.

G.2 Circumferential plasma at diffuser inlet

The other configuration is circumferential plasma at the mid pitch (50 %) of the passage of the diffuser domain. Plasma in this case is only applied for around 20% of length of shroud at the inlet of diffuser in the stream-wise direction.

G.3 Stream-wise plasma at Impeller LE

The plasma is applied at the impeller LE plane in the tip region. The effect of these actuation configurations on velocity contours is shown in figure G.1

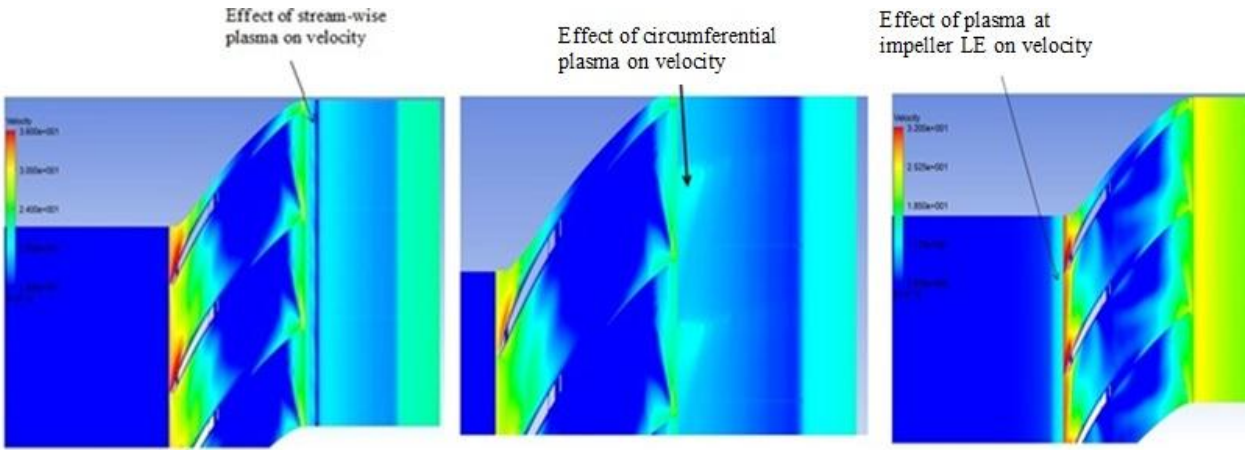

Figure G.1: Effect of different plasma configurations on velocity

And also the effect of different configurations on surface velocity streamlines for point 10 on speedline (figure G.3), is highlighted in figure G.2.

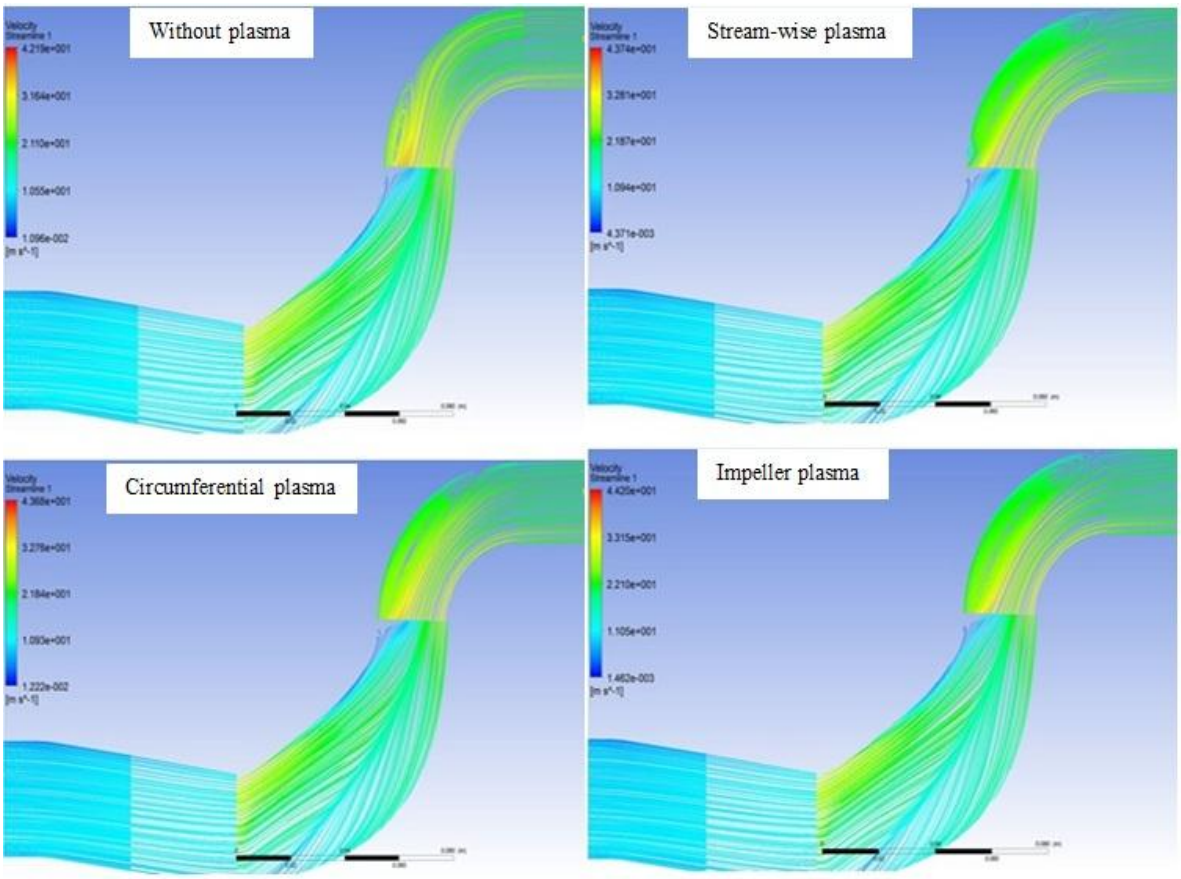

Figure G.2: Effect of different configurations on surface streamlines

As can be seen stream-wise plasma at diffuser inlet and impeller plasma increase meridional flow velocity which with the same discussions as section 4.2 for velocity triangles it can be said that the amount of separation and size of recirculation zone increases. Circumferential velocity cannot increase absolute flow angle effectively and it has also the same tendency to increase the recirculation zone size.

A comparison between the length of a single streamline in the diffuser (from its inlet to its outlet) for point 10 on the speedline for the three different cases is done.

Streamline length ➡ Without Plasma>Circumferential Plasma>Impeller Plasma>Stream-wise Plasma

Figure G.3 shows the speedline of the centrifugal compressor at 3700 RPM.

The vertical axis is the ratio of area-averaged static pressure over diffuser outlet plane to the mass-averaged total pressure over a plane 10% axial chord upstream of impeller leading edge plane.

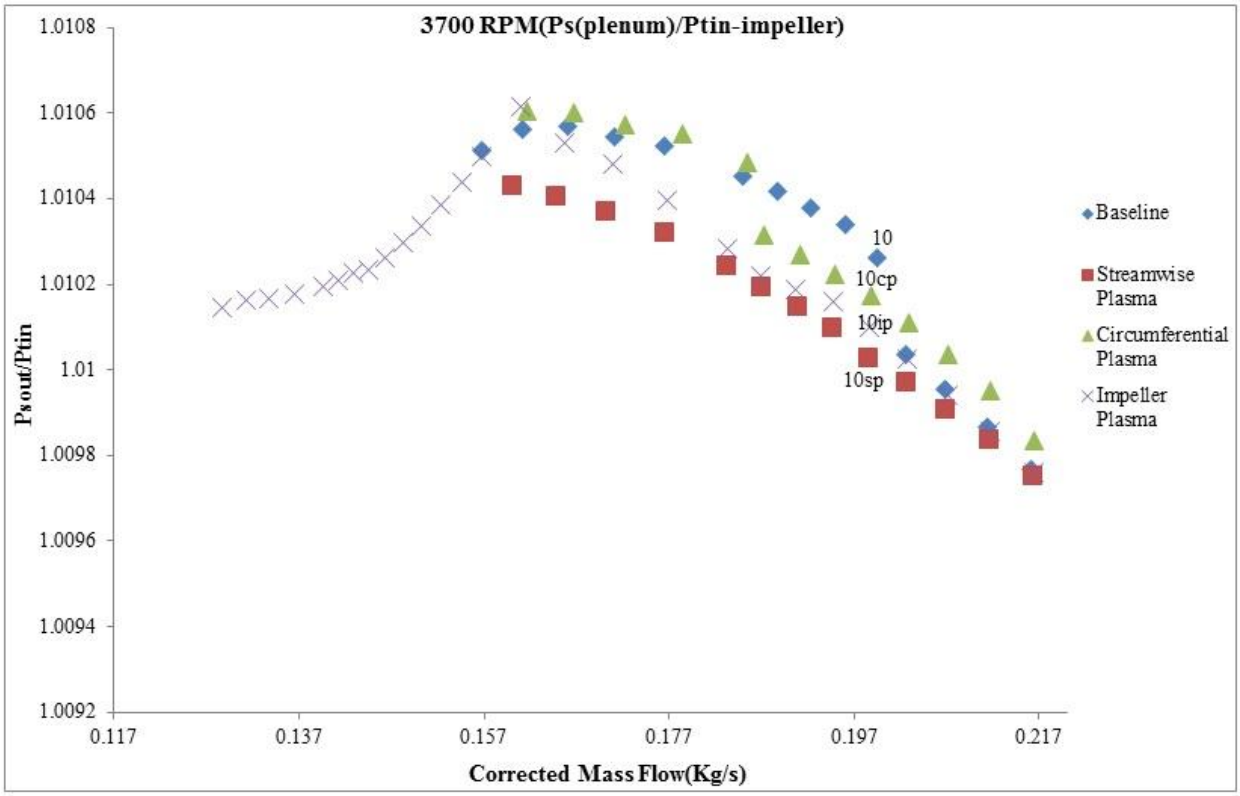

Figure G.3: Speedline of centrifugal compressor for different plasma locations and without plasma case

As noticed, none of the methods can increase pressure coefficient, because they increase recirculation in diffuser, however impeller plasma is the only location that can increase the range of operation and delay stall. The same location for plasma is used for simulations and tests at 3470 and 4400 RPM in this project.

APPENDIX H- Mesh study

A mesh study is performed to survey the effect of mesh size on the results and to evaluate the quality of the mesh used.

H.1 Entire compressor simulations

For doing a mesh study for the entire compressor, a point of operation should be chosen, since the most sensitive operational points are the points near stall, point 6 from figure 4.1 (the last stable operating point) is chosen and the area averaged static pressure measured at the outlet of the entire compressor (at the outlet of End Duct) is applied as the outlet boundary condition for different meshes. The criterion for judgment about the quality of the mesh is the corrected mass flow through the compressor. Table H.1 summarizes the characteristics of three different meshes applied for simulations at 4400 RPM.

Table H.1: Characteristics of different meshes applied for the mesh study of entire compressor

	Mesh #1	**Mesh #2**	**Mesh #3**
Number of nodes	521400	1091440	1957878
Number of elements	472840	1011536	1840984

Note that each time the number of nodes and elements are almost doubled. For doing so the number of elements and nodes in each domain are proportionally increased.

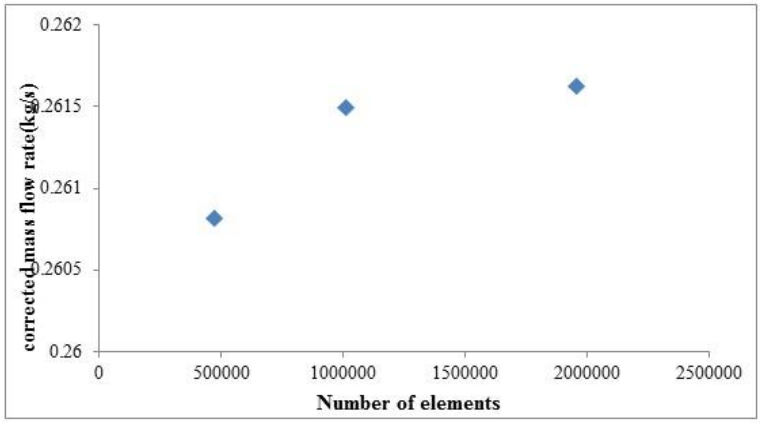

Figure H.1: Variation of corrected mass flow rate as a function of number of elements for the entire compressor

The density of Mesh#2 which is applied in this project for the entire compressor seems enough, since increasing number of mesh elements after that requires a much longer computational time and more powerful computational resources, however does not give a result with big difference, so it is not worth to make the mesh finer.

H.2 Centrifugal compressor

A similar study is also done for centrifugal compressor. Table H.2 shows the characteristics of the meshes applied and figure H.2 assesses the criterion for convergence based on the corrected mass flow rate for point 9 in figure J.2.

Table H.2: Characteristics of different meshes applied for the mesh study of centrifugal compressor

	Mesh #1	**Mesh #2**	**Mesh #3**
Number of nodes	240462	408329	1006030
Number of elements	213572	369306	938400

The results are shown in figure H.2; again Mesh#2 for centrifugal compressor which is used for simulations of centrifugal compressor in this project seems to have enough mesh density.

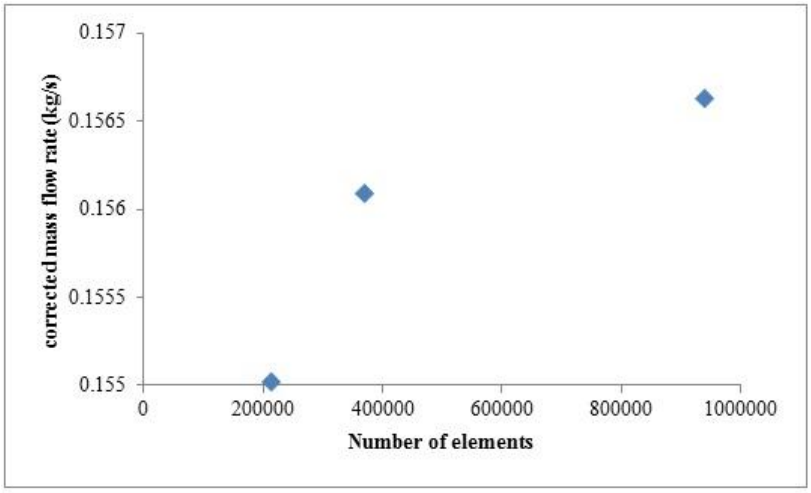

Figure H.2: Variation of corrected mass flow rate as a function of number of elements for the centrifugal compressor

APPENDIX I- Details of calculating errors for simulations and experiments

I.1 Errors in simulations

When simulating the points near stall with throttle setting, it is seen that mass flow, and pressures start to oscillate periodically versus time, in order to save time and judge about the convergence a Fast Fourier Transform analysis (FFT) is performed on these types of results. These oscillations consist of several different frequencies. (FFT) helps to find the lowest frequency which is translated as the highest time period of the oscillations ($T = \frac{1}{f}$), then the simulations are set to run for an integer number of this time period, and all data (mass flow rate, pressures, etc.) are time-averaged over this period of simulation to obtain the converged solution from the simulation. The amplitude of lowest frequency oscillation may reduce as the time passes, but the time-average which is of our interest remains constant, so after running the simulations for just several time periods (Known number of time-steps), it is possible to stop the simulations and get the averaged data. In the steady-state part of the speedline there is no oscillation, for point 6 in figure 4.1 despite that is the last stable operating point no oscillation is recorded. But for points 10p, and 11p, such oscillations exist and the errors are considered. So these points are shown with error-bars, but uncertainties in their mass flow rates are so small such that are even smaller than the symbol size. Such an analysis for the mass flow is shown in figure I.1, this method will also be used for centrifugal compressor results.

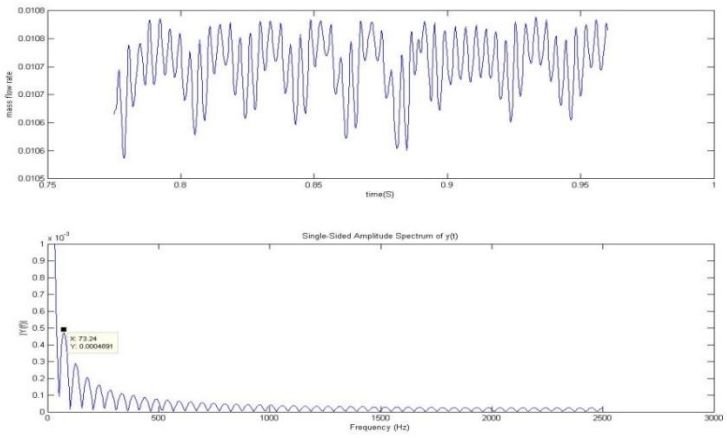

Figure I.1: FFT analysis for obtaining lowest frequency of oscillations

I.2 Errors in experiments

All the instrumentations measure data with a specified frequency that they are designed for, but since the LabView is programmed in a way that shows data every second, so all the necessary variables are recorded over a fixed period of time (10 seconds or 10 data) for each operating point or each valve position, the amplitude of the fluctuations are calculated based on the minimum and the maximum values measured during this fixed period. As mentioned in section 3.4 for insuring repeatability of data three tests are carried out in succession for two-stage configuration, and the results without plasma are shown in figure I.2, and the ones with plasma are illustrated in figure I.3, also two tests were performed for centrifugal compressor alone, results without plasma and with plasma are plotted in figures I.4 and I.5 respectively.

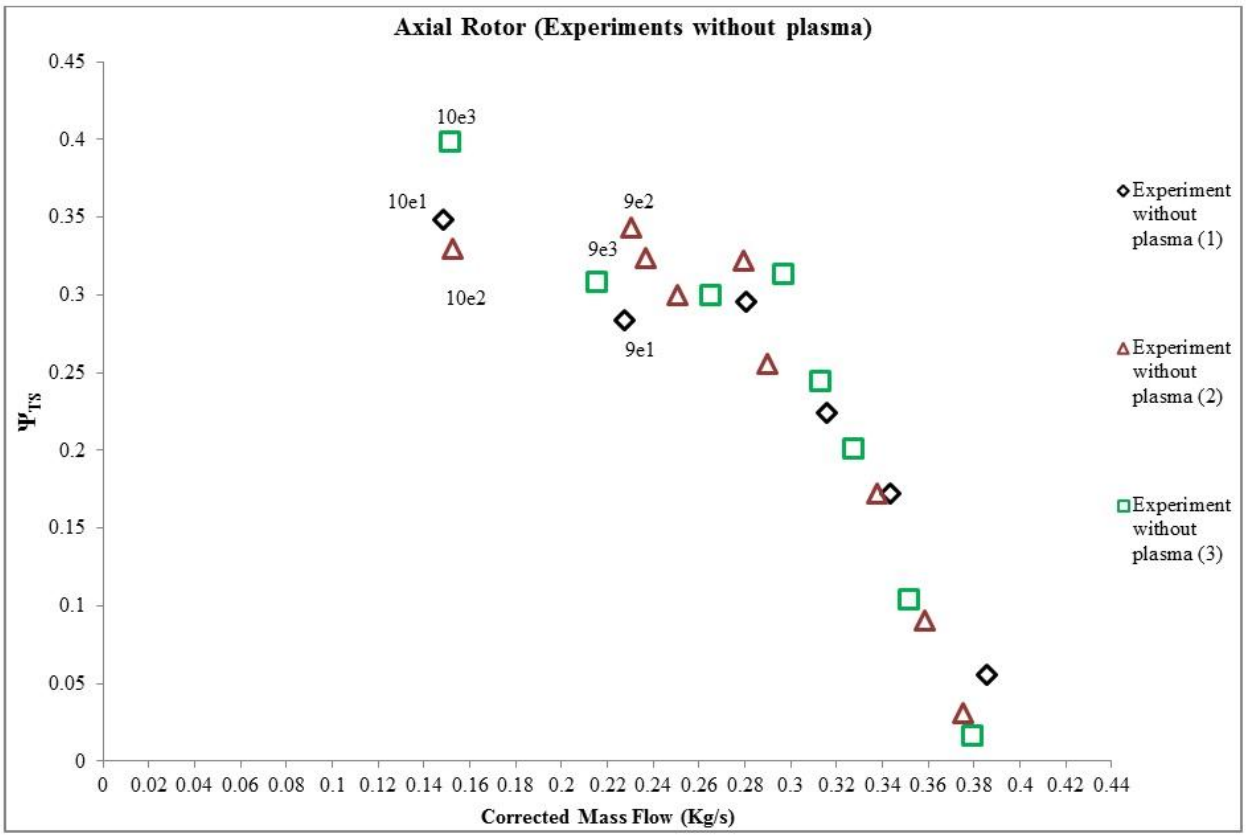

Figure I.2: Speedline of axial rotor without plasma in three different tests

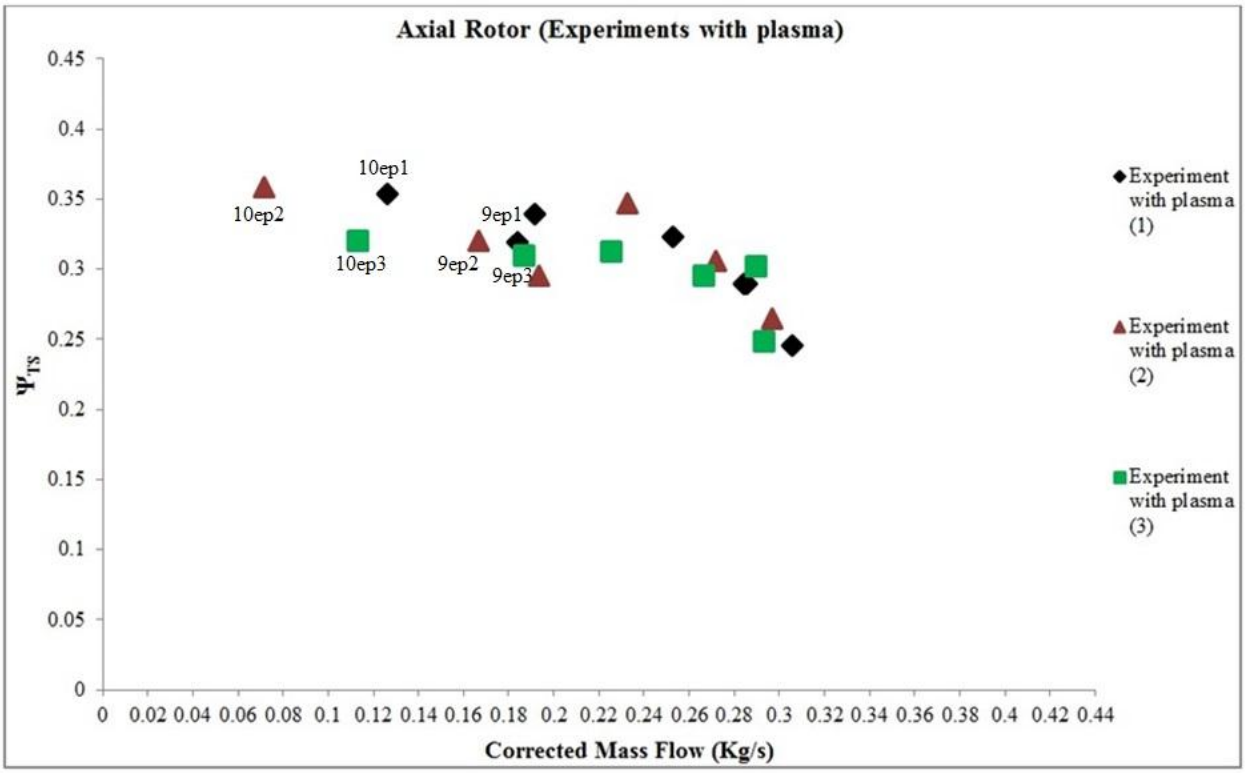

Figure I.3: Speedline of axial rotor with plasma in three different tests

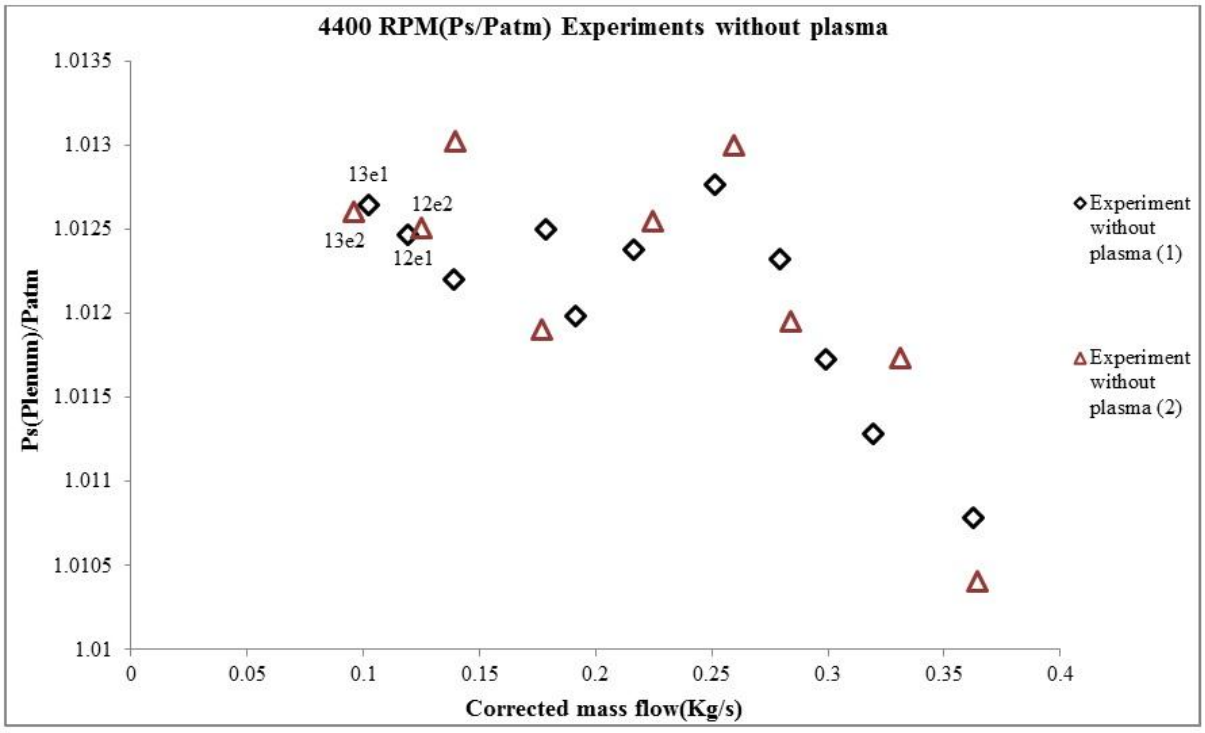

Figure I.4: Speedline of centrifugal compressor alone without plasma in two different tests

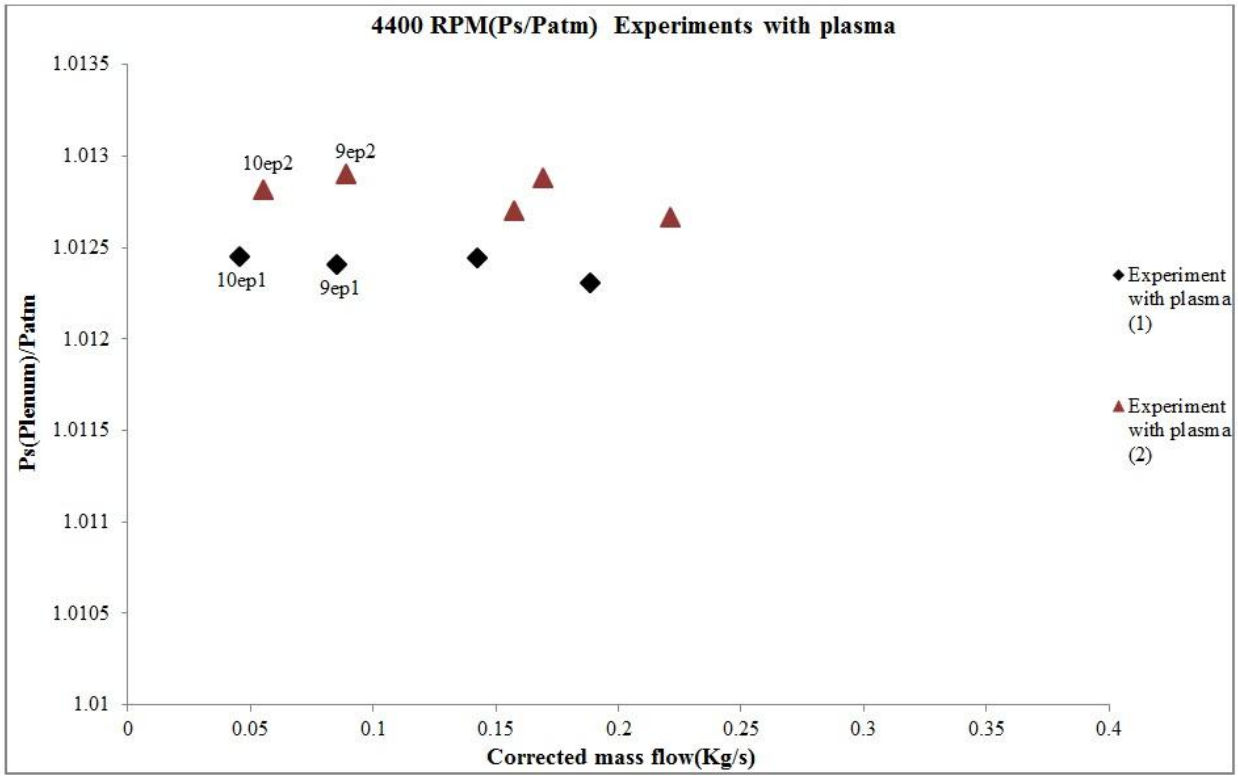

Figure I.5: Speedline of centrifugal compressor alone with plasma in two different tests

APPENDIX J- Centrifugal compressor results at 3470 RPM

J.1 Centrifugal results at 3470 RPM

Figure J.1 shows the speedline of the compressor with and without applying the actuation for both experimental tests and numerical simulations.

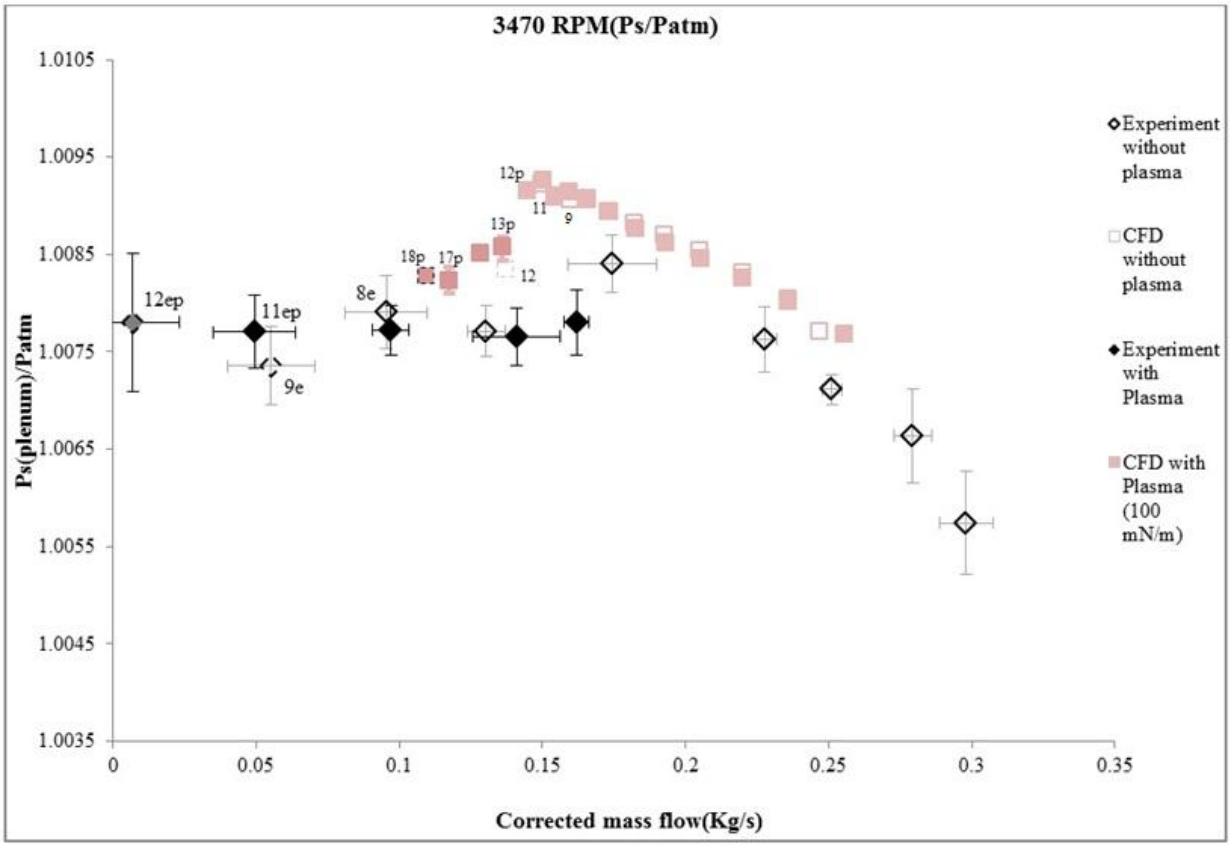

Figure J.1: Speedline of centrifugal compressor at 3470 RPM (CFD and experiment)

Again note the growth in error-bars size as moving up the speedline. For this speed the numerical results show an extension of 0.0327 kg/s in stall margin from point 11 to 17p (21.76 percent extension compared to the last stable point without plasma), and experimental results show that stall margin is extended by 0.046 kg/s (48.17 percent extension of last stable operating point). Both experimental and CFD results show a further extension in stall margin with 100mn/m actuation compared to 4400 RPM, the result which was anticipated in section 4.2,

however since the difference in speeds is not so great, the improvement in stall margin is not that big as well.

J.2 Effect of higher actuation strength

To predict the effect of actuation at higher actuation strength, in addition to 100mN/m, 300mN/m is also applied in CFD simulations at 3470 RPM. Figure J.2, shows the speedline of the compressor, without actuation, with 100mN/m actuation and with 300mN/m actuation.

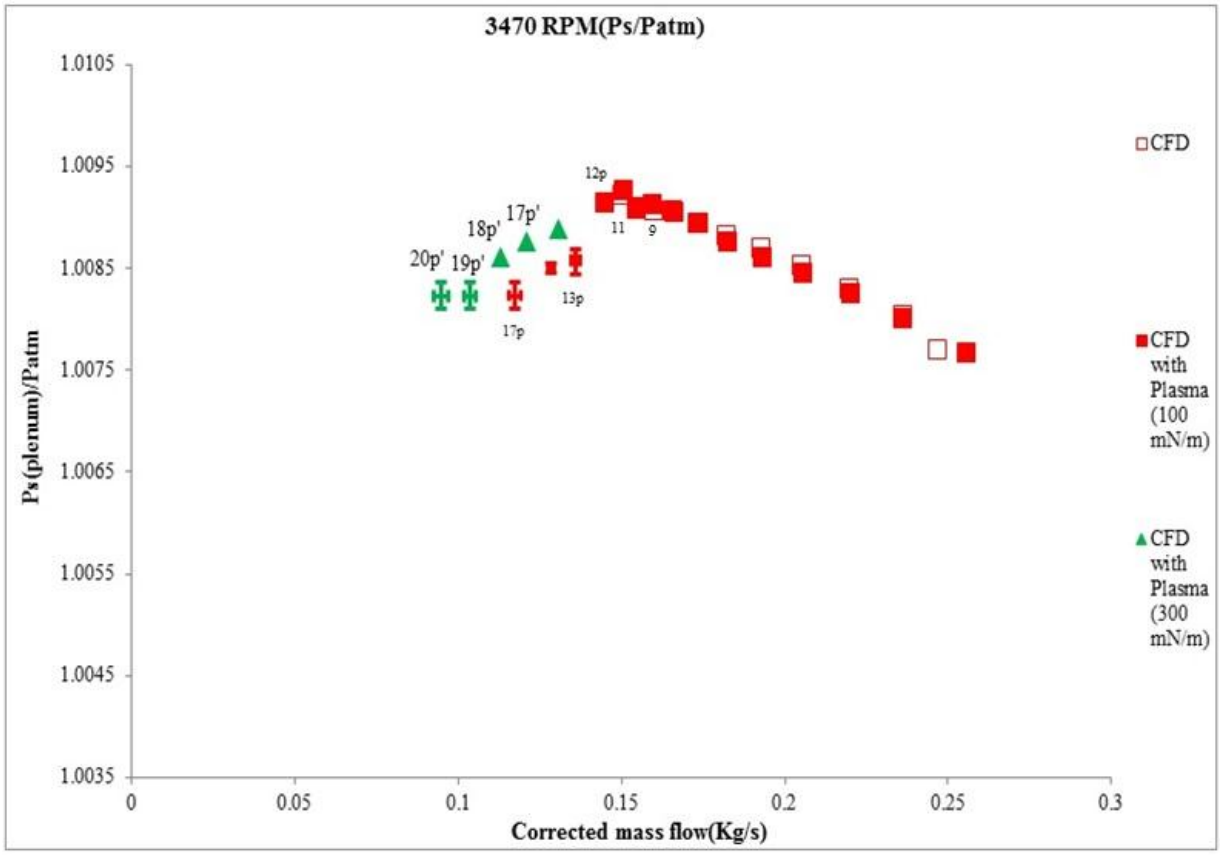

Figure J.2: Effect of higher strength actuation on stall margin improvement at 3470 RPM for centrifugal compressor

Higher actuation strength increases the momentum of incoming flow more and pushes the static entropy interface to a more downstream location and hence improves stall margin more than 100mN/m, a reduction of 0.0533 kg/s in mass flow rate of last stable point is recorded, compared to 0.0327 kg/s for 100mN/m. Note the change in location of interface for points 17p and 17p' for 100 and 300 mN/m actuations in figure J.3.

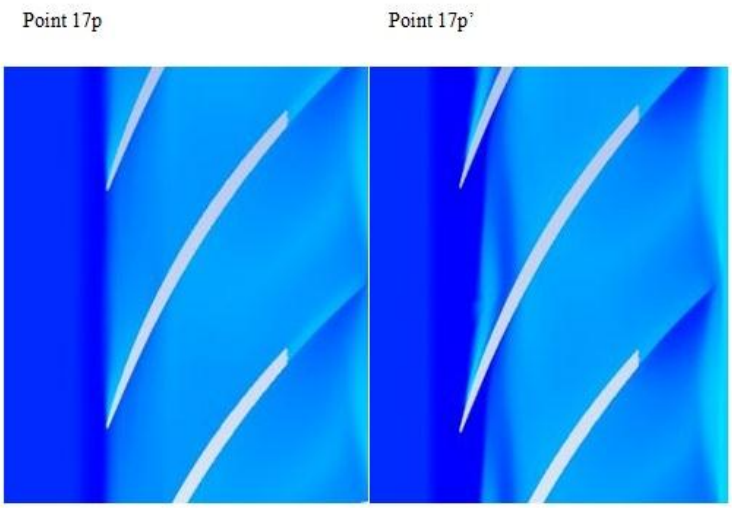

Figure J.3: Effect of higher actuation strength in replacing static entropy interface at 3470 RPM